.

Biophysical Modelling of Skeletal Muscle

by John B. Davidson

Supervised by

Professor Andrew J. Pullan

Dr Oliver Röhrle

A thesis submitted in partial fulfilment of the requirements
for the degree of Doctor of Philosophy
at the University of Auckland

Auckland Bioengineering Institute
The University of Auckland
New Zealand

April 2009

Abstract

This thesis presents a new framework and methodology for modelling the structure and function of skeletal muscles. It incorporates an anatomical description of the macroscopic structure of the muscle, an extensive representation of the physiology of skeletal muscle tissue, and comprehensive depiction of the functional response of skeletal muscle to both physiological and external inputs. The components of structure, physiology, and function are combined together to give the most detailed skeletal muscle model currently available. The general skeletal muscle modelling framework is demonstrated using the specific example of the human Tibialis Anterior.

The physiology of skeletal muscle is represented using the Shorten *et.al.* cellular model [105] and the Bidomain equations [55]. The structure of the human Tibialis Anterior muscle is represented using triquadratic-Lagrange Finite Elements, and includes information on the internal muscle fibre directions. Individual muscle fibres are explicitly represented within the muscle and are grouped into functional units (the Motor Units) in a physiologically accurate manner. Physiological activation, or activation as a result of an applied stimulus, can be represented.

Physiological data obtained from the combination of the fibre activation and the Bidomain simulation of muscle physiology are then linked, using a novel muscle constitutive law, to produce whole muscle deformation. The framework is a true multi-scale modelling framework, linking one of the most detailed skeletal muscle physiological models available to the deformation of the muscle as a whole. As a result of this detail, muscle force output profiles that replicate physiologically, and numerically obtained data, can be generated.

The modelling framework has been developed to maximise versatility. It provides for the first time a multi-scale framework where such a large number of model input parameters are able to be modified to demonstrate the effect of varying muscle properties. The versatility of this modelling framework is demonstrated by building stimulation protocols, using the constraint of inverse muscle recruitment, which represent normal, physiological, muscle recruitment.

It is hoped that, with further advances in knowledge concerning the mechanical behaviour of skeletal muscle, this modelling framework will be able to provide insight into the development of Functional Electrical Simulation

protocols, as well as provide a tool for researchers interested in the interaction of structure and function within skeletal muscle.

Acknowledgements

This thesis is a result of the help and support of a large number of people. I would like to spend the following few paragraphs trying to do justice to them.

Firstly I would like to acknowledge my funding source. This work was funded through the Foundation for Research in Science and Technology under contract UOAX0406. Without these generous funds, this work would not have been possible. Funding for various conferences was also obtained from: The University of Auckland Graduate Research Fund; the Postgraduate Research Support Service, University of Auckland; and the Bioengineering Institute, University of Auckland.

To my supervisors Andrew and Oliver, thank you very much for your help and support. I cannot count the number of times that I've come to you with questions and problems, and you have been nothing but generous with your time and energy. I've really enjoyed the PhD journey, with its ups and downs, and I believe that this fact is primarily a reflection on your supervision. On the lighter side, I've also benefited from Oliver's knowledge on fluid dynamics and skiing, while Andrew has instilled in me the importance of leading a world class research group before renovating a house.

There have also been a large number of members of the Bioengineering Institute to which I owe a huge debt of gratitude. I would like to thank the following people specifically for there help on the technical side of things. To Mark Trew and Leo Cheng, thanks very much for finding time to put up with all my questions. To David Nickerson, thanks for all the help with CellML. Kumar, thank you for your help with CMISS. To Andrew Cantell, Tiong Lim, and more recently Peter Schmiedeskamp, thanks very much for fixing things when I broke them. I would also like to thanks everyone above for being easy to deal with and making asking for help easy.

There are a large number of people that I have become good friends with over the last four to six years. From the coffee group, to Friday drinks, student and staff alike who have made the social side of working at the institute a real pleasure. I'm able to name but a few, so to Rita, Zoar, and Richard, its been great fun sharing an office with you over the past years. The conversations, jokes, and general stupidity have kept me going. Kieran, Paul, David and

Casey plus all the regulars at Friday drinks, the weekly lunch outing, institute sporting events, coffee breaks, CoHo's, and other miscellaneous events, it would not have been the same without you.

To my family, especially my parents, thank you for your love and support. Jacqui, thanks for putting up with me, for motivating me, for always making me feel better. This work is just another moment in time where you have been there for me.

Contents

List of Figures

List of Tables

Glossary of Symbols & Abbreviations

Symbols

Symbol	Description
A_1	Concentration of Cross-bridges Pre-powerstroke
A_2	Concentration of Cross-bridges Post-powerstroke
MU	The Number of Motor Units
MU_1	Number of Fibres in Smallest Motor Unit
MU_{Ftot}	Number of Fibres in the Calculated MU Distribution
MU_n	Number of Fibres in Largest Motor Unit
MU_{ratio}	Input Value, Ideal MU_n/MU_1
ρ_{MUT}	Motor Unit Territory Density
T^{MN}	$2^{nd} Piola - Kirchhoff$ Stress Tensor
T_{tot}	Total Number of Fibres Generated in the Muscle Geometry
V_m	Transmembrane Potential

Abbreviations

Abbreviation	Description
ACSA	Anatomical Cross-sectional Area
ADP	Adenosine Diphosphate
ATP	Adenosine Triphosphate
Ca	Calcium
CMISS	Continuum Mechanics, Image analysis, Signal processing and System identification
CT	Computed Tomography
EDL	Extensor Digitorum Longus
EMG	Electromyogram
FEM	Finite Element Method
FES	Functional Electrical Stimulation
ISI	Inter-spike Interval
K	Potassium
LSODA	Livermore Solver for Ordinary Differential Equations
MFR	Minimum Firing Rate
MURF	Motor Unit Representative Fibre
MUT	Motor Unit Territory
Na	Sodium
PCSA	Physiological Cross-sectional Area
PFR	Peak Firing Rate
P_i	Inorganic Phosphate
RMS	Root Mean Square
RTE	Recruitment Threshold of Excitation
RyR	Ryanodine Receptor
WTFN	The Value of the Weighting Function

Chapter 1

Motivation

The structure and function of skeletal muscle has been the subject of investigation for many years. Over the last five decades, developments in the areas of molecular biology, physiology, and the ever increasing level of technology, which is used to probe all facets of science, have led to a massive body of knowledge on the structure and function of muscle. However, there are still areas where our understanding is relatively limited.

As needs and technologies change, emphasis shifts to areas where the greatest gain in knowledge can be made. The progress in the field that led to the advent of technologies such as Functional Electrical Stimulation, Electromyograms, and tendon relocation surgery; our improved understanding of how genetic-based diseases occur and progress; and our ubiquitous quest for knowledge, has induced a massive drive to increase our understanding of how muscle tissue works. For example, Functional Electrical Stimulation, a rehabilitation technique, requires improvements in the areas of electrode localisation, stimulus protocol design, and activation trains to help minimise fatigue and improve the technique's efficacy. In order to enhance Electromyography (EMG) into a tool that can be used for diagnosis of ailments and improve its research capabilities, greater knowledge is required as to the Electromyograph's specific output, and how different patients, time courses and muscle geometries can effect the output. When performing tendon relocation surgery in order to improve a patient's quality of life, a detailed understanding on how the change in the location of muscle attachment areas will effect the three-dimensional interactions of the surrounding musculoskeletal system is desirable. In addi-

tion, the possible effects on performance that a muscle of different composition and structure will haven in the modified system would also be of benefit. Genetic diseases, such as muscular dystrophies and cerebral palsy, that affect the structure and composition of muscle over time could be diagnosed earlier and possibly treated in a more effective manner with a more inclusive concept on the electrical and mechanical functioning of muscle in health and disease.

The work presented in this thesis has been motivated by the fact that modelling of a system is integral to the process of understanding the underlying function of a system and thus facilitating more targeted investigations into areas of interest. A multi-scale modelling framework that is able to replicate much of the current knowledge on skeletal muscle structure and function would not only be of great use in further understanding the problems outlined above, but would also be an invaluable tool in helping researchers and experimentalists gain insight into future problems and help guide them to likely areas of interest, or methods of investigation. This alone would save time and effort in both experimental time and ethics requirements. Further, advances in the areas of anatomy, physiology, molecular biology, and biomechanics have tended to create large pools of related, but disjoint, information. A number of studies on the function of skeletal muscle have attempted to pull information together from different areas, e.g. the work of Fernandez *et.al.* [33], however the work presented in this thesis is one of the most complete multi-scale modelling frameworks to date, including sub-cellular muscle behaviour, structural organisation, functional organisation, and whole muscle response.

With these goals in mind, the work presented creates a framework for musculoskeletal modelling that integrates the sub-cellular function of muscle tissue, as defined by the Shorten *et.al.* model [105] and is also able to predict the large scale muscle response as a result of these sub-cellular actions using the governing equations of finite elasticity. Further, the presented framework is capable of replicating the gross control mechanism of normal skeletal muscle to achieve a realistic large scale response by using elements of the Fuglevand *et.al.* [36] and Enoka *et.al.* [30] models, which define muscle composition and whole muscle response to activation. In addition, a large amount of flexibility is included so that changes in sub-cellular physiology, internal muscle structure, gross structural changes, functional grouping and control mechanisms can be

investigated. To this end, the work detailed in this thesis is set out as follows;

- The *Introduction and Background* (Chapter 2) gives a short background on skeletal muscle structure and function. The structure and function of skeletal muscle from the sub-cellular level of membrane channels and contractile proteins up to the full muscle anatomy and functional organisation are detailed. A discussion on previous skeletal muscle modelling work is also included.

- The theory used to develop and solve the mathematical models of the multi-scale framework is covered in Chapter 3, *The Formulation of the Modelling Framework*. The Bidomain formulation, finite elasticity, and a brief description of the finite element method are included, as well as an introduction to the software package, CMISS, which has been modified and extended to carry out this work.

- The *Creation of a Whole Muscle Model* chapter (Chapter 4) demonstrates the method used to develop the three-dimensional muscle structure, including the physiological modelling of a single muscle fibre, internal fibre distribution, using the Tibialis Anterior muscle as an example. Furthermore, a novel method for spatially grouping the fibres into functional units is proposed.

- Results of the full muscle simulations are then presented in the *Results of Whole Muscle Activation Simulations* chapter (Chapter 5). A number of different muscle activation simulations are presented, along with the techniques used to replicate whole muscle activity. Normal physiological recruitment is considered as well as the effect of inverse recruitment, which occurs as a result of Functional Electrical Stimulation (FES). FES is used as an example of how the presented framework can be adapted to different skeletal muscle properties. As such the model provides an insight into the resulting differences between inverse recruitment and normal physiological function.

- This work concludes with a full discussion on the framework and the results along with a summary of conclusions that can be drawn from this work (Chapter 6).

Chapter 2

Introduction and Background

This chapter is intended to give the reader the necessary background on the structure, function, and classification of skeletal muscle, as well as a brief background into other methods of modelling such tissue. It introduces the information and concepts that will be called upon in later chapters to develop the proposed musculoskeletal modelling framework. Firstly, the function of skeletal muscle, and its anatomical make up will be defined, followed by the transmission of generated force through the muscle fibre network. Then the sub-cellular organisation of muscle fibres, and the metabolic properties of skeletal muscle will be described. The differences between different types of skeletal muscle fibres as well as the internal structure of skeletal muscles are then discussed before the functional grouping and activation of whole muscles are outlined. The control system and the transmission of activation information from the central nervous system to the individual muscle fibres will be described, followed by a brief introduction into the areas of Functional Electrical Stimulation and Electromyography. Finally, a brief background on previous skeletal muscle modelling work and its implementation is presented.

2.1 Skeletal muscle function in the body

Muscle is one of the most abundant tissues in the human body and is subdivided into skeletal, cardiac, and smooth muscle. The primary role of all muscle is the conversion of chemical energy into physical work and in this capacity it facilitates many of the body processes necessary for homeostasis. Our heart,

the pump that keeps our entire bodies supplied with oxygen and nutrients, is composed of cardiac muscle, a form of striated (banded) muscle that is ideally suited to its role of pumping blood, approximately once a second, for our entire lives. Smooth muscle, so named because, under the microscope, it does not display the banding pattern of striated muscle and thus appears smooth, controls the function of a great many important organ systems. It controls the flow of blood around the body by altering the diameter of blood vessels, it is responsible for the movement of food through our digestive tract plus many other important roles in the daily life of our bodies. Skeletal muscle, by far the most common type of muscle composes approximately 40-50% of our body weight [111]. Unlike cardiac and smooth muscle, it is under voluntary control, and its primary purpose is to allow us to move and explore the world around us. In addition to voluntary control, most skeletal muscles are also involuntarily controlled to some extent, allowing, for example, continual maintenance of posture and ventilation of the lungs. Skeletal muscles also play a role in maintaining fluid flow through the body by helping to push blood through veins from distal regions. Also, in cases of thermal stress, skeletal muscle can be used to heat the body through the action of shivering.

Skeletal muscle is a finely tuned tissue and, although its structure must be maintained precisely for efficient function, it is a very plastic tissue. Given different demands it can modify its function to allow great endurance or explosive power. The diverse attributes of skeletal muscle are made possible by its complex structure and control systems.

2.2 Skeletal Muscle Anatomy

A schematic of the structure of skeletal muscle can be seen in Figure 2.1. The basic unit of skeletal muscle is the muscle fibre, which is synonymous with a muscle cell. These cells can be many centimetres long and contain many peripherally located nuclei surrounding the force producing protein structures. In humans, muscle fibres are approximately $80-100\mu m$ in diameter [70, 78, 106]. Each of these muscle fibres is surrounded by a layer of connective tissue called the endomysium, of which the primary load bearing component is collagen, anchoring the fibre to its neighbours and providing a path along which force

can travel. A single muscle fascicle contains tens to thousands of muscle fibres, depending on the specific muscle. Each fascicle is bound in its own connective tissue layer call the perimysium. The perimysium is also made up of collagen and provides a further path for force to be transferred. The physical connections between fascicles are less tight than between fibres and thus fascicles also allow the muscle to deform and shear. A whole muscle is composed of a number of fascicles and is wrapped in its entirety in a final connective tissue layer termed the epimysium. Skeletal muscles are connected to the skeleton via tendons, which are primarily made of collagen. There is a gradual interface between the muscle tissue and the tendon allowing for force transduction to the skeleton. In many human muscles, the muscle fibres do not span the full distance from tendon to tendon, instead they are connected serially to subsequent fibres. This type of muscle structure is termed intrafascicular termination. This type of muscle structure raises many questions as to the control systems and force transduction paths of skeletal muscle, questions that are currently unanswered [111].

2.3 Skeletal Muscle Morphology

Although the general function of all skeletal muscle is the same, individual muscles are often required to have vastly different functional properties. As a result different muscles have different fibre and tendon architectures which allow them to best perform their specific role in the body. For example, muscles located at the extremities of the body, such as the soleus (a calf muscle) tend to have compact, proximally located, muscle bodies with long distal tendons. This allows for elastic energy to be stored in the long tendon (useful for energy conservation during walking and, taken to an extreme, in the bounding of a kangaroo) [88]. This configuration also reduces the inertia around the joint (in this case the knee joint) by locating most of the mass of the muscle-tendon complex centrally. Muscles can also be divided into different anatomical and functional compartments. For example, the semitendinosus muscle of the hamstrings is divided into a proximal and distal compartment by a collagen rich dividing line called a tendonous inscription. The two compartments function together as one muscle and the inscription reduces the required length of muscle

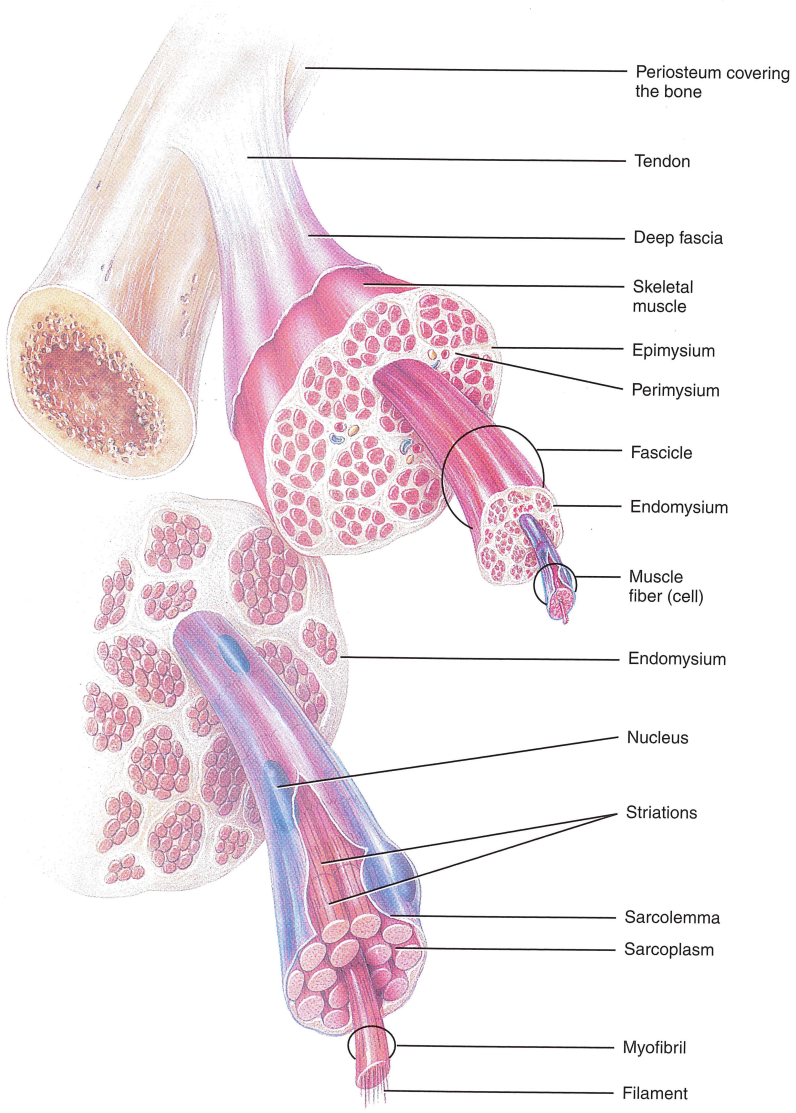

Fig. 2.1: A depiction of the internal structure of a skeletal muscle. The muscle is shown attached to the bone via the tendon and surrounded by the epimysium and the deep fascia (a layer of connective tissue). A fascicle, surrounded by perimysium, is seen extending from the skeletal muscle and, extending from the fascicle, a muscle fibre is shown. An expanded view of the fascicle is then depicted with the structure of the muscle fibre shown more clearly. The endomysium, cell nucleii, the striations, the cell membrane (sarcolemma), and the myofibril containing the filaments are shown (Figure reproduced from Tortora and Grabowski [111]).

fibres. Muscles can also be organised into different functional compartments, usually as a result of innervation from more than one nerve. For example the rabbit masseter is innervated by more than one nerve [80]. As a consequence of differential activation of the resulting muscle compartments, different force vectors are generated to fulfil different functional requirements.

Pennation Angle

The force, which an individual muscle is able to produce, is dependant on the muscle's cross-section. The cross-section of a muscle perpendicular to the longitudinal axis of the muscle is referred to as the anatomical cross-sectional area (ACSA) [82]. The force produced by a muscle is also dependant on the angle of the fibres with respect to the longitudinal axis of the muscle, the so-called pennation angle of the muscle. Muscles, in which the fibre direction is not aligned with this axis are termed pennate muscles, of which there are a number of sub classifications. The simplist form of muscle occurs when the muscle fibres lie parallel with the axis of force. These muscles are termed fusiform muscles (i.e. a pennation angle of 0^o as depicted in Figure 2.2). Unipennate muscles have fibres with a uniform orientation to the axis of force. Bipennate muscles have two populations of fibres with different angles with respect to the axis of force and multipennate muscles have a number of populations of fibres misaligned with the axis of force [111] (see Figure 2.3).

A better measure of the force output of a particular muscle is therefore the physiological cross-sectional area (PCSA), the area of the muscle at right angles to the longitudinal axis of the muscle fibres [82]. In muscles where large forces are required muscle fibres can be oriented obliquely to the axis of force, thus giving a greater PCSA without changing the ACSA. That is, the area of fibres able to contract and generate force is greater than the cross-section of the muscle as a result of an oblique fibre angle. However, muscle speed is sacrificed as the primary direction of shortening is also oblique with respect to the longitudinal axis.

Fig. 2.2: Schematic of a fusiform muscle (e.g. the difastric muscle of the throat [111]). Note that fibres are aligned with longitudinal axes of the muscle (reproduced from Tortora and Grabowski [111]).

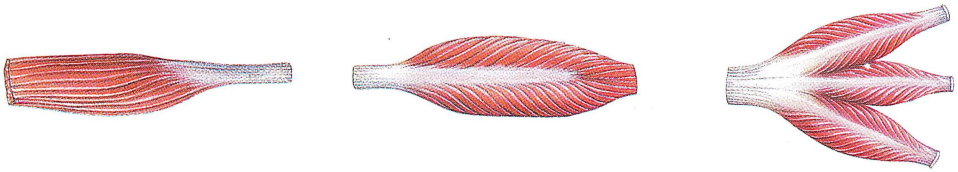

(a) (b) (c)

Fig. 2.3: The structure of a unipennate (a), bipennate (b), and multipennate (c) muscle. The unipennate muscle only has one fibre angle with respect to the longitudinal axis on the muscle (e.g. extensor digitorum longus [111]), whereas the bipennate muscle has two (e.g. rectus femorus [111]). There are six different fibre directions in the multipennate muscle shown (e.g. deltoid [111]) (reproduced from Tortora and Grabowski [111]).

2.4 Force Transmission

Skeletal muscles have historically been modelled as a collection of parallel muscle fibres, extending from tendon to tendon [80]. As a result it has been assumed that the tension generated by the contractile apparatus is directly transferred to the tendon at the myotendinous junction. A number of experiments and observations have shown that the simplistic view of muscle fibres transferring their generated force directly to the myotendinous junction is over simplified. Street [110] designed an experiment in which the force generated by a single fibre was measured by fixing one end a section of muscle, excising a single muscle fibre from the muscle at the opposite end and attaching this to a force transducer. It was shown that when the fibres surrounding the single fibre were held instead of the fibre end itself, at the fixed end, $76 - 100\%$ of force was still recorded by the transducer. This result showed that force was not necessarily transferred through the muscle fibre, and up to 100% of the force generated by a muscle fibre could be transferred by the surrounding connective tissue.

Goldberg *et.al.* also found that cutting a pie shaped wedge out of the lateral rectus muscle of the cat, about 1/3 of the width of the muscle, had very little impact ($> 5\%$) on the force production of the muscle [39]. The mechanism proposed to account for these experimental observations is termed lateral force transmission. Lateral force transmission is the transmission of force generated by a muscle fibre to the surrounding muscle fibres and connective tissue. Proske *et.al.* [95] observed that when the tendon of the soleus muscle of the cat was split longitudinally into two halves, muscle force was approximately equally divided between the two halves, and this remained consistent independant of muscle force. They concluded that the force generated by the muscle fibres must be integrated in some way before being transferred to the tendon [95].

The transmission of muscle fibre force is achieved by specialised protein complexes called costamers that link the cellular contractile machinery to the extracellular matrix. These costamers are located all over the sarcolemma but preferentially over Z and M lines (see Section 2.5) and are found to co-localise with collagen and laminin in the extracellular matrix [81]. They are composed of a number of intracellular and transmembrane proteins such as

vinculin, dystrophin and intergrins, and deficiencies in these proteins can result in muscular dystrophies. The force is tranferred from the extracellular matrix to the tendon via the myotendinous interface.It is possible that up to 50% of force is transferred laterally through the muscle, however in-vivo experiments are difficult to perform [43].

There are still a number of unknowns concerning the force summation in skeletal muscle, for example, the reason that the force of two active motor units is not equal to the sum of each motor unit activated individually. Non-linear force summation is possibly a result of differences in the anatomy of the constituent muscle fibres [80]. The contractile state of surrounding fibres may also affect the force produced by muscle fibres [30].

2.5 Sub-Cellular Anatomy

The sub-cellular structures responsible for muscle force generation are sarcomeres, which are repeating subdivisions of specialised protein structures called muscle fibrils [111]. When skeletal muscle was first examined under a microscope it was noticed that there was a regular banding pattern or striations. Closer examination revealed that the regular pattern could be broken down further into the groupings in the list below. It is now known that these regions contain various protein structures, primarily actin and myosin (refer to Figure 2.4).

1. A-band: optically anisotropic or birefringent; i.e., the refractive index of the material depends on the angle of incident light relative to the material. It contains both thick and thin filaments (longitudinally overlapping).

2. I-band: contains thin filaments only (which have opposite polarity either side of the Z-line). (This area appears isotropic under the microscope).

3. Z-line: an electron-dense region in the middle of the I-band where actin filaments of different polarity in each half sarcomere attach. The inter-Z-line distance defines the (variable) sarcomere length.

4. H-zone: a region in the centre of the A-band which contains thick filaments only (and hence is not as dark as the rest of the A-band).

5. M-line: an electron-dense region in the centre of the H-band where myosin filaments of different polarity attach.

The primary functional constituents of the sarcomere are the thick and thin filaments. The thick filament is primarily composed of myosin. The thin filament is made up of actin, and the control proteins, troponin and tropomyosin. These filaments are arranged in an interdigitating pattern which allows specialised sections of the myosin protein to attach to the actin, forming structures known as crossbridges. These crossbridges are then able to deform, releasing the energy stored in them, thus moving the proteins relative to each other creating force and movement (refer Figure 2.16). A vast number of proteins are responsible for various tasks within the sarcomere such as maintaining the structure (e.g. titin and nebulin), controlling the interaction of actin and myosin (e.g. troponin and tropomyosin), and transferring the generated force to the surrounding tissue (e.g collagen, laminin, dystrophin and intergrins).

2.5.1 The Thick Filament

The thick filament (made up of myosin) is approximately $1.6\mu m$ long and is largely monomolecular. It contains approximately 300 myosin molecules arranged in a strict three-dimensional geometry. It forms spontaneously under physiological conditions. The myosin molecules form a linear fragment with a central bare patch and opposite 'molecular polarities' on either side. Each subsequent myosin molecule self-assembles with an angular displacement of 60^o and a linear displacement of $14.3nm$ leading to a unit repeat distance of $42.9nm$. Hence crossbridges project in 6 equally spaced pairs around the circumference of the thick filament. Individual myosin molecules are $470kDa$[1] and are $160nm$ long. Each molecule consists of two heads on a single tail consisting of a double stranded coil. Myosin can be cleaved (by trypsin or chymotrypsin) into two moieties: light meromyosin (LMM) and heavy meromyosin (HMM). The HMM unit can be further divided into the myosin heads (which are the

[1]The Dalton (Da) is a unit of molecular mass equal to 1/12 of a carbon-12 atom

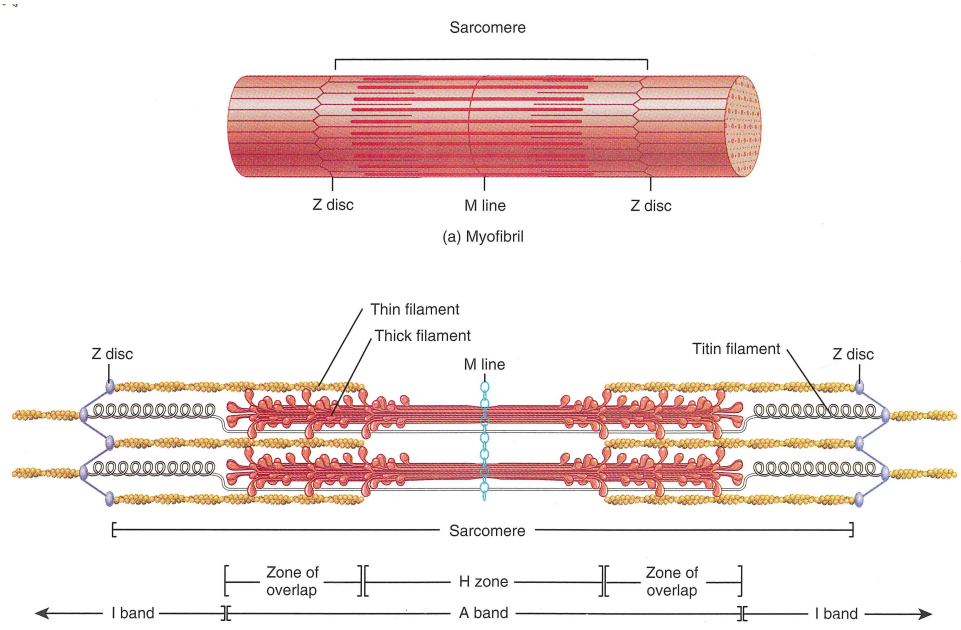

Fig. 2.4: A schematic drawing depicting a sarcomere as a whole is shown (top), and a close up view of it's constituent structures (bottom). The interdigitating thick and thin filaments (myosin and actin respectively) form the basis for each sarcomere. A sarcomere is linked to its neighbour at the Z-disk and is symmetric about the M-line, the centre of the thick filament (reproduced from Tortora and Grabowski [111]).

structures that form the crossbridges), Myosin Heavy Chain (MHC) and also four Myosin Light Chains (MLCs) (see Figure 2.5). The heavy chains are able to hydrolyse ATP, and the energy is used to change the physical structure of the myosin head from a low energy state to a high energy state (see Figure 2.16). The light chains help to regulate the activity of the myosin head. There are a number of different isoforms of myosin, each with slightly different ATPase activity, giving each slightly different functional properties.

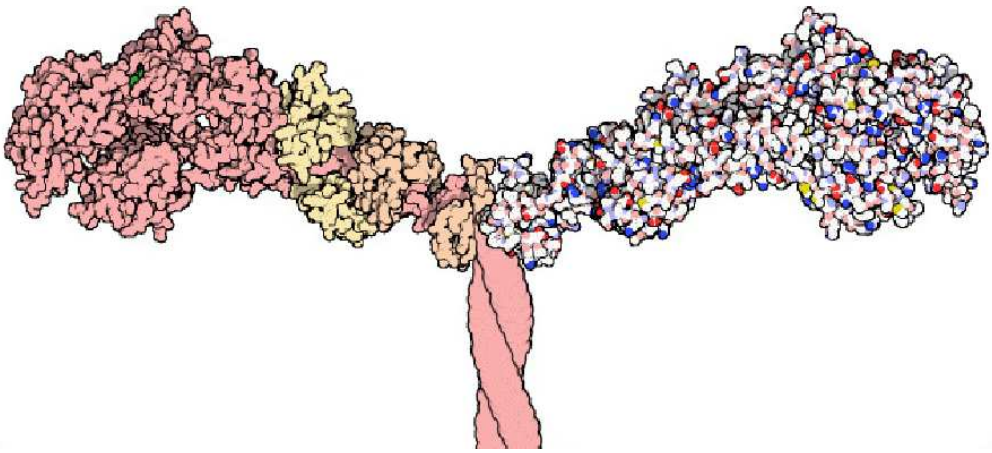

Fig. 2.5: The two heads of a myosin molecule. The atoms of the heavy chain (MHC) are coloured red on the left hand side and the light chains (MLC) are coloured orange and yellow (on the left).

2.5.2 The Thin Filament

The primary constituent of the thin filament is actin. Actin is composed of the globular G-actin molecule ($42kDa$). Under physiological conditions G-actin spontaneously polymerises, with an axial separation of $5.46nm$ into (filamentous) double stranded F-actin with a pitch of $73nm$ (see Figure 2.6). Each thin filament contains one F-actin strand of some 350 G-actin monomers, this inserts into the Z-line where it changes polarity. Its interaction with myosin is controlled by troponin and tropomyosin.

Tropomyosin is a rigid, insoluble molecule that polymerises end-to-end, with a slight overlap, such that each thin filament contains 50 molecules. Each molecule contains 7 similar regions along its length each of which inhibits the binding of myosin to a single G-actin molecule. Tropomyosin lies asymmetri-

cally in the groove formed by the double actin strands (i.e. closer to one strand than the other). It sterically inhibits the actin-activated ATPase activity of myosin as seen in Figure 2.6.

Troponin is a globular protein consisting of 3 polypeptides. Troponin-T binds to tropomyosin in a 1:1 stoichiometry so that each thin filament contains 50 tropomyosin molecules, troponin-C binds (up to 4) Ca^{2+} in a co-operative manner, and troponin-I together with tropomyosin, inhibits the activation of actin activated myosin ATPase activity by binding to actin (refer to Figure 2.6). These interactions are very important to the control of skeletal muscle, and play a large role in the cell modelling work outlined in Chapter 3.

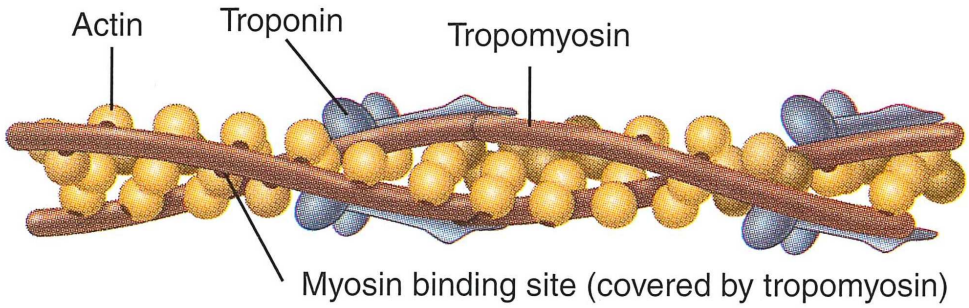

Fig. 2.6: The interaction of the double stranded actin molecule (yellow/orange), tropomyosin (brown) and troponin (grey/blue). The tropomyosin sterically inhibits myosin from interacting with the binding sites on the actin molecules. In the presence of calcium, troponin removes the inhibition by causing a conformational change in the location of the tropomyosin.

2.5.3 Structural Proteins

There are more than a dozen structural proteins that contribute to the precise architecture of the myofibril. Titin (connectin) is one of the biggest proteins found in the body at approximately 3MDa. It extends from Z-disk to M-line. It consists of a compliant section in the I-band and a stiff section in the A-band. It is connected to myosin via C-protein which binds to the MHC tail. It is connected to the M-line via M-protein. It acts as a molecular ruler, dictating the length of the thick filament.

Nebulin is another huge protein approximately 700-900kDa. It runs from the Z-disk to the end of the thin filament. For each thin filament there are

two nebulin molecules which are probably localised in the groves of the actin molecules. Nebulin acts as a molecular ruler for actin.

2.5.4 The T-tubular Network

The outer membrane of skeletal muscle, or sarcolemma, is pocketed with orderly invaginations of plasma membrane forming the transverse tubular (or T-tubular) network. This is a specialised network which allows Action Potentials to quickly travel into the centre of the fibre to where the muscle fibrils are located. The T-tubules can be seen running through the cell in Figure 2.7. Located in close proximity to the T-tubules is the Sarcoplasmic Reticulum which is the intracellular calcium store (see Figure 2.7). The specialised area of Sarcoplasmic Reticulum that comes into close proximity to the T-tubules is the terminal cisternae. This structure contains many calcium specific channels called Ryanodine Receptors which are in close association with T-tubular calcium channels (Dihydropyridine Receptors) and these are the primary channels that allow calcium signalling in skeletal muscle.

2.6 Metabolism

The most basic energy currency in the body is adenosine triphosphate (ATP). It is this molecule that is primarily used by muscle, and all electrically active tissue, to maintain the required ionic environment, and it is also the molecule that facilitates the contraction of all types of muscle (for example, see Figure 2.16). ATP is produced via the oxidation of high energy glucose, which can be ingested or produced from stored glycogen or triglycerides. The energy gained from this reaction is used to add inorganic phosphate (P_i) to ADP (adenosine diphosphate). ATP is able to be hydrolysed by enzymes called ATPases, back into ADP and P_i. The energy release is then able to be used to facilitate energetic needs.

Depending on the level of oxygen available to the cell, production of ATP can be achieved in aerobic (in the presence of oxygen) or anaerobic (in the absence of oxygen) conditions. The process of glycolysis is able to produce 2 ATP molecules at the expense of 1 glucose molecule (Subfigure 2.8(a)), with

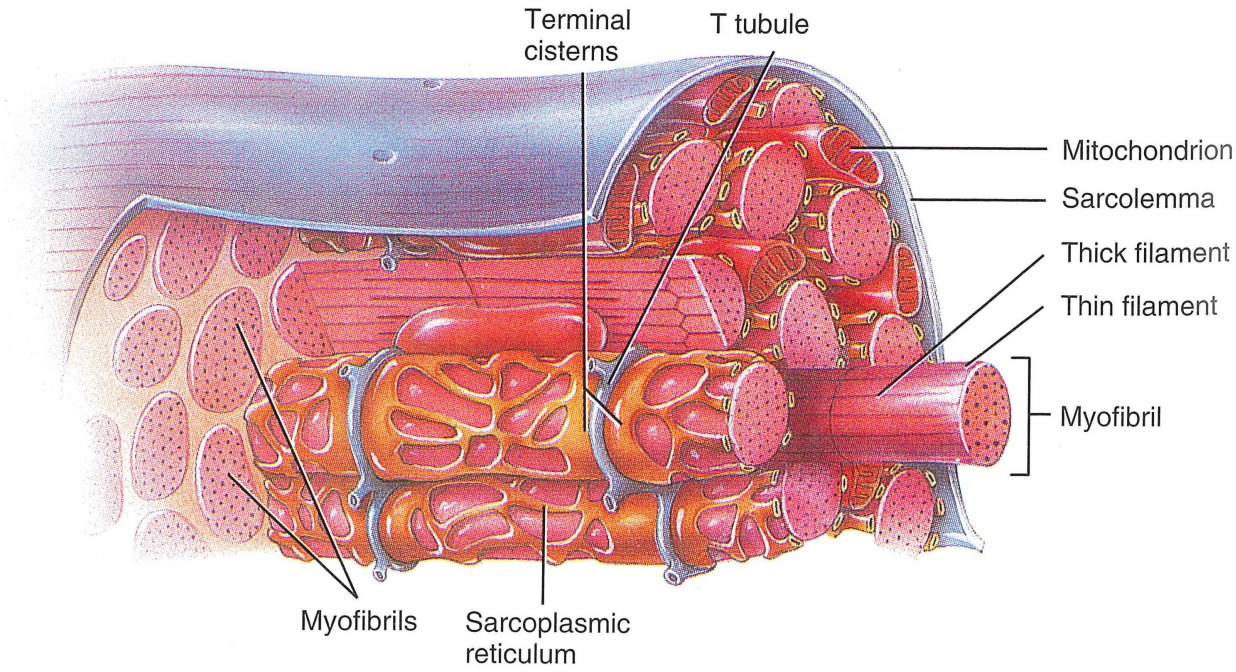

Fig. 2.7: The internal components of a skeletal muscle cell. The T-tubular network can be seen in close contact with the terminal cisternae, specialised segments of the Sarcoplasmic Reticulum. Action Potentials, propagated by the T-tubules, cause a release of calcium ions from the Sarcoplasmic Reticulum, and this calcium can then diffuse to the myofibrils (reproduced from Tortora and Grabowski [111]).

two pyruvate molecules as the by product. This is an anaerobic process, which can be maintained in skeletal muscle for approximately 40 second before the stores of glycogen and glucose are exhausted. In the presence of oxygen the pyruvate molecules are able to be broken down further by the process of oxidative phosphorylation into 34-36 ATP molecules, whereas in anoxic conditions the pyruvate is converted into lactic acid (Subfigure 2.8(b)). The process of glycolysis is very fast compared to oxidative phosphorylation and can thus be used to service high energy requirements for a short period of time, whereas oxidation phosphorylation is required for any activity over 40 seconds and is the process wholly responsible for energy production in endurance activities [111]. The build up of inorganic phosphate in the sarcoplasm of muscle cells is believed to be a cause of fatigue, termed metabolic fatigue. The increased levels of inorganic phosphate inhibit the cycling of crossbridges and reduce the signalling capacity of the cell [105].

2.7 Fibre Type Classification

Differences in factors, such as metabolic properties, give rise to different muscle fibre types which have vastly different performance characteristics. Muscle composition is a dynamic equilibrium where variations in cellular environment and force loading conditions are able to shift the molecular balance, allowing the muscle as a whole to perform more efficiently. These differences are primarily in the composition of the myosin protein, i.e. the isoform and the resulting ATPase activity of the myosin head, and the composition of metabolic enzymes, i.e. predominantly aerobic or anaerobic. As a result of these molecular differences, different types of muscle fibres are able to be distinguished. Knowledge of the overall composition of a muscle gives an indication as to its dynamic performance, fatigue properties, and metabolic requirements.

A number of classifications have been applied to distinguish muscle fibre types. These have been based primarily on either the metabolic properties of the muscle, or the myosin ATPase (mATPase) composition. The relationship between these two fibre type classifications is often confused and not necessarily the same between species or even within the same species at different stages of development [90]. An early classification scheme involved quantify-

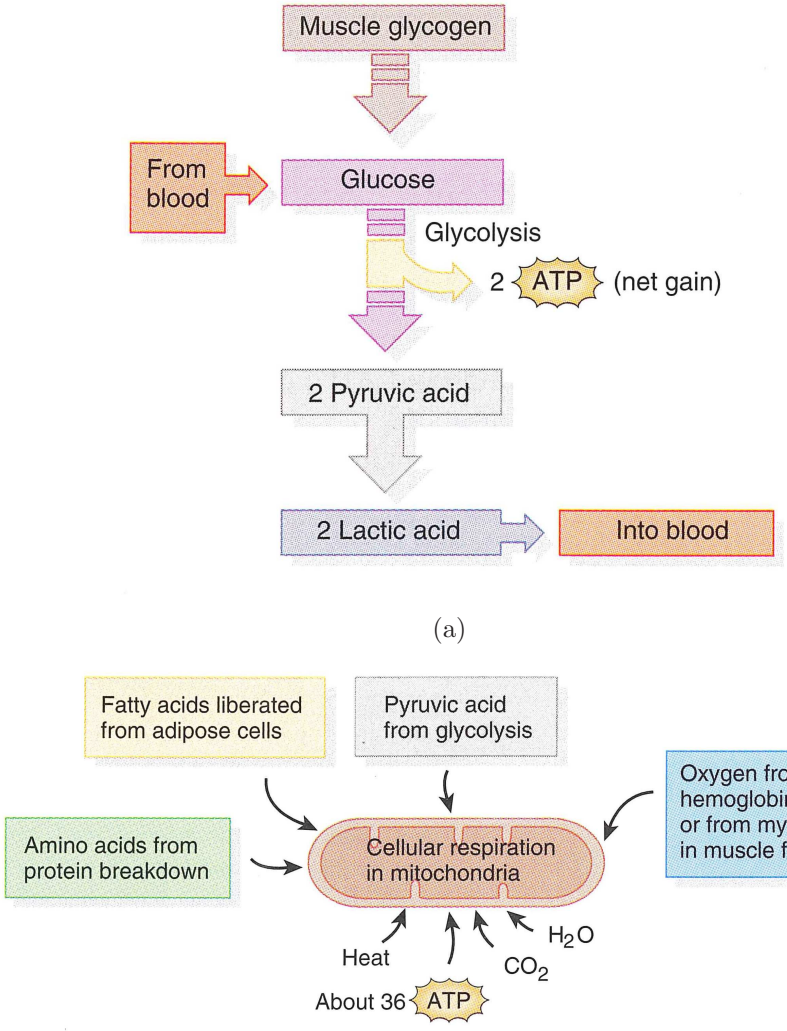

Fig. 2.8: Diagrams showing the steps of Glycolysis (a) and Oxidative Phosphorylation (b). Subfigure (a) shows glucose, which is obtained from the blood or derived from muscle glycogen store, being converted to pyruvic acid and 2 ATP molecules by the process of glycolysis. The pyruvic acid is then converted to lactic acid which enters the blood stream. Subfigure (b) depicts the inputs needed for the mitochondria (the cellular organelle specialised for ATP production) to convert the shown sources of energy into ATP

ing the distribution of enzymes associated with aerobic oxidative or anaerobic glycolytic metabolism. This method was performed on fibres displaying either low or high mATPase activity (type I and type II respectively) and was thus used to distinguish Slow Oxidative (SO), Fast Oxidative Glycolytic (FOG), and Fast Glycolytic (FG) [7, 89].

Depletion of glycogen in a motor unit and the subsequent analysis of the fibres showed an association between FG fibres and fast-fatigable (FF) motor units, FOG fibres and fast-fatigue resistant motor units (FR), and SO fibres and slow fatigue resistant motor units (S) [17]. Further refinements to the mATPase-based classification scheme (using activity levels at various pH levels, or formaldehyde sensitivity) have elucidated a large number of fibre types, e.g. I, Ia, Ib, IIa, IIb, IIc, IIx etc. However, the exact classification of a muscle fibre depends on the method used, the classification boundaries and the species investigated [90]. It should be noted that although in many cases there is a correlation between slow twitch (i.e., type I) fibres and fatigue resistance, this does not always hold true. The same applies to type II muscle fibres and fatigability.

2.8 Electrical Activity

In addition to the structural properties outlined above, skeletal muscle is an electrically active tissue. Each individual muscle fibre is activated by the conduction of signals from the nerves arising from the motor cortex in the brain. The integration of all of the signals controlling the muscle fibres, along with the structural properties of the muscle, give rise to the complex force output of a whole muscle.

2.8.1 The Plasma Membrane and Resting Potential

Skeletal muscle is an electrically active tissue. Its plasma membrane acts as a barrier to charged particles. The plasma membrane consists of a phospho-lipid bi-layer that has a hydrophobic core which inhibits the crossing of water soluble species such as charged ions. Specialised plasma membrane proteins (ionic channels) control the transfer of ions from the intracellular and extracellular

spaces as well as between specialised compartments within the cell itself. The electrochemical gradients set up by the membrane and membrane channels in electrically active tissue allow cells to signal their neighbours, and thus pass information around the body. At rest, skeletal muscle fibres and nerve fibres maintain a constant potential difference across the cell membrane, termed the Resting Membrane Potential. This potential is maintained, and functionally disturbed, by membrane bound ionic channels.

Some of the important channels that set up and maintain the Resting Membrane Potential include the Sodium/Potassium exchanger, the Chloride pump, the Na/Ca exchanger, and the Calcium pump. The Sodium/Potassium exchanger is a membrane bound protein which has ATPase activity. This exchanger pumps sodium out of the cell and potassium into the cell with a stoichiometry of 3/2. At rest the plasma membrane is relatively impermeable to sodium ions and relatively permeable to potassium ions. The sodium-potassium exchanger creates an electro-chemical gradient that allows the potassium ions to diffuse down (out of the cell) until a dynamic equilibrium is reached (see Figure 2.9). The sodium and potassium gradients are the primary energetic sources for electrical signalling between nerve and muscle tissue.

2.8.2 Ion Channels and the Action Potential

A number of important channels are involved in dynamically changing the Membrane Potential of a cell to propagate a signal along it's length. In electrically active tissue, such as skeletal muscle, a propagated membrane depolarisation is termed an Action Potential. The channels primarily responsible for this are the voltage-gated sodium channel, the inward rectifier (a voltage-gated potassium channel), and the delayed rectifier (also a voltage-gated potassium channel). Voltage-gated channels are proteins that change their permeability to specific ions as a result of changes to the surrounding potential. Such channels often switch on at a specific voltage, termed the Threshold Potential of the channel (see Figure 2.10). The voltage-gated sodium channel allows a very rapid influx of sodium into the cell when the Membrane Potential of the cell is depolarised from the Resting Membrane Potential to the Threshold Potential of the sodium channel. This flow of sodium into the cell causes a rapid de-

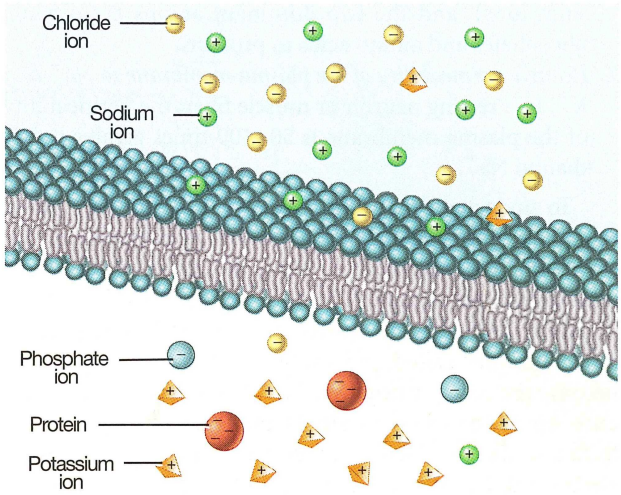

Fig. 2.9: The distribution of ions across the cell membrane are shown. The phospholipid bi-layer is seen separating the extracellular space (top) and the intracellular space (bottom). Higher concentrations of sodium and chloride ions can be seen in the extracellular space, and higher concentrations of potassium can be seen intracellularly (reproduced from Tortora and Grabowski [111]).

polarisation of the membrane. The membrane is brought back to its Resting Membrane Potential by an outflow of potassium ions, mediated by the inward and delayed rectifier potassium channels, and the inactivation of the sodium channel (see Figure 2.11). This controlled fluctuation of the Membrane Potential is termed the Action Potential. Repeated activation of the cell membrane can cause a form of fatigue, termed membrane fatigue. Membrane fatigue is believed to be a result of a break-down in the transmembrane ion fluxes as a result of potassium accumulation in the T-tubules [105].

The Action Potential is propagated down the length of muscle fibres. As a segment of membrane undergoes depolarisation and forms an Action Potential, the diffusion of ions causes down-stream sections of membrane to depolarise to the Threshold Potential of the sodium channels, which is referred to as continuous conduction (see Figure 2.15) [111]. Andreassen *et.al.* showed that Action Potentials in muscle fibres travel at an average velocity of $3.7m/s$ (range $2.6 - 5.3m/s$) [3], while Houtman *et.al.* found that Action Potential velocities ranged between $1.8 - 4m/s$ [59].

Membrane depolarisation, resulting from the Action Potential, induces the opening of two calcium channels important for Excitation-Contraction Cou-

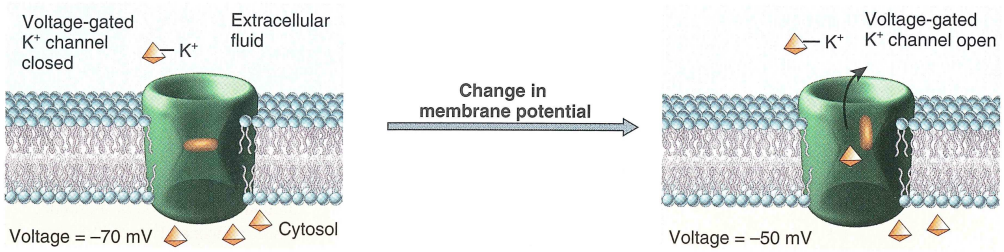

Fig. 2.10: A voltage gated potassium channel in its closed, or inactive, state is shown on the left. On the right, the Membrane Potential has changed (in this case from $-70mV$ to $-50mV$). This change in Membrane Potential reaches the Threshold Potential for the channel and it becomes active, allowing potassium ions to flow across the membrane (right) (reproduced from Tortora and Grabowski [111]).

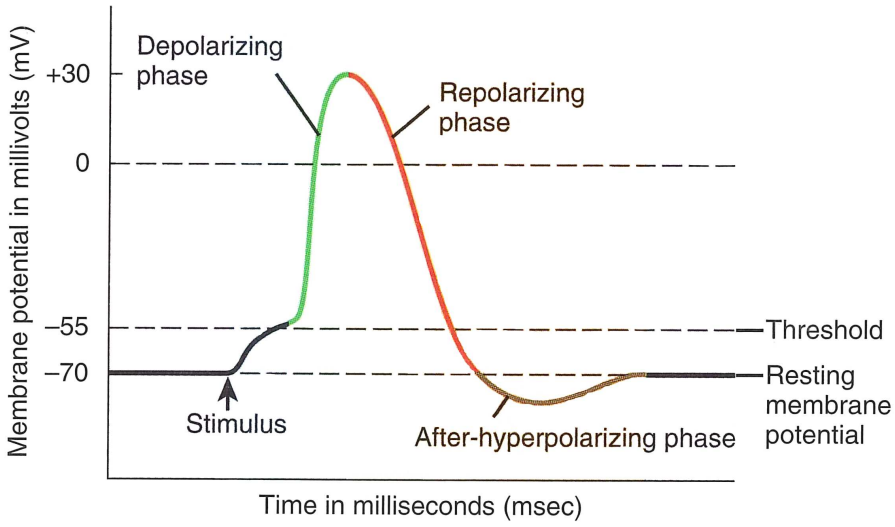

Fig. 2.11: A simple schematic of a nerve Action Potential. The membrane is at Resting Membrane Potential ($-70mV$ in this case) and becomes depolarised by a stimulus to the Threshold Potential ($-55mV$ in this case). The membrane then undergoes the upstroke of the Action Potential (caused by the sodium channel), and is then repolarised by the outflow of potassium ions and the inactivation of the sodium channel during the repolarisation phase. The membrane then returns to the Resting Membrane Potential after a small hyperpolarisation. The Action Potentials in skeletal muscle fibres only differ from nerve Action Potentials quantitatively. Resting Membrane Potential is about $-90V$ to $-80mV$ and the duration of the Action Potential is $1-5ms$ [44] (reproduced from Tortora and Grabowski [111]).

pling (see Section 2.9), the Dihydropyridine receptor (DHPR) which is voltage gated, and the Ryanodine Receptor (RyR) which is located in the membrane of internal cellular structures called the Sarcoplasmic Reticulum (SR). In skeletal muscle it is thought that the RyRs are mechanically coupled to the DHPRs whereas in other muscle types they are Calcium gated channels.

2.8.3 Neurons

All skeletal muscle are innervated by the central nervous system and receive electrical impulses from *alpha*-motor neurons which are controlled by the motor cortex. These are connected to each individual muscle fibre at the neuromuscular junction. The neuromuscular junction is a specialised structure where the nerve terminates in a number of bulbous structures called synaptic end bulbs, which lie in very close proximity to the muscle fibre (see Figure 2.12).

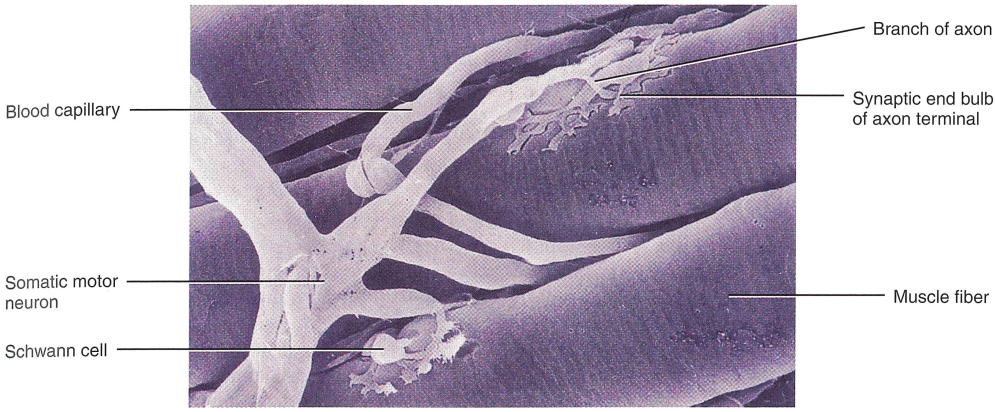

Fig. 2.12: A 1650 times magnification of the neuromuscular junction. The nerve axon can be seen to be terminating in a number of individual synaptic end bulbs in close proximity to the muscle fibres, forming neuromuscular junctions (reproduced from Tortora and Grabowski [111]).

The function of neurons is the transfer of information around the body. Signals, originating from other cells or transduced from external sources, are transferred as trains of Action Potentials. The neurons that control the activation of skeletal muscle are called α-motor neurons. They consist of three main structures, the dendrites, the cell body and the axon (refer Figure 2.13). Input in the form of electrical signals is received by the dendrites. The axon extends

from the cell body and at the junction between the axon and the cell body, Action Potentials form as a result of the input from the dendrites. The axon then propagates the Action Potential to the axon terminal and in the case of α-motor neurons, the axon terminals form the neuromuscular junctions (refer to Section 2.9). The population of α-motor neurons differ in size from about $5\mu m$ to $20\mu m$ [111]. All of these neurons are myelinated fibres. The myelin sheath is a multilayered lipid and protein covering which electrically insulates the axon of a neuron and is a result of specialised cells called Schwann cells wrapping around the axon (see Figure 2.14) [111]. Myelination greatly increases the speed at which the Action Potentials can travel [111] (see below). Not all neurons are myelinated, for example the neurons carrying pain signal from receptors in the skin are unmyelinated.

The gaps between the Schwann cells are called the nodes of Ranvier and are the only locations on the axon where Action Potentials can form. As a result the Action Potential is not continuously propagated as it is in skeletal muscle, but rather it propagates by the method of saltatory conduction (refer Figure 2.15). Saltatory conduction is much faster than continuous conduction and α-motor neurons have conduction speeds of approximately $100m/s$ [111].

2.9 Excitation-Contraction Coupling

At rest, the myosin heads are unable to interact with the actin molecules as they are inhibited by the Troponin-Tropomyosin complex. In order to reduce this inhibition and allow force generation to occur a process termed excitation contraction coupling takes place. When an electrical signal (Action Potential) is propagated to the neuromuscular junction, a release of Calcium ions into the nerve cytoplasm induces the release of the neurotransmitter acetylcholine into the cleft between the nerve bulbous and the muscle fibre. Acetylcholine membrane receptors on the muscle fibre are then activated allowing an influx of Sodium ions, which cause a local depolarisation from the resting Membrane Potential [111].

This change in Membrane Potential causes voltage gated Sodium channels adjacent to the neuromuscular junction to open causing an adjacent membrane depolarisation. At the same time the Sodium pump and the Na/K exchanger

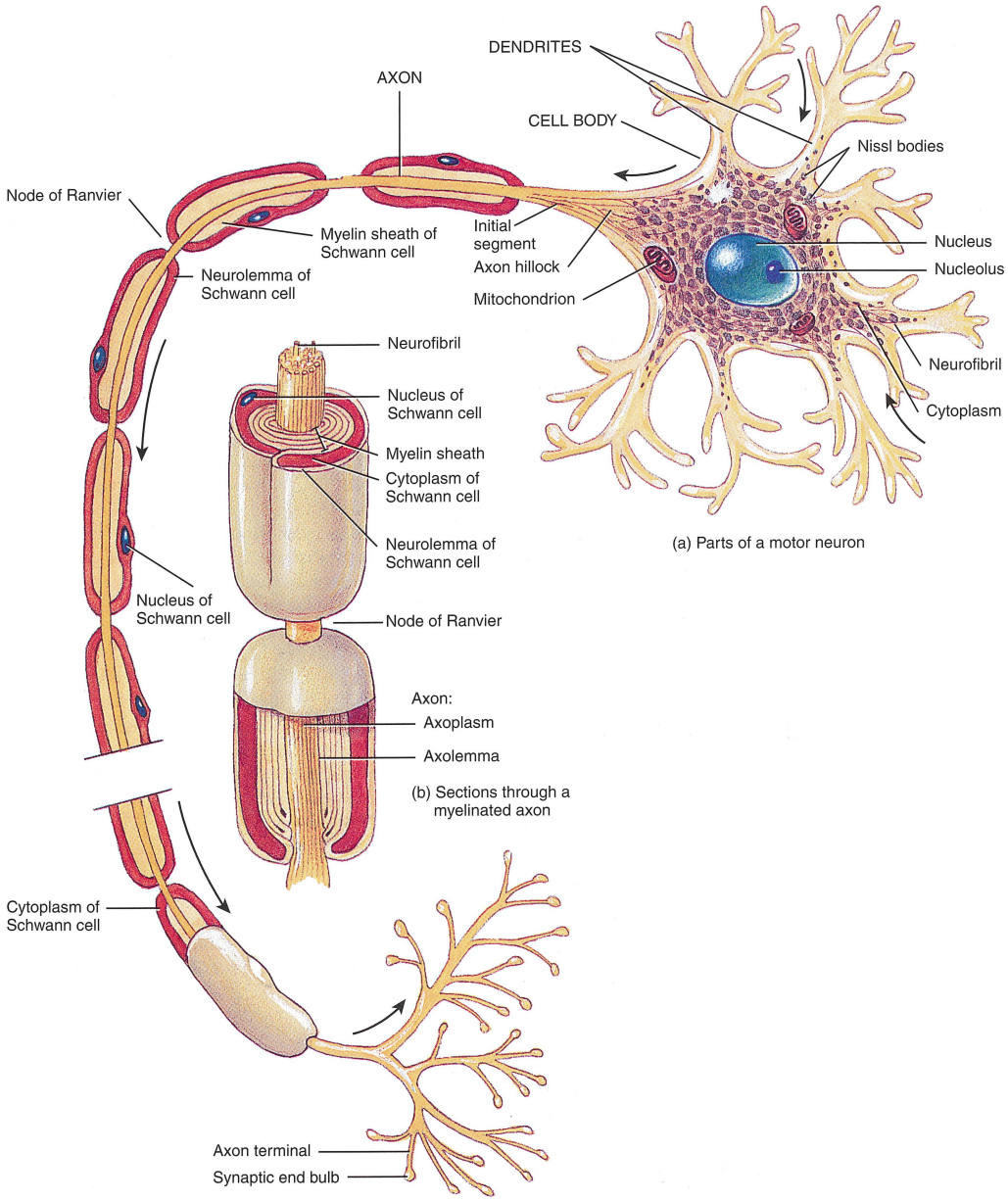

Fig. 2.13: A motor neuron, showing the cell body with the dendrites for receiving input. The axon extends from the cell body to the axons terminals. The myelination of the axon can be seen along with the nodes of Ranvier (reproduced from Tortora and Grabowski [111]).

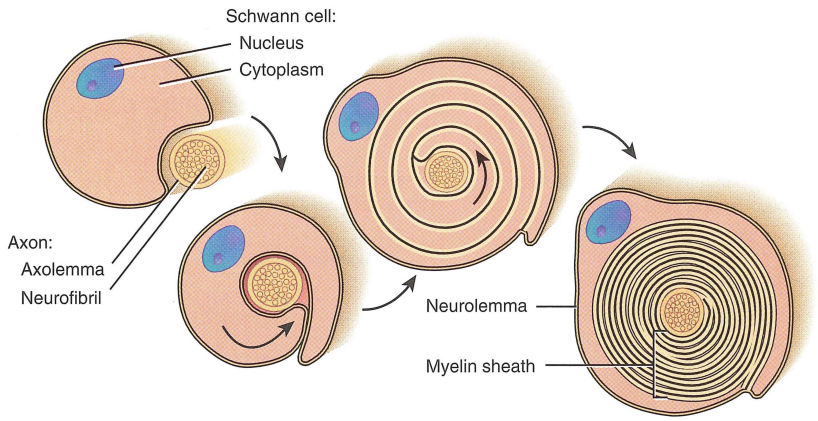

Fig. 2.14: Figure showing the Schwann cells wrapping around the axon of a neuron. The multiple layers of the Schwann cells neurolemma electrically insulate the axon and are needed before the axon is able to efficiently propagate Action Potentials (reproduced from Tortora and Grabowski [111]).

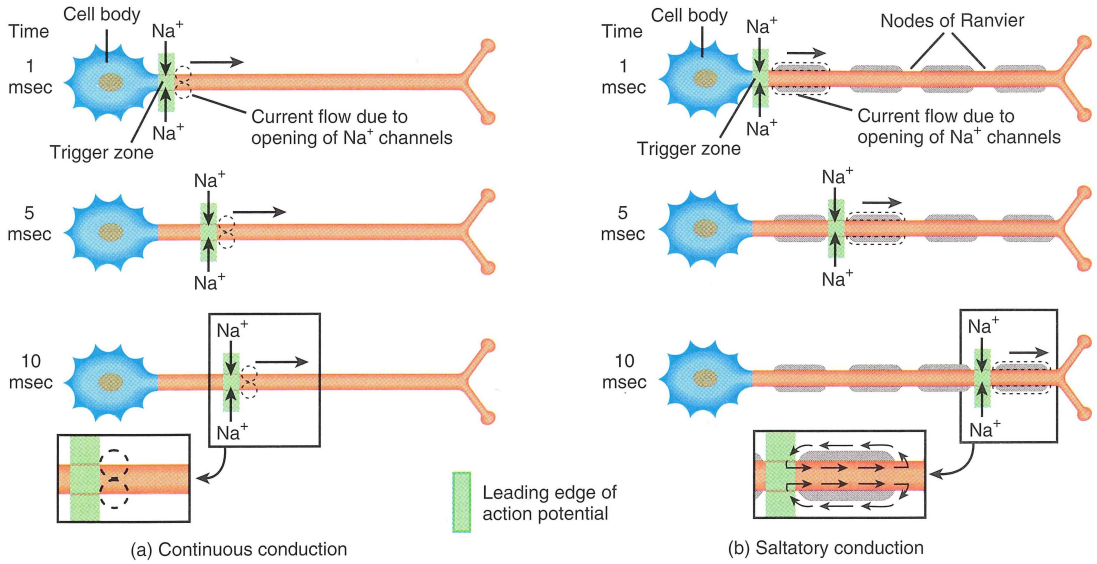

Fig. 2.15: A schematic showing the processes of continuous Action Potential conduction (a) as seen in skeletal muscle fibres and unmyelinated neurons, and saltatory conduction (b) as seen in α-motor neurons. The depolarisation due to the Action Potential in continuous conduction causes depolarisation in the adjacent membrane, causing the sodium channels to open and thus the Action Potential propagates. In (b), the influx of positive ions due to the Action Potential at one node of Ranvier cause a diffusion of these ions down the axon, depolarising the down stream node, inducing an Action Potential (reproduced from Tortora and Grabowski [111]).

work to bring the local membrane back to resting potential. In this way a moving wave of activation is able to travel down the length of the muscle fibre. This is termed the muscle Action Potential.

As the Action Potential travels down the length of the fibre it also propagates down the T-tubular network which carries the signal deep into the cell to where the muscle fibrils are located. The voltage gated dihydropyridine receptors (DHPR) in the T-tubule open during depolarisation and allow an influx of Calcium into the cell. The opening of the DHPRs causes a conformational opening of Ryanodine receptors (RyR) in the adjacent terminal cisternae. This creates a large Calcium flux out of the Sarcoplasmic Reticulum and into the cytosol. This calcium then diffuses through the myofibrils where it binds to troponin-C, causing a conformational change in the troponin-tropomyosin complex, removing the inhibition of myosin interacting with actin. Skeletal muscle troponin requires two bound Calcium ions to remove the inhibition, compared to a single ion in cardiac muscle [111].

At rest, the myosin head, having bound and hydrolysed an ATP molecule is rotated into its high energy state. The ADP and P_i remain bound to the head (step 1 of Figure 2.16). When the myosin head binds to actin, it forms what is known as a crossbridge (step 2), and sequentially releases the P_i and the ADP while undergoing the power stroke (step 3). The release causes the myosin head to rotate back to its low energy position, moving relative to the thin filament in a ratchet like manner, and thus building force and creating displacement. For the myosin to release from the thin filament, ATP must bind. The ATP is once again hydrolysed and the cycle can begin again. This sequence of events is termed the crossbridge cycle. If the myosin head is unable to bind an ATP molecule it is unable to detach. Such circumstances lead to a state of rigour [111].

The force created by a single Action Potential activating a muscle fibre is termed a twitch. The force profile produced by a sarcomere is dependant on the time history of activation. If a second Action Potential activates the release of calcium before the calcium released by the last Action Potential is fully removed from the sarcoplasm, then the calcium transients, and thus the force, will tend to add. This process of addition of subsequent calcium transients is termed wave summation. An unfused tetanus occurs when the process of wave

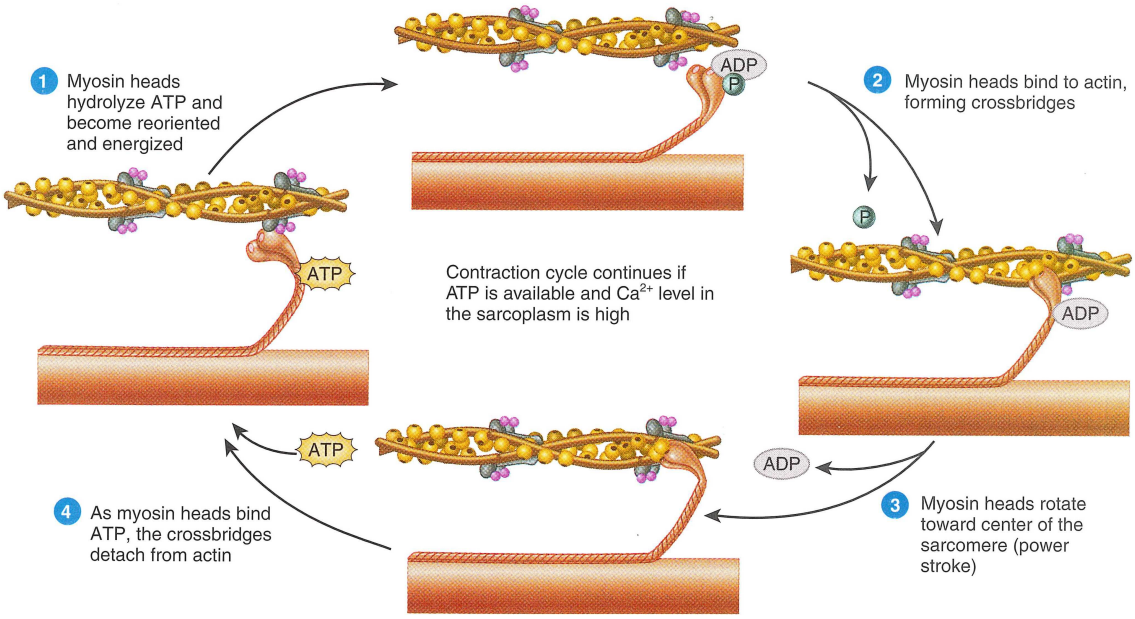

Fig. 2.16: The major steps in the crossbridge cycle. Step 1: A myosin head with bound ATP, hydrolyses it to ADP and inorganic phosphate. The energy from the hydrolysis is used to rotate the head into its high energy state. Step 2: The myosin head then releases the inorganic phosphate and binds to an attachment site on the thin filament. Step 3: The myosin head rotates from its high energy state to a low energy state and release the ADP. The rotation of the head causes the thick and thin filaments to move relative to each other. Step 4: The myosin head binds a molecule of ATP and is then able to detach from the thin filament (reproduced from Tortora and Grabowski [111]).

summation is repeated, and a fused tetanus occurs when the Action Potentials arrive fast enough so that individual twitches cannot be distinguished in the force profile (see Figure 2.17).

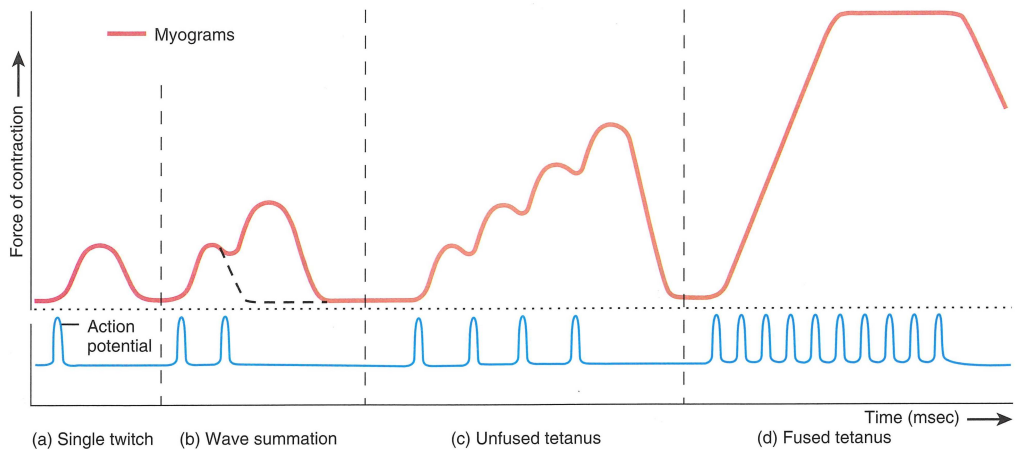

Fig. 2.17: The force output (in red above) of a skeletal muscle fibre as a result of the Action Potential train (in blue below) applied to a muscle. A single muscle twitch is evident in (a) as only a single Action Potential is activating the muscle. The result of wave summation can be seen in (b) as a second stimulus activates the muscle before the effect of the first twitch have dissipated. Further Action Potentials result in an unfused tetanus in (c) and as the frequency of activation increases, the forces as a result of individual Action Potentials cannot be distinguished, giving a fused tetanus (d) (reproduced from Tortora and Grabowski [111]).

2.10 Functional Organisation

The primary functional unit of skeletal muscle is the motor unit. This consists of an α-motor neuron and the population of muscle fibres that the neuron innervates [28, 80, 51]. A motor unit is the finest level of control the central nervous system has over skeletal muscle (Figure 2.18). The α-motor neurons are the terminal extensions of nerves arising from the motor cortex of the brain and are responsible for the transduction of signals from the brain to the muscle. The nerve innervates a number of muscle fibres and on each of them terminates centrally at the motor end plate [4]. As a result the activity of each fibre within a motor unit is the same. The number of fibres within a motor unit is not consistent throughout an individual muscle [80], and instead an exponential

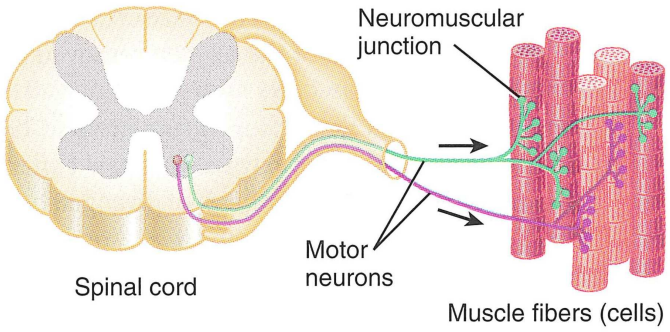

Fig. 2.18: The functional organisation of motor units. Axons of motor units 1 and 2 are seen exciting the spinal cord and then branching to innervate a number of skeletal muscle fibres. Each muscle fibre is only innervated by one motor unit.

distribution of fibres is observed over the motor pool [30]. All muscle fibres within a motor unit tend to be of the same type [3, 28, 51, 80, 116] and the smaller motor units tend to be composed of fibres with slow mATPase activity and oxidative (fatigue resistant) metabolism [53, 116] and are innervated by α-motor neurons of smaller diameter [51]. The force output of a motor unit is highly dependant on the number of fibres contained in it (innervation ratio) [80]. The fibres of a motor unit are, in general, not adjacent but instead distributed throughout an area of the muscle, this is termed the motor unit territory (MUT) [17, 35, 80, 101]. This territory can extend up to the entire cross-section of the muscle but is dependant on the number of fibres (size) of the motor unit [80]. The average density of fibres within a motor unit territory is reasonably consistent [80, 101], and is thought to be around $10 - 30 fibres/mm^2$ [36, 101, 117]. The distribution of motor unit fibres within the motor unit territory is still disputed, with reports of random [13] and clustered distributions [80].

Motor units are recruited to produce force in an order determined by the size principle [53, 51, 80, 116], although there is evidence that this is not always the case [46]. The size principle states that motor neurons of a smaller diameter are recruited before larger diameter neurons and was first proposed by Henneman et. al. in 1965 [53, 52]. This ordering occurs because the pre-synaptic drive (the input from higher levels of the nervous system) has a greater effect on the smaller diameter neurons at lower input levels. This is

because, from Ohm's law, the change in Membrane Potential is proportional to the input resistance of the motor neuron. Small diameter motor neurons have a higher input resistance than larger motor neurons and are thus activated at a lower pre-synaptic drive [28]. As a result, the smaller, fatigue resistant motor units tend to be recruited earlier than the larger and more fatigable motor units. This orderly recruitment scheme results in a smooth gradation of force and increased fatigue resistance compared to a random recruitment scheme or an inverse recruitment scheme (where larger motor units are recruited preferentially) [19, 28]. This recruitment order, although slightly variable due to changes in the activation order of motor neurons of similar thresholds, is conserved through isometric (no change in muscle length), eccentric (lengthening) and concentric (shortening) contractions [28].

The force that a muscle produces is dependant on the number of motor units that are active (i.e. the number of units that have been recruited), and the activity levels (i.e. firing rates) of those motor units [15, 22, 28, 30, 36]. Rate coding is the term used to describe the change in the level of activation of a motor unit, i.e., the frequency of Action Potentials activating the motor unit. Due to the exponential distribution of fibres within motor units, there are a much larger number of small motor units with relatively similar recruitment thresholds. This results in gradation of small forces being mainly achieved by increasing the number of active motor units. Most muscles have an upper limit of motor unit recruitment at approximately 85% of maximum muscle force. That is, all motor units are recruited at, or below, 85% of maximum muscle force, and all further force increase occurs as a result of rate coding [28]. This upper limit of recruitment varies between muscles (e.g. some hand muscles have an upper limit of 60%) but it is also dependant on the movement being performed and the length of the muscle. In dynamic contractions (length changing) and also at reduced muscle lengths, recruitment thresholds are reduced if compared to isometric contractions [87]. Recruitment thresholds are also dependant on the rate of force production. In the case of the Tibialis Anterior muscle, the recruitment threshold of motor units decrease with an increase in the rate of force development. This reduction in recruitment threshold is more pronounced in slower contracting muscles, which likely facilitates those performing faster contractions [28]. The reduction in recruitment threshold

with increasing speed of contraction is seen in all other muscles [62]. Another factor that is thought to influence the recruitment of motor units is the type of motion being performed. The three-dimensional geometry of muscles means that contractions of different areas of the muscle create different joint forces, which has led to the observation of muscle compartmentalisation (activation of distinct fibre pools within the same muscle for different movements) [28, 30].

Firing Rates

It should be noted that there are a number of unresolved issues relating to the time dependant activation of skeletal muscle. Although the mechanism of motor neuron activation is known, the summation of excitatory post synaptic potentials depolarising the cell body to threshold, the in-vivo details are difficult to elucidate. The distribution of excitatory drive over the motor neuron population is not known. There is evidence that the input to the pool is homogeneous [22, 117], as well as non-homogenous [48, 47]. It is also unclear why motor neurons in-vivo rarely fire above $40 - 50Hz$, when maximum tetanic tension is generated by artificially stimulating the same fibres at a frequency closer to $100Hz$ [30]. Speculation exists as to whether the discharge pattern itself might have an effect on total force output or not [30].

The synchronisation of motor unit firing is also an area of active investigation. Motor unit synchronisation refers to the approximately simultaneous activation of motor units, more so than would be expected if each was a completely random event. The cause of motor unit synchronisation is though to be the fact that the excitatory input driving the motor pool comes from related sources, increasing the likelihood of motor neurons firing synchronously [117]. There is evidence that there is a synchronisation effect in some muscles [20, 117], although the level of synchronisation seems to be dependant on the individual muscle and the type of training that it has undergone [26, 28, 117].

In general motor units fire in a conserved order as defined by Henneman [53], with a maximum firing rate of approximately $30 - 50Hz$ [10, 30]. Newly recruited motor neurons fire at around $5 - 10Hz$ [10, 15, 26, 62, 42, 77]. The firing rate is dependant on the level of input to the motor neuron, and increases monotonically with force output [15, 21]. Firing rates of active motor units appear to be independent of whether a new motor unit has become active or

not [62] although there is evidence to the contrary [15].

Interesting effects are seen as muscles fatigue. As the units sustaining a submaximal force begin to fatigue the force output drops, and to compensate excitatory drive to the motor pool is increased [97]. Thus the muscle is able to maintain the force until there are no longer enough remaining motor units able to generate that force. There is likely to be a change in the force profile as the muscle fatigue as larger, stronger, motor units are recruited at low frequencies.

2.11 Functional Electrical Stimulation

Functional Electrical Stimulation (FES) is a technique which, as its name suggests, involves stimulating nerve and/or muscle tissue with electrical signals in order to elicit a functional response. It is used to rehabilitate, or augment, the motor function of individuals who have suffered a disease or injury of the neuromuscular system [93].

Strokes, or cerebro-vascular accidents, can cause a localised loss of motor function by causing the death of an area of cerebral tissue. The mechanism of neurological damage is a reduction in blood flow, or ischemia, causing a lack of oxygen and nutrients and a buildup of toxic compounds. Ischemia can result from vessel occlusion or from haemorrhage and the result can be an infarct [93]. If the infarct is located in the motor cortex, motor function will be inhibited, although rehabilitation is possible as other, functioning, areas of the brain are able to replace the lost functionality [94]. A more permanent from of sensory-motor injury is mechanical damage to central or peripheral neurons, for example spinal cord injury. In the case of a spinal cord or peripheral nerve injury, the connection between the motor cortex (the control centre) and the muscles is severed. The first noninvasive (transcutaneous) system was reported in 1960 and was used to treat foot drop during the swing phase of gait in stroke patients [72]. Stimulation systems to help with the ambulation of thoracic-level spinal cord injury patients were first reported in the 1980's, and one system (Parastep [40]) was FDA approved as a FES ambulation system in 1994 [40].

Functional Electrical Stimulation can be used as a tool in the case of both stroke and spinal cord injury. FES involves stimulating predominantly neural tissue with either cutaneously mounted, or sub-cutaneous electrodes [93], al-

though stimulation of muscle fibres directly is also possible. Electrical impulses are delivered in order to depolarise the target tissue past threshold and thus induce an Action Potential. The electrodes used in a specific functional electrical system can be either mono-polar or bi-polar in configuration and can be designed as constant-current or constant-voltage devices. The electrical pulse delivered to the tissue is usually rectangular and bi-phasic to maximise the activation of the tissue and minimise possible tissue damage [93]. Selection of recruitment level can be achieved by adjusting the charge delivered to the tissue [93].

Functional Electrical Stimulation holds promise as a strategy to assist humans in performing functional movement after central nervous system injuries [65, 93, 40], and has been shown to increase the rate of recovery of function in stroke victims [94]. Electrical stimulation is also effective in reducing or preventing muscle atrophy, or building up the muscle from the atrophied state. It is also possible to use this method to increase carbohydrate oxidation and whole body glucose uptake which may help with glycemic control and insulin sensitivity in patients with Type II diabetes [45].

Given the benefits of using FES as a rehabilitation technique a detailed understanding of the multi-scale effects of this type of intervention is desirable. Further, a full functional characterisation of the limitations inherent to this method would increase the possibility of their elimination or mitigation. One of the limitations of FES is the fact that the recruitment of motor neurons is modified from normal physiological recruitment. Predominantly, the recruitment order of the motor neurons is reversed with the larger diameter motor neurons being activated preferentially [93, 35]. In myelinated axons, the ratio of internodal distance to axon diameter is conserved (internodal distance = 100x diameter [11]). As a result, larger diameter neurons have a greater distance between the nodes of Ranvier and thus, given a constant electric field, there is a greater potential difference between the nodes. As a result, electric fields preferentially activate larger diameter neurons and thus, larger motor units [11].

The inversion of the normal recruitment order causes a loss in fine control and increased muscle fatigue at lower output levels [65]. Some progress has been made into rectifying the inverse recruitment order in implanted electrode

arrays [69], however these techniques are still experimental. In addition to the modification of recruitment order, the level of rate coding for all activated motor units is fixed at the stimulation frequency of the FES system. The effect of this consistent level of rate coding is less well understood than the effect of recruitment inversion, although there is some evidence that synchronous firing of motor units decreases smoothness of the force output and may even reduce the average level of force [117]. The preceding issues are examples of areas where a multi-scale skeletal muscle model can be utilised to investigate the effect that changing muscle activation parameters has on functional output. For further reading on FES refer to [93].

2.12 Electromyography

The surface electromyogram (EMG) uses skin mounted electrodes to record the electrical output of muscles. The EMG represents the sum of all of the electrical outputs of the active motor units, and thus is often considered a global measure of muscle activity [31]. The EMG is therefore a useful tool to evaluate the function of muscles as a whole, but to use EMG to infer the functional properties of muscle, the relationship between the two must be well understood [31].

The output of the EMG depends on a large number of factors, from anatomical features; such as the shape, number, size, conductivity of subcutaneous layers, the distribution and size of the motor unit territories, the number of fibres in the motor units and the length of the fibres, to physiological features; such as the average fibre conduction velocity, the distribution of conduction velocities, the shape of the Action Potential, the number of recruited motor units and the rate coding of the motor units. The EMG output also depends on the electrode configuration used, the relative distance between the electrode and the muscle, and the relative movement between the electrode and the muscle [31]. The use of mathematical models has been very useful in characterising the sensitivity of the EMG output to these parameters [31] and even more diagnostic power could be conferred to the EMG with more detailed models.

2.13 Models of Skeletal Muscle Mechanics

Mathematical models of skeletal muscle functional output vary in form and complexity depending on the aims of the modeller, the limitations on the available body of knowledge, and the resources and time available to solve the model. As a result a large literature base has been created in the area of skeletal muscle modelling. This section will focus on a review of a few of the most influential models and also more recent mechanical modelling frameworks which relate closely to this thesis (a brief introduction into skeletal muscle cellular models can be found in Section 3.1.1).

Models of skeletal muscle mechanics can be divided into two very broad categories, biophysically-based models and phenomenologically-based models. Biophysically-based models aim to represent the output of skeletal muscle as a result of an analysis of intrinsic physiological properties, whereas the phenomenologically-based models use mathematical representations of the input-output properties of muscle without reference to the internal workings of muscle tissue [114]. Thus the parameters in a phenomenologically-based model do not necessarily bare any physical relevance to internal muscle processes.

One of the first, and the most influential, phenomenological-models of the force output of skeletal muscle is the model developed by A.V. Hill in 1938 [56]. Although [56] is primarily concerned with the energetics of muscle contraction, a relationship between the muscle force and the velocity of contraction was found.

$$(a + P)\, V = b\,(P_o - P)\,, \tag{2.1}$$

where a and b are constants obtained from data fitting, P is the muscle force at contraction velocity V and P_o is the maximum isometric force of the muscle. This equation is plotted in Figure 2.19. A schematic of the muscle representation used in [56] can be seen in Figure 2.20.

The experiments used to derive Equation 2.1 were restrictive in their scope. The muscle was only shortened (not lengthened), only maximum muscle activation was used, and the experiments were only conducted over a limited range of muscle lengths near the optimum muscle length. Successive investigations into the behaviour brought more generality to the model by adding the parallel

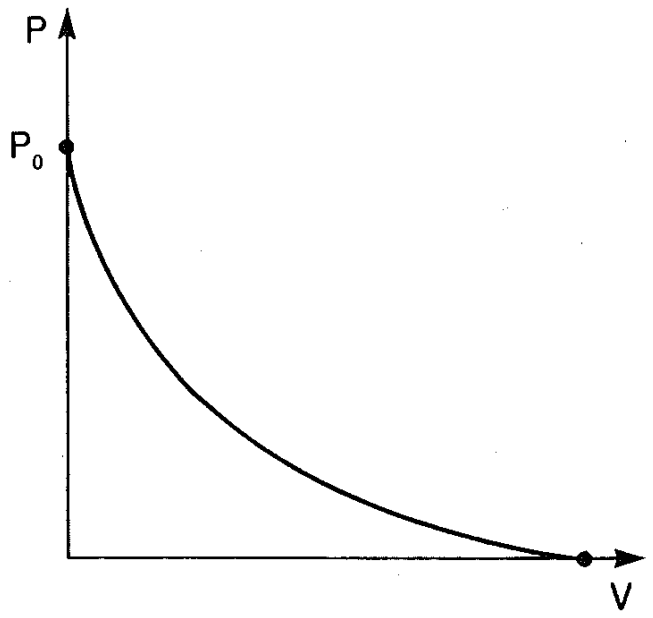

Fig. 2.19: Muscle force verses shortening velocity (from Equation 2.1). The maximum force occurs at zero velocity and the maximum velocity occurs at zero force (reproduced from [115]).

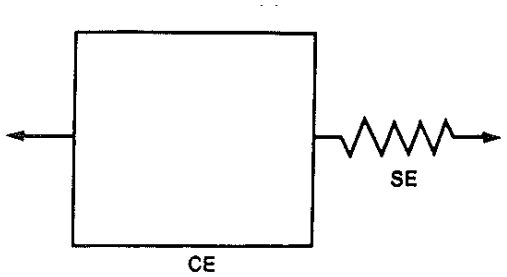

Fig. 2.20: Schematic of the classic 1938 Hill representation of a skeletal muscle. The contractile element (CE) is responsible for the active force and the passive series element (SE) provides the passive force (reproduced from [115]).

elastic element to the Hill 1938 model (Figure 2.21).

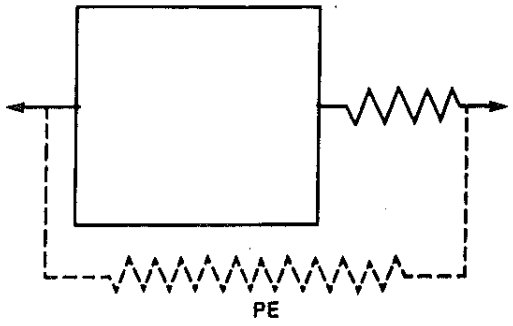

Fig. 2.21: Schematic of the Hill model. A parallel elastic element (PE) has been added to the classic 1938 Hill model (Figure 2.20) (reproduced from [115]).

An example of the implementation of the Hill model can be found in the LifeMOD/BodySIM biomechanics modeller[2]. In this software package, the series elastic element is neglected as it assumes an in-series tendon in the simulations. Thus the total force is composed of a passive and active component, $F_{MUSCLE} = F_{CE} + F_{PE}$, where F_{CE} is the force due to the contractile element and F_{PE} is the force due to the parallel elastic element. The passive force is calculated by, $F_{PE} = \sigma * pCSA$, where σ is the passive stress of the muscle and $pCSA$ is the muscle's physiological cross-sectional area. The active stress is calculated as follows,

$$F_{CE} = A(t) * F_{MAX}.f_H(v_r).f_L(l_r), \tag{2.2}$$

where F_{MAX} is the maximum muscle force, $A(t)$ is the activation state of the muscle (normalised to F_{MAX}), $f_H(v_r)$ is the Hill force-velocity relationship (Equation 2.1), and $f_L(l_r)$ is the muscle force length relationship. It had been noted for many years that the force output of skeletal muscle was dependant on the length of the muscle. The length-tension was elegantly explained by the sliding filament hypothesis, and the effect on force can be seen in Figure 2.22.

The sliding filament hypothesis (and thus myosin crossbridges attaching to the actin filament) was the basis of the biophysically-based Huxley model [60]. This model assumes that each crossbridge can only exist in one of two

[2]www.lifemodeler.com

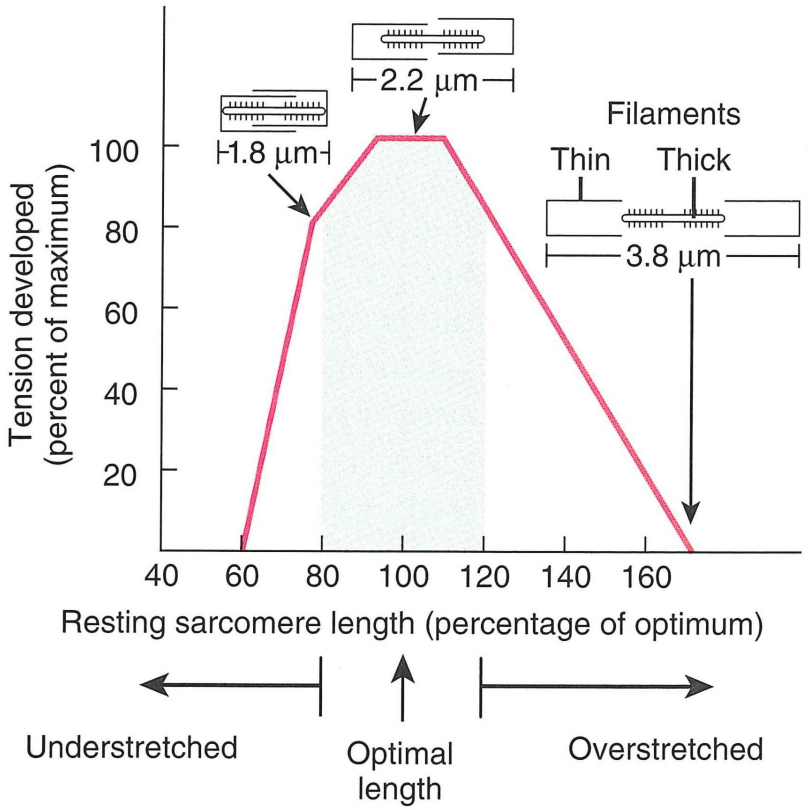

Fig. 2.22: The length-tension relationship of skeletal muscle. At optimum fibre lengths ($2.0\mu m$ to $2.4\mu m$) the maximum overlap between the thick and thin filaments occur, allowing the maximum interaction between the myosin heads and actin, therefore maximum force. As the sarcomere length is lengthened, the number of crossbridges that can form is reduced as the overlap between actin and myosin is reduced. As the sarcomere length is shortened, the thick filament hits the Z-disk and crumples, and this restricts the interaction of actin and myosin. Reproduced from [111]

biochemical states, either attached or detached (see Figure 2.23).

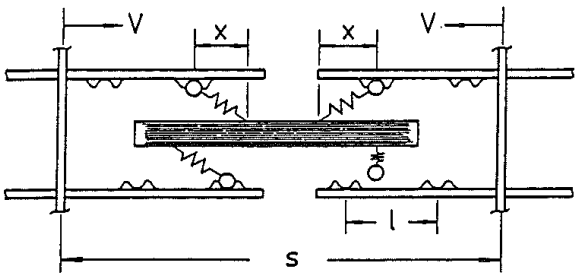

Fig. 2.23: The thick filament can be seen within the sarcomere (S) surrounded by the thin filaments. The crossbridges are represented as balls and are attached to the thick filament via an elastic element. The deformation of this elastic element (X) produces force. The sum of all of the crossbridge forces give the muscle force. Note that l is the distance between actin attachment sites and V is the velocity of the muscle (reproduced from [115]).

In more recent work, the Huxley model has been extended so that the crossbridges are able to exist in more distinct states. For example, the Shorten *et.al.* model [105] uses an eight-state model (six attached states and two detached states). Functionality is conferred to the Huxley type model by relating the transfer of the crossbridges between states by rate variables. These rate variables vary between individual models.

Many mechanical or kinematic models have been developed to represent skeletal muscle contraction. Most of those models are based on the principles of the Huxley or Hill-type models, most of which represent individual muscles as one-dimensional strings. In general, a small number of physiological parameters are used to describe the muscle; these usually include the point of origin, the direction, the average muscle length, and the physiological cross-sectional area. These parameters are often gleaned by investigation via magnetic resonance imaging (MRI) or the examination of cadaver specimens [61, 64]. Muscle forces are then calculated from the physiological cross-sectional area [6, 113] or Hill-type models [2, 66, 86]. Examples of this methodology can be seen in the work of de Zee *et.al.* [23, 24] which takes advantage of the Anybody modelling system[3], as well as LifeMOD/BodySIM, and OpenSim[4] among others. These

[3]www.anybodytech.com
[4]www.simbiome.org

simulations [23] use the known anatomical properties of the muscles and bones of the jaw and use inverse dynamics to calculate the muscle and joint forces as a result of the movement of the jaw (from motion capture). The advantage of using inverse dynamics and lumped-parameter models such as [23] are that the simulations can be run with little computational expense (compared to forward dynamics simulations) and produce accurate predictions of the muscle activation [23]. The limitations to the use of inverse modelling are that musculo-skeletal simulations are generally ill-conditioned, giving a large number of muscle activation solutions to a given movement, and also very little information can be inferred about functional activation of the muscles being simulated.

Recently, full three-dimensional models of muscles have been created by a number of authors [12, 68, 85, 100], and these have led to a fuller understanding of muscle force distributions [100]. The three-dimensional nature of the models allows modifications to the line of muscle action and possible causes of non-linear strains to be investigated [12]. These models are all however based on the principles of continuum mechanics and result in macroscopic models that do not explicitly include any information from finer scales, e.g., the cellular level. The continuum representation also prohibits the use of functional information such as motor unit distributions, fibre firing rates, and different locations of fibre types to name a few.

The Fernandez *et.al.* [33] model of rectus femoris muscle in humans links the mechanical deformation of the muscle to calcium transients. A full three-dimensional description of the muscle fibre angles (bipennate) and the location of the motor end plates were included. Contraction was initiated via the simulation of Action Potential propagation through the nerves to the muscle fibres. The muscle Action Potential triggered the calculation of the calcium transient using,

$$Ca_{actn}(t) = Ca_0 + (Ca_{max} - Ca_0) \cdot \frac{t}{\tau_{Ca}} \cdot e^{(1-t)/\tau_{Ca}}, \tag{2.3}$$

where $Ca_{actn}(t)$ was the level of calcium at time t, Ca_0 was the resting calcium concentration, Ca_{max} was the maximum calcium concentration which was achieved at time $t = \tau_{Ca}$. The calcium concentration $Ca_{actn}(t)$ was then

used to modify the force output of the muscle. However, the Fernandez model does not treat muscle fibres as functionally separate units. Each fibre within the muscle produced the same force output, with a delay calculated from the propagation of an Action Potential through the continuous muscle geometry.

There are a number of muscle models that aim to explicitly represent the recruitment and rate coding of skeletal muscles. Many of these types of models are based on the work of Heckman and Binder [48, 49, 50, 47]. Heckman and Binder [48] details experimental work performed to determine the mechanism of the orderly recruitment of motor units. From Ohm's law, the steady-state synaptic potential, P_{ss}, is equal to,

$$P_{ss} = I_N \cdot R_N, [48] \tag{2.4}$$

where I_N is the effective synaptic current entering the cell and R_N is the total resistance of the cell [48]. The value of R_N is due to the surface area of the neuron, as well as other geometric properties, and has been found to vary approximately 10-fold over motor unit populations [48]. A method for determining I_N directly was presented and this was found to co-vary with R_N with a 2-fold variation in magnitude [48]. In [49], Heckman *et.al.* used a model of 100 simulated motor units to model the input-output function of cat medial gastrocnemius, where the input was I_N and the output was muscle force. The effective synaptic current I_N was used as a parameter that is unrelated to motor neuron geometry to determine the recruitment and firing rates of the motor units [49]. It was assumed that the motor neuron pool received the same I_N, and the recruitment and rate coding of individual motor units were functions of I_N. Recruitment and rate coding were also dependant on intrinsic motor unit properties that varied across the pool. These variations were based on experimental data [49]. They found that, by using this approach, sigmoidal force input-output curves were produced. These curves were believed to be as a result of the inclusion of frequency modulation (rate coding) which was not present in other models [49]. Other researchers have looked at more mathematical descriptions of the input to the motor pool. The work of Nussbaumer *et.al.* [84] looked at ways of simulating the input to the motor pool using physiological information concerning the input currents to the motor neuron cell

body and the recruitment and rate coding that would occur as a result of this input. Gabriel *et.al.* [37] considered the link between the motor pool input and the force output as a novel form of integral equation, and thus theorised that, given a known muscle output, the input characteristics of the system could be deduced.

Fuglevand *et.al.* [36] proposed a model that incorporated descriptions of the recruitment and rate coding of 120 motor neurons in order to represent the force output of a muscle as well as the EMG. The investigation aimed to determine if differences in EMG output in various human muscles were a result of different recruitment strategies. Recruitment thresholds for the motor units were assigned in an exponential fashion with respect to the size of the motor unit, so that there were many small motor units with low activation thresholds, and few large motor units with high activation thresholds. The firing rate of recruited motor units was assumed to linearly increase with excitation [36] (as opposed to Heckman *et.al.* [49] who used a piecewise linear increase in firing rate). The form of recruitment and rate coding used by Fuglevand 1993 is used later in the thesis in a modified form (see Chapter 5). Fuglevand then used a critically damped second order system to represent the force output of individual motor units. The twitch amplitude of the motor units was set depending on the rank of the motor unit. The EMG was calculated from the sum of all motor unit Action Potential trains using assumptions about muscle fibre distributions, conduction velocities, and fibre locations through the area of a muscle [36].

The Livshitz *et.al.* model [73] calculates the current distribution through a muscle stimulated by a specific FES protocol. The current distribution is then used to calculate the level of activation of the muscle, as the area of muscle over the threshold electric field strength value is assumed to be active. The force output was assumed to be proportional to the active number of fibres with respect to the total number of fibres [73]. As a model of muscle activation due to FES, the Livshitz *et.al.* models the method of recruitment in a different manner to the framework proposed in this thesis, but still provides a useful gauge as to the applicability of the proposed framework.

Yao *et.al.* [117] used a modified Fuglevand *et.al.* [36] model to analyse the effect that the synchronisation of motor unit firing had on the force and

EMG of muscle. In order to represent the synchronisation effect, randomly selected motor units were defined to receive an Action Potential at the same time as a reference unit. It was found that increasing the synchronisation of the motor pool had very little effect on the magnitude of the force produced by the muscle, although it did increase the force variability. Synchronisation also increases the magnitude of the EMG [117].

The framework proposed in this thesis makes use of many of the methodologies of the aforementioned models. A subcellular model of the biophysical properties of skeletal muscle allows detail physiological data to drive muscle simulations. A three-dimensional, finite element, representation of the muscle structure means that complex fibre directions, fibre type locations, and functional groupings of fibres can be explicitly represented. Recruitment and rate coding information derived from principles developed by Heckman *et.al.* and Fuglevand *et.al.* allow the framework to exhibit physiological functional activation. The three-dimensional force and deformation of the muscle can be derived as a result of these inputs. The work presented represents one of the most complete modelling frameworks currently available for skeletal muscle research.

Chapter 3

The Formulation of the Modelling Framework

The framework presented in this thesis will be developed in four semi-distinct steps. These steps are;

1. Representing the physiology of a skeletal muscle at a point in space. The solution of the system of Ordinary Differential Equations (ODEs) from the Shorten *et.al.* model [105] will be used.

2. Representing the physiology of a single skeletal muscle fibre. To do this, the Bidomain equations will be combined with the Shorten *et.al.* model.

3. Predicting the mechanical deformation of a three-dimensional muscle geometry given the physiological output of a number of muscle fibres (from Step 2).

4. Representing the unique activation patterns of individual muscle fibres using (a) physiological parameters and (b) parameters describing functional stimulation of the fibre to predict the force output as a result of the activation patterns.

In this chapter the representation of the cellular properties of skeletal muscle as a coupled system of ordinary differential equations is detailed, subsequently the Bidomain equations which are used to model single muscle fibres are derived, and then the governing equations of Finite Elasticity are presented.

The numerical methods used to solve the cellular Ordinary Differential Equations, the Bidomain equations, and the equations of Finite Elasticity are then described. Finally, the software package CMISS is introduced.

3.1 Mathematical Representation of Skeletal Muscle

In this section the set of cellular Ordinary Differential Equations used to represent the physiology of skeletal muscle is described. The derivation of the Bidomain equations and the equations of Finite Elasticity is also outlined. These three sets of equations are used to describe the functionality of skeletal muscle in this thesis.

3.1.1 Cellular Transmembrane Model

As a result of the ever increasing ability to probe the depths of cellular function; mathematical models of the observed processes have become more and more common over the past century. These models have often taken the form of cellular transmembrane models which aim to replicate the observed properties of specific cell types such as cardiac myocytes [9, 83], smooth muscle [32], skeletal muscle [18, 8, 27, 98, 109, 112, 105], and nerve tissue [75], to name a few. These models can be phenomenological, i.e. representing the cell behaviour without any reference to intra-cellular processes, or biophysically-based, i.e. building up the total cell behaviour from representations of sub-cellular processes. Biophysically-based models aim to represent features such as ion fluxes and concentrations of cell species and tend to use ordinary differential equations in time for this purpose.

The Shorten *et.al.* Transmembrane Model

The model that is used in this framework to represent the sub-cellular physiological function of skeletal muscle is the Shorten *et.al.* model [105]. This model was developed to investigate the mechanisms of skeletal muscle fatigue. Further, the differences in fatigue properties between fast and slow type muscle were an area of interest, and so this model is parameterised to represent

the functioning of both fast and slow type muscle. For the purposes of the cell model 'fast type' muscle can be considered to have glycolytic, fatigable metabolic properties and consist of fast type myosin isoform, while 'slow type' muscle is oxidative, fatigue resistant and composed of a slow myosin isoform. The parameters used to represent the fast and slow type muscle came from analysis of the mouse EDL (extensor digitorum longus, which is predominantly fast) and soleus (predominantly slow) muscle, and so the output of the model represents the average function of these two muscles. The EDL and soleus experiments were conducted by electrically stimulating both muscles while holding them at their optimal fibre lengths (the length that resulted in the greatest force output).

The differences between fast and slow twitch muscle types are captured by varying certain model parameters which represent the physical and physiological difference between the two muscle types. For example, fast twitch fibres have greater concentrations of Sarcoplasmic calcium pumps, Ryanodine receptors, Dihydropyrimadine receptors, and membrane ionic channels than slow twitch fibres. The two fibre types also differ in the rate of many cellular processes, for example, calcium release from the Sarcoplasmic reticulum and the cycling of the actomyosin crossbridges occur at higher rates in fast twitch than slow twitch muscle [105].

Two major types of fatigue process are believed to be involved in the change of skeletal muscle function during prolonged activity; membrane and metabolic fatigue. Membrane fatigue is thought to be a result of a break-down in transmembrane ionic fluxes brought about by potassium ion accumulation in the T-tubular network. Metabolic fatigue is believed to come about as a result of inorganic phosphate (Pi) accumulation, which results in slower crossbridge cycling and a reduction in calcium cycling from the sarcoplasmic reticulum to the cytosol.

In order to model these phenomena, the Shorten *et.al.* model uses ordinary differential equations in time to represent the ionic fluxes across the sarcolemmal and T-tubular membranes as well as their respective potentials. The membrane potentials of the sarcolemma, v_S, and the T-tubule, v_T, membranes

are calculated from the following equations,

$$\frac{dv_S}{dt} = \frac{-\left((I_S^{ionic} + I_{stim}) + I_T\right)}{C_m}, \tag{3.1}$$

and,

$$\frac{dv_T}{dt} = \frac{-\left(I_T^{ionic} + I_T/\gamma\right)}{C_m}, \tag{3.2}$$

where t is time (in ms), I_S^{ionic} and I_T^{ionic} are the total ionic currents across the respective membranes, I_{stim} is the stimulus current applied to the model, C_m is the membrane capacitance ($1\mu F/cm^2$ in fast, and $0.58\mu F/cm^2$ in slow twitch muscle), γ is the ratio of T-tubule membrane area to sarcolemma membrane area, and I_T is the access current. The access current is the current that flows from the T-tubular network to the extracellular space. The ionic currents of both membranes are composed of the individual currents due to the chloride, inward rectifier, delayed rectifier, and sodium channels as well as the current due to the sodium potassium exchanger. Each of these currents is dependant on both time and membrane voltage. In this way, the complex interaction of the two membrane potentials is represented. An example of the sarcolemmal membrane potential can be seen in Figure 3.1.

Excitation-Contraction Coupling is achieved in Shorten *et.al.* by linking the gating of the Sarcoplasmic Ryanodine receptors to the T-tubular membrane voltage. The Ryanodine receptors are represented by ten coupled ordinary differential equations (refer to Appendix A). These Ryanodine receptor equations specify a number of open channel states. The calcium concentration in the sarcoplasm of the cell is then calculated as a result of the opening and closing of the Ryanodine receptors (see Section A). The calcium concentrations, along with magnesium and ATP concentrations, form another set of linked ordinary differential equations which also represent the interaction of these species with mobile and immobile buffers such as Calsequestrin, Parvalbumin and Troponin (see Appendix A). Examples of the calcium concentration in the sarcoplasm in fast and slow type muscle as a result of a $40Hz$ stimulation can be seen in Figure 3.2.

The interaction of the actin-myosin complex is modelled as an eight state crossbridge model (similar to Huxley [60]). Three detached states (myosin not

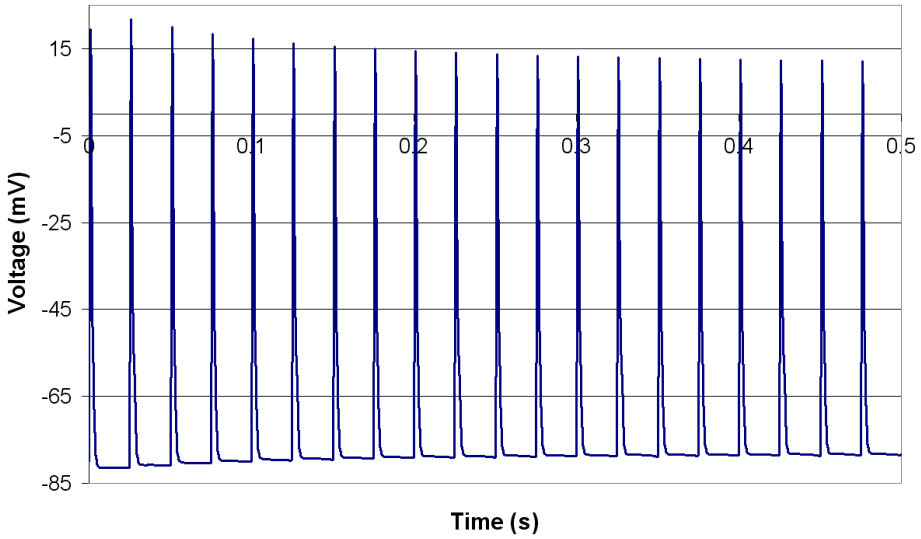

(a)

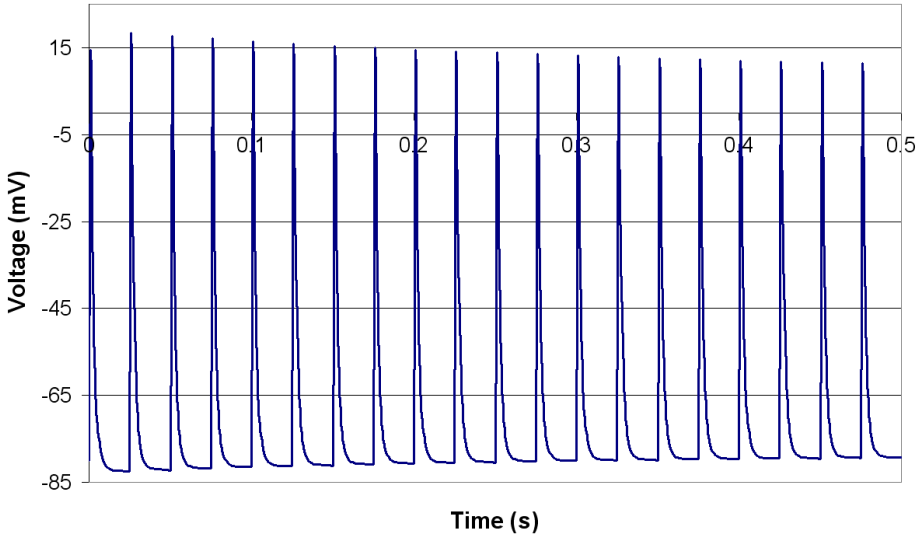

(b)

Fig. 3.1: Output of the sarcolemmal membrane potential of the Fast and Slow muscle types of the Shorten *et.al*. cellular model stimulated at $40Hz$. The membrane potential of the fast and slow type, respectively, are shown in (a) and (b). The fast type muscle shows faster membrane kinetics (this shorter repolarisation time can be seen as the difference in width at the base of the action potentials) but also a faster drop off in peak membrane potential (a result of membrane fatigue).

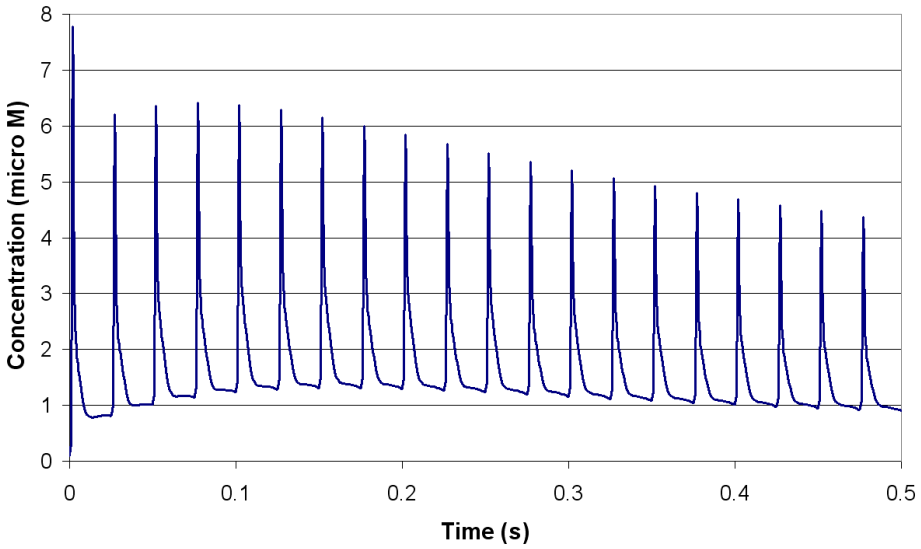

(a)

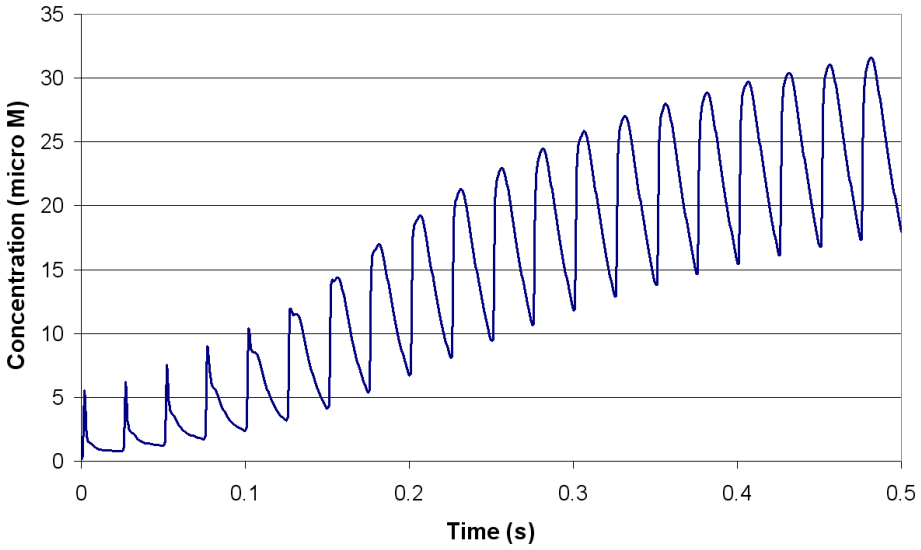

(b)

Fig. 3.2: The Shorten *et.al.* model output for fast and slow muscle type calcium concentration given a $40Hz$ stimulation. The difference in the calcium dynamics can clearly be seen between the fast (a) and slow (b) type muscle.

bound to actin) where the Troponin-Tropomyosin complex blocks binding of actin to myosin are modelled as well as three detached states where no block exits. The two attached states represent crossbridges attached pre-powerstroke and post-powerstroke. Each of the eight equations represents a concentration (e.g. the concentration of detached binding sites unblocked, or the concentration of crossbridges post-powerstroke). The equations of the two attached states are,

$$\frac{dA_1}{dt} = f_o \cdot D_2 - f_p \cdot A_1 + h_p \cdot A_2 - h_o \cdot A_1, \tag{3.3}$$

and,

$$\frac{dA_2}{dt} = -h_p \cdot A_2 + h_o \cdot A_1 - g_o \cdot A_2, \tag{3.4}$$

where A_1 and A_2 are the concentrations of attached crossbridges pre and post-powerstroke respectively (in μM), D_2 is the detached state with two calcium ions bound and no Troponin-Tropomyosin block, and f_o, f_p, h_p, h_o, and g_o are constants governing the rate of transition between the different crossbridge states. These rate constants are different for fast and slow type muscle (see Section A). The attached crossbridge concentration pre and post-powerstroke at $40Hz$ stimulation frequency are plotted in Figure 3.3.

The concentration of buffered and unbuffered inorganic phosphate is also modelled which then feeds back to affect the calcium release from the sarcoplasmic reticulum (see Appendix A). In all, 51 coupled ordinary differential equations are used to model the activation and contraction processes of skeletal muscle on the cellular level.

The different parameterisation of the fast and slow twitch cellular models leads to a difference in the output values of A_1 and A_2 between the two subtypes. Fibre force is primarily related to the diameter of the muscle fibre [71], and as both fast and slow type muscle fibres in humans are approximately the same diameter [54] it is necessary to modify the output A_1 and A_2 values so that both muscle types produce the same maximum force. To achieve this, the maximum A_1 and A_2 values for both slow and fast type muscle were calculated at $40Hz$ (the maximum frequency that would be used during simulations) and each respective parameter was normalised to its respective maximum. The maximum values of each parameter can be seen in Table 3.1. The normalisation of A_1 and A_2 to their respective maximum values in fast and slow type

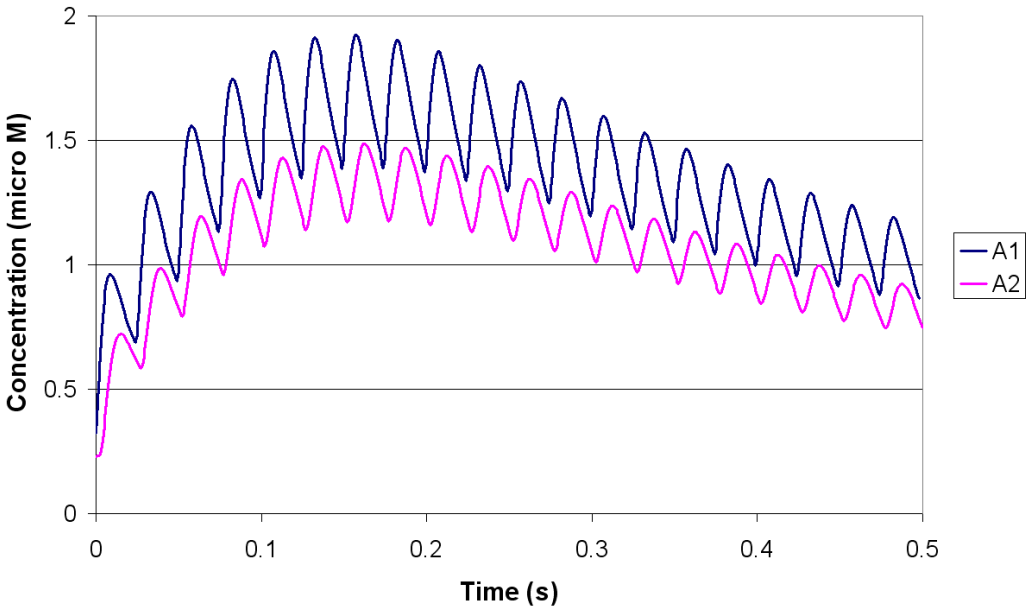

(a)

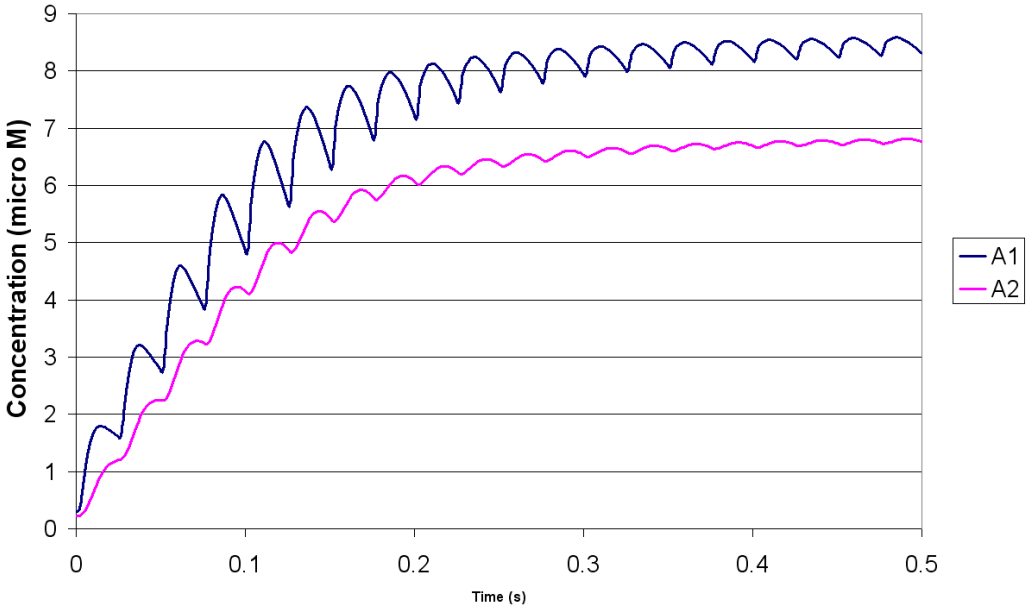

(b)

Fig. 3.3: Pre (A1) and post (A2) powerstroke crossbridge concentrations for fast (a) and slow (b) type muscle. The relatively fast increase in crossbridge concentration is evident in the fast type muscle compared to the slow type, as is the more prominent effect of metabolic fatigue. Note that the scale for slow type muscle ranges between $0-9$, while for fast twitch the scale is from $0-2$.

Table 3.1: The maximum A_1 and A_2 values for fast and slow twitch muscle stimulated at $40Hz$

Concentrations in μM	Fast Type	Slow Type
A_1	1.95	8.8
A_2	1.5	7

muscle increased the difference in the initial values of the parameters. The difference in initial values of A_1 and A_2 between muscle types results in variations in the resting force values of the two muscle types (this difference can be seen in Figure 5.8 of Section 5).

3.1.2 The Bidomain Formulation

Electrophysical models have been used for more than half a century to elicit a deeper understanding of the properties and function of active tissue. The most influential model has been the Hodgkin-Huxley model of the squid giant axon [58], which explicitly represented the effect of specific membrane channels on the passage of ions across the impermeable cellular membrane, and the resulting change in membrane potential. Hodgkin and Huxley also described the squid axon as a leaky cable and used this analogy to derive a model for the propagation of an action potential along its length. This is known as the cable equation [58, 96].

The cable equation can be extended into higher dimensions, which allows for a greater range of electrophysiological problems including those that involve spatially dependent material properties [5] and are termed the Bidomain equations. The Bidomain equations are a continuum approximation of the tissue properties and were first proposed by Schmitt [103]. The Bidomain equations have become increasingly popular in the cardiac modelling field where the three dimensional structure of the tissue has a major effect on its functional response [5, 96]. The Bidomain equations describe the tissue as two inter-penetrating domains, representing the intracellular and extracellular spaces. These two domains are defined as having potential fields ϕ_i and ϕ_e, and conductivity tensors σ_i and σ_e representing the intra and extra-cellular spaces respectively. The derivation of the Bidomain used in this work results in two equations, the first describes the extracellular potential while the second is a reaction diffusion

equation in terms of the cellular transmembrane potential, which is obtained from the sum of the ionic currents in the cellular transmembrane model.

This thesis uses the Bidomain formulation to model the physiology of skeletal muscle fibres (refer to Chapter 4). The Shorten *et.al.* transmembrane model is linked with the Bidomain equations (specifically (3.20)), and thus the current flow is influenced by the reaction of the Shorten *et.al.* cell model, and vice versa.

The initial step in the derivation of the Bidomain equations is the definition of the transmembrane potential, V_m, which, by convention, is,

$$V_m = \phi_i - \phi_e. \tag{3.5}$$

The only path that current can take between the two domains is through the cellular membrane. From Ohm's law

$$\mathbf{J} = \frac{1}{R} * \mathbf{E}, \tag{3.6}$$

where $\mathbf{E}$ is the electrical field strength, $\mathbf{J}$ is the current density and R is the resistivity. If the quasi-static assumption is used the electric field can be expressed as the gradient of a scalar potential field, i.e. $\mathbf{E} = -\nabla\phi$. Substituting $\mathbf{E}$ into (3.6), and expressing the resistivity as a conductivity ($\sigma = 1/R$), leads to

$$\mathbf{J}_i = -\sigma_i \nabla\phi_i, \tag{3.7}$$

$$\mathbf{J}_e = -\sigma_e \nabla\phi_e. \tag{3.8}$$

Any current that leaves one domain must enter the other, hence the change in current density in each of the domains must be equal and opposite i.e.

$$-\nabla \cdot \mathbf{J}_i = \nabla \cdot \mathbf{J}_e = A_m I_m, \tag{3.9}$$

where A_m is the surface to volume ratio of the cell membrane and I_m is the transmembrane current density per unit area, as calculated from the cellular equations. Combining (3.7) and (3.8) with (3.9) gives two equations that

represent the conservation of current densities

$$\nabla \cdot (\sigma_i \nabla \phi_i) = A_m I_m, \tag{3.10}$$

$$\nabla \cdot (\sigma_e \nabla \phi_e) = -A_m I_m. \tag{3.11}$$

This implies that

$$\nabla \cdot (\sigma_i \nabla \phi_i) = -\nabla \cdot (\sigma_e \nabla \phi_e). \tag{3.12}$$

Subtracting $\nabla \cdot (\sigma_i \nabla \phi_e)$ from both sides gives

$$\nabla \cdot (\sigma_i \nabla \phi_i) - \nabla \cdot (\sigma_i \nabla \phi_e) = -\nabla \cdot (\sigma_e \nabla \phi_e) - \nabla \cdot (\sigma_i \nabla \phi_e). \tag{3.13}$$

Then (3.5) can then be used to rewrite (3.13) as,

$$\nabla \cdot (\sigma_i \nabla V_m) = -\nabla \cdot ((\sigma_i + \sigma_e) \nabla \phi_e). \tag{3.14}$$

Equation 3.14 is the first of the two Bidomain equations and is used to calculate the extracellular potential field given a transmembrane potential distribution. The current flowing across the cellular membrane can be represented by the sum of a time dependant capacitive current and the current due to ionic flow.

$$I_m = C_m \frac{\partial V_m}{\partial t} + I_{ion}, \tag{3.15}$$

where C_m is the membrane capacitance per unit area and I_{ion} is the sum of all of the currents calculated from the cellular transmembrane models. Combining (3.10) and (3.15) yields,

$$\nabla \cdot (\sigma_i \nabla \phi_i) = A_m \left(C_m \frac{\partial V_m}{\partial t} + I_{ion} \right). \tag{3.16}$$

In order to convert (3.16) into an equation with V_m as a dependant variable, $\nabla \cdot (\sigma_i \nabla \phi_e)$ is subtracted from both sides resulting in,

$$\nabla \cdot (\sigma_i \nabla (\phi_i - \phi_e)) + \nabla \cdot (\sigma_i \nabla \phi_e) = A_m \left(C_m \frac{\partial V_m}{\partial t} + I_{ion} \right). \tag{3.17}$$

Substituting $\phi_i - \phi_e = V_m$ into (3.17), one obtains,

$$\nabla \cdot (\sigma_i \nabla V_m) + \nabla \cdot (\sigma_i \nabla \phi_e) = A_m \left(C_m \frac{\partial V_m}{\partial t} + I_{ion} \right). \tag{3.18}$$

Equation (3.18) is known as the second Bidomain equation and is used to calculate the transmembrane potential. Note that it is possible for a stimulus current to be added to either of the two domains which gives,

$$\nabla \cdot (\sigma_i \nabla V_m) = -\nabla \cdot ((\sigma_i + \sigma_e) \nabla \phi_e) + I_{s1}, \tag{3.19}$$

and

$$\nabla \cdot (\sigma_i \nabla V_m) + \nabla \cdot (\sigma_i \nabla \phi_e) = A_m \left(C_m \frac{\partial V_m}{\partial t} + I_{ion} \right) - I_{s2}, \tag{3.20}$$

where I_{s1} and I_{s2} are the applied stimulus currents.

3.1.3 Finite Elasticity - Linking Cellular Models to Force

A representation of the resultant muscle force, as a result of muscle activation, is produced by the cellular model. This takes the form of the concentration of actomyosin crossbridges pre- and post-powerstroke. However, in order to calculate the force of a whole muscle containing large numbers of motor units composed of many fibres and different fibre types, a solution method is required that is able to integrate the total muscle force from the individual contributions of each fibre. In order to calculate the force and deformation of a whole muscle, the governing equations of finite elasticity were chosen. The solution of muscle mechanics via this route has been used previously and has been shown to be highly effective and efficient [99].

The Derivation of the Equations of Finite Elasticity

Let us consider a body in a reference (undeformed or initial) configuration. This body can be thought of as being made up of an infinite number of particles. Under an applied load the body deforms to the deformed, or final, configuration. The motion of the body from one configuration to another can be defined mathematically by,

1. Kinematic relationships - define the strain, or deformation, of the body in terms of displacement gradients.

2. Stress equilibrium - equations that are derived from the principles of conservation of linear and angular momentum.

3. Constitutive relations - relate the body strains to the body stresses. The constitutive relationships are dependant on the specific material being represented.

4. Boundary conditions - define the specific loading condition of the problem.

Kinematic Relationships

The motion of any body can be related to two different coordinate systems. The *spatial* or *Eulerian* coordinate system refers to a coordinate system that is fixed in space. A *material* or *Lagrangian* coordinate system is one where the coordinates move and deform with the material being analysed. As an analogy, if one was to be sitting on the side of a river watching a raft move though the rapids, the watcher would be consider to be viewing the raft using a *spatial* reference system, whereas, if the viewer was on the raft, moving with it through the rapids, a *material* frame of reference would be used.

Consider a line segment $\Delta\mathbf{X}$ in the undeformed configuration being deformed to $\Delta\mathbf{x}$. The deformation of the line segment can be expressed using the deformation gradient tensor $\mathbf{F}$ which maps the two segments by $\Delta\mathbf{x} = \mathbf{F}\Delta\mathbf{X}$, or $\Delta\mathbf{X} = \mathbf{F}^{-1}\mathbf{x}$, where,

$$\mathbf{F} = \left[F_M^j\right] = \left[\frac{\partial x_j}{\partial X_M}\right] = \left[\frac{\partial(X_j + u_j)}{\partial X_M}\right], \quad \text{with} \quad j, M = 1, 2, 3. \tag{3.21}$$

Here $\mathbf{u}$ is the displacement from $\mathbf{X}$ to $\mathbf{x}$. The deformation gradient $\mathbf{F}$ describes the mapping between two points. The change in length of two line segments can be described by the Cauchy-Green deformation tensor ($\mathbf{C}$) which is derived as follows. Consider two line segments $\mathbf{X}^1$ and $\mathbf{X}^2$ being deformed to $\mathbf{x}^1$ and

$\mathbf{x}^2$ respectively. This can be written,

$$\begin{aligned} \mathbf{x}^1 \cdot \mathbf{x}^2 &= \left(\mathbf{F}\Delta\mathbf{X}^1\right) \cdot \left(\mathbf{F}\Delta\mathbf{X}^2\right) \\ &= \Delta\mathbf{X}^1 \left(\mathbf{F}^T\mathbf{F}\right) \Delta\mathbf{X}^2 \\ &= \Delta\mathbf{X}^1\mathbf{C}\Delta\mathbf{X}^2, \end{aligned}$$

where $\mathbf{C} = \mathbf{F}^T\mathbf{F}$. The Cauchy-Green deformation tensor is a symmetric, positive definite matrix and is expressed in terms of material coordinates. In three-dimensions it is a 3x3 tensor, and has three scalar combinations of its components known as the *principle invariants*, which are unchanged by coordinate rotations. The invariants are,

$$I_1 = tr\mathbf{C} \tag{3.22}$$

$$I_2 = \frac{1}{2}\left[(tr\mathbf{C})^2 - tr\mathbf{C}^2\right] \tag{3.23}$$

$$I_3 = det\mathbf{C}, \tag{3.24}$$

where $tr\mathbf{C}$ is the trace of $\mathbf{C}$ (the sum of the diagonal components), and $det\mathbf{C}$ is the determinant of $\mathbf{C}$. Another measure of the change in length of line segments from the undeformed to the deformed configuration is the Green-Lagrange strain tensor $\mathbf{E}$. This tensor provides information about the change in the squared length of elements and is defined as,

$$\mathbf{E} = \frac{1}{2}(\mathbf{C} - \mathbf{I}), \tag{3.25}$$

where $\mathbf{I}$ is the Lagrangian identity tensor.

Stress Equilibrium

Stress is, by definition, the force acting over an area. Given the deformed and the undeformed geometries, we are able to define a number of stress relationships. The true stress acting on a body can be defined by the Cauchy stress tensor σ^{ij}, where index i denotes the direction normal to the surface on which the stress acts and j indicates the direction of the stress component. It is a symmetric 3x3 tensor composed of the three normal forces, σ_{11}, σ_{22} and σ_{33}, and three unique shear forces, σ_{12}, σ_{13} and σ_{23}. The Cauchy force represents

the force per unit area in the deformed configuration.

The 1^{st} *Piola-Kirchhoff* stress tensor, P^{Mj}, represents the force acting on a surface in the deformed configuration measured with respect to the undeformed surface. Index M indicates the normal to the undeformed surface and j is the force direction in the deformed configuration. The 1^{st} *Piola-Kirchhoff* stress tensor is used when the force is measured in the deformed configuration while the area over which the force acts is measured from the undeformed configuration. The 1^{st} *Piola-Kirchhoff* stress tensor can be obtained from the Cauchy stress as follows,

$$P^{Mj} = J\frac{\partial X_M}{\partial x_i}\sigma^{ij}, \tag{3.26}$$

where J is the Jacobian matrix of the transformation for undeformed to deformed coordinates,

$$J = det\mathbf{F} = \sqrt{I_3}. \tag{3.27}$$

The 2^{nd} *Piola-Kirchhoff* stress tensor, T^{MN}, represents the force per unit area in the undeformed configuration (in the direction normal to the undeformed surface M) acting on the undeformed surface. This tensor is used to represent material behaviour at a point, independent on rigid body rotation. The 2^{nd} *Piola-Kirchhoff* stress tensor must be transformed into 1^{st} *Piola-Kirchhoff* stresses to be used in equilibrium equations, as the 2^{nd} *Piola-Kirchhoff* tensor requires a spatial frame of reference. The 2^{nd} *Piola-Kirchhoff* stress tensor is derived from the Cauchy tensor as follows,

$$T^{MN} = J\frac{\partial X_M}{\partial x_i}\sigma^{ij}\frac{\partial X_N}{\partial x_j}, \tag{3.28}$$

and can be found from the 1^{st} *Piola-Kirchhoff* stress tensor by,

$$T^{MN} = P^{Mj}\frac{\partial X_N}{\partial x_j} \tag{3.29}$$

Consider a body acted on by body forces $\mathbf{b}$ per unit volume (V) and traction forces $\mathbf{t}$ per unit area (S). Using the conservation of linear momentum, the time rate of change of the total linear momentum for a set of body particles is equal to the vector sum of all the external forces acting on the particles. Thus,

$$\int_S \mathbf{t}\, dS + \int_V \rho \mathbf{b}\, dV = \frac{d}{dt} \int_V \rho \mathbf{v}\, dV, \tag{3.30}$$

where $\mathbf{v}$ is the velocity vector and ρ is the mass density in the deformed body. In this thesis the inertial effects are assumed to be negligible, therefore from (3.30),

$$\int_S \mathbf{t}\, dS + \int_V \rho \mathbf{b}\, dV = 0. \tag{3.31}$$

The traction vector ($\mathbf{t}$) can be written in terms of the Cauchy stresses,

$$\mathbf{t} dS = \sigma^{ij} \hat{n}_i \mathbf{i}_j dS, \tag{3.32}$$

where $\hat{\mathbf{n}} = \hat{n}_j \mathbf{i}_j$ is the unit normal which is projected on the orthogonal Cartesian reference coordinate system. The body force $\mathbf{b}$ can also be written in component form as $\mathbf{b} = b^j \mathbf{i}_j$, which, when substituted into (3.31) along with (3.32), gives,

$$\int_S \sigma^{ij} \hat{n}_i\, dS + \int_V \rho b^j\, dV = 0. \tag{3.33}$$

The divergence theorem can then be used to rewrite (3.33) as,

$$\int_V \left[\frac{\partial \sigma^{ij}}{\partial x_i} + \rho b^j \right] dV = 0. \tag{3.34}$$

If it is assumed that the integral in (3.34) is continuous within an arbitrary volume, the equation can be simplified to,

$$\frac{\partial \sigma^{ij}}{\partial x_i} + \rho b^j = 0. \tag{3.35}$$

Equation (3.35) is Cauchy's first law of motion, and can be written in terms of the 2^{nd} *Piola-Kirchhoff* tensor using (3.28),

$$\frac{\partial}{\partial X_M} \left(T^{MN} \frac{\partial x_j}{\partial X_N} \right) + \rho_o b^j = 0. \tag{3.36}$$

The mass density, ρ_o, of the undeformed volume, V_o, is related to the deformed bodies mass density, ρ, by $\rho_o = J\rho$ (conservation of mass).

The principle of virtual work is used to solve (3.36). If a body is in static

equilibrium, then the sum of all of the forces acting on the body is 0. If we consider adding an arbitrary displacement, $\delta\mathbf{u}$, to each particle in the body, then the total work done also must be 0. As a result, the sum of the internal ($\mathbf{s}$) and external ($\mathbf{t}$) traction forces must be 0, giving,

$$\int_{S_2} \mathbf{s} \cdot \delta\mathbf{u}\, dS = \int_S \mathbf{t} \cdot \delta\mathbf{u}\, dS, \tag{3.37}$$

where S_2 is the surface which is not subject to displacement boundary conditions. The virtual displacements may be decomposed into $\delta\mathbf{u} = \delta\mathbf{u}\mathbf{i}_j$. Equation 3.32 can be used to rewrite the surface traction,

$$\int_{S_2} \mathbf{s} \cdot \delta\mathbf{u}\, dS = \int_S \sigma^{ij}\hat{n}_i \delta u_j\, dS. \tag{3.38}$$

The right hand side of (3.38) can be expanded using Gauss's theorem to,

$$\int_{S_2} \mathbf{s} \cdot \delta\mathbf{u}\, dS = \int_V \left[\frac{\partial\sigma^{ij}}{\partial x_i}\delta u_j + \sigma^{ij}\frac{\partial\delta u_j}{\partial x_i}\right] dV. \tag{3.39}$$

Substituting (3.35) into (3.39) and re-arranging terms results in,

$$\int_V \sigma^{ij}\frac{\partial\delta u_j}{\partial x_i}\, dV = \int_V \rho b^j \delta u_j\, dV + \int_{S_2} \mathbf{s} \cdot \delta\mathbf{u}\, dS, \tag{3.40}$$

which can be written in terms of the 2^{nd} *Piola-Kirchhoff* stresses as,

$$\int_V T^{MN}\frac{1}{j}\frac{\partial x_j}{\partial X_M}\frac{\partial\delta u_j}{\partial X_N}\, dV = \int_V \rho b^j \delta u_j\, dV + \int_{S_2} \mathbf{s} \cdot \delta\mathbf{u}\, dS. \tag{3.41}$$

When considering non-homogeneous, anisotropic materials, it is often more useful to describe the aforementioned quantities in terms of a local material coordinate system. This allows tensor entries to be easily associated with structural features of the body in question. For example, when considering skeletal muscle, it is convenient to associate stress tensors with the muscle fibre direction at every point throughout the muscle, allowing for a constant definition of the material properties. This results in the Green strain tensor becoming $[E_{\alpha\beta}]$ and the 2^{nd} *Piola-Kirchhoff* stress tensor becoming $\left[T^{\alpha\beta}\right]$, which gives the weak form of stress equilibrium in terms of the local coordinate

system, ν_α, as

$$\int_{V_e} T^{\alpha\beta} F^j_\beta \delta u_{j,\alpha}\, dV_e = \int_{V_e} \rho_0 (b^j - f^j)\delta u_j\, dV_e + \int_{S_e} t^j \delta u_j\, dS_e. \tag{3.42}$$

where F^j_β are the components of the deformation gradient with respect to the ν_α-coordinate system, $\delta u_{j,\alpha}$ are the virtual displacement expressed relative to the reference coordinate system and differentiated with respect to the ν_α-coordinate system, ρ_0 is the material density in the reference configuration, b^j and f^j are the body force and acceleration vector and t^j is the traction force on the surface S_e, of the volume V_e.

Constitutive Relations

The constitutive relationship of a material defines the deformation of the material under loading conditions. That is, the constitutive law relates stress (σ, $\mathbf{P}$ or $\mathbf{T}$) to strain ($\mathbf{F}$, $\mathbf{C}$ or $\mathbf{E}$) in a body. These laws are based on the results of experimentation with the material in question and are independent of the coordinate system. The constitutive law can be expressed using a *strain energy function*, Ψ, which is a scalar value dependant on either $\mathbf{C}$ or $\mathbf{E}$. For example, the Mooney-Rivlin material law is expressed as,

$$\Psi(I_1, I_2, I_3) = c_1(I_1 - 3) + C_2(I_2 - 3) + (I_3 - 1), \tag{3.43}$$

where c_1 and c_2 are experimentally determined parameters. For an incompressible material, which skeletal muscle is assumed to be [118, 85, 99], the third invariant is set to be 1 i.e. $I_3 = 1$, which means that the third term on the right hand side of (3.43) is 0.

Stresses can then be calculated by differentiating the strain energy function with respect to a measure of strain, in this case $\mathbf{E}$.

$$\frac{\partial \Psi}{\partial \mathbf{E}_{MN}} = \frac{\partial \Psi}{\partial I_1}\frac{\partial I_1}{\partial \mathbf{E}_{MN}} + \frac{\partial \Psi}{\partial I_2}\frac{\partial I_2}{\partial \mathbf{E}_{MN}}. \tag{3.44}$$

Equation 3.44 provides the components of the 2^{nd} *Piola-Kirchhoff* stress ten-

sor,

$$T^{MN} = \frac{1}{2}\left(\frac{\partial \Psi}{\partial \mathbf{E}_{MN}} + \frac{\partial \Psi}{\partial \mathbf{E}_{NM}}\right). \tag{3.45}$$

Again M refers to the normal of the surface and N denotes the direction of the force acting on the material in the undeformed state.

As skeletal muscle can be modelled as a transversely isotropic material [12, 85, 118], meaning that at any material point there is one material direction with different stiffness properties to the other two directions, an appropriate constitutive law must be used. In recent work [85] this is achieved by using an isotropic stress tensor, to which additional stress components are added in the fibre direction, to describe the transversely isotropic material behaviour of skeletal muscle.

It should be noted that, when using this method, the isotropic material law is intended to represent the basic structural material components of muscle tissue, that is, the connective tissue (primarily collagen) and passive structural components of the fibres (titin etc.). The additional components that are added to the stress tensor arise from purely active considerations of muscle activity. However, the assumption that the basic passive structural components can be represented by an isotropic material law is fundamentally flawed, as it is well known that passive muscle is transversely isotropic. The use of the isotropic law is an unfortunate necessity, as more accurate skeletal muscle passive (and active) constitutive laws do not currently exist. In this work, the active component that is added to the stress tensor in the fibre direction is composed of two components, T_{passive} and T_{active}. Here T_{passive} is added to try and counteract the inherent problem of using the isotropic material law. T_{passive} should not be thought of as an inherent passive material structural property, but as an active addition to the passive material stiffness to increase the accuracy of the model.

As can be seen in (3.28), the 2^{nd} *Piola-Kirchhoff* stress tensor is dependant on the Cauchy stress tensor which is in turn defined through the constitutive behaviour of the material. The additional stress in the fibre direction is of Cauchy type and can be transformed by (3.28) into a 2^{nd} *Piola-Kirchhoff* tensor, which in turn will be fully populated. Henceforth, the fully populated 2^{nd} *Piola-Kirchhoff* stress tensor will be considered.

A Novel Muscle Constitutive Law

In the work presented in this thesis, the muscle fibre cellular solution was linked to the finite elasticity solution via a new skeletal muscle fibre constitutive law. This new formulation is based on a simple isometric Mooney-Rivlin constitutive law (a generalisation of the neo-Hookean law), with stiffness components added to the fibre direction, turning it into a more accurate transversely isotropic law. The components added to the fibre direction represent the passive and active stiffness of skeletal muscle at different muscle lengths and also depend on the level of muscle activity, which is specified by cellular output parameters. The new relationship is formulated as follows.

The passive stiffness of skeletal muscle in the fibre direction is known to be a result of the stiffness of various structural proteins such as collagen and titin [111]. Within the normal range of motion, most of these structural fibres are not fully extended and therefore non load bearing in much the same way that a crumpled piece of string cannot resist a tensile load without being straightened out. The passive tension is represented mathematically by a piecewise function composed of an exponential function that represents the rapid, non-linear change in passive force as the muscle extends through the upper limit of its normal working range, and a linear function which models the steep increase in force above this point (refer to (3.48) and Figure 3.4). The passive force is included in the constitutive law by being added to the Cauchy stress in the fibres direction. There is zero passive force specified when the muscle is in compression. The resistance to compressive force is attributed to the internal hydrostatic pressure of the muscle. Using (3.28), the 2^{nd} *Piola-Kirchhoff* tensor can be modified as follows

$$T_{\text{passive}} = T_{\text{iso}} + J\mathbf{F}^{-1}\left(\begin{bmatrix} \sigma^{ff}_{\text{passive}} f^{\text{fibre}}_{\text{passive}}(\lambda) & 0_{1\times 2} \\ 0_{1\times 2} & 0_{2\times 2} \end{bmatrix}\right)\left(\mathbf{F}^{T}\right)^{-1} \tag{3.46}$$

where $\sigma^{ff}_{\text{passive}}$ is a constant Cauchy stress, with respect to the material coordinate system, representing the maximal passive stress in the fibre direction, and is the only non zero value of the Cauchy stress tensor. The Jacobian, J, is the determinant of the deformation gradient tensor, $\mathbf{F}$.

The active component of force is represented as follows

$$T_{\text{active}} = T_{\text{passive}} + J\mathbf{F}^{-1}\left(\alpha \begin{bmatrix} \sigma^{ff}_{\text{active}} f^{\text{fibre}}_{\text{active}}(\lambda) & 0_{1\times 2} \\ 0_{1\times 2} & 0_{2\times 2} \end{bmatrix}\right)\left(\mathbf{F}^{T}\right)^{-1} \tag{3.47}$$

The maximum passive stress, $\sigma^{ff}_{\text{passive}}$, and maximum active stress, $\sigma^{ff}_{\text{active}}$, are both set to $0.3MPa$ [12]. The functions $f^{\text{fibre}}_{\text{passive}}(\lambda)$ and $f^{\text{fibre}}_{\text{active}}(\lambda)$ are defined as follows,

$$f^{\text{fibre}}_{\text{passive}}(\lambda) = \begin{cases} 0, & \lambda \leq 1, \\ 0.05\left(e^{6.6(\lambda-1)} - 1)\right), & 1 < \lambda \leq \lambda_{ofl}, \\ 4.6244\lambda - 5.8234, & \lambda > \lambda_{ofl}, \end{cases} \tag{3.48}$$

and

$$f^{\text{fibre}}_{\text{active}}(\lambda) = \begin{cases} -\dfrac{25}{4\lambda^2_{ofl}}\lambda^2 + \dfrac{25}{2\lambda_{ofl}}\lambda - 5.25 & 0.6\lambda_{ofl} \leq \lambda \leq 1.4\lambda_{ofl}, \\ 0 & \text{otherwise}, \end{cases} \tag{3.49}$$

where $\lambda_{ofl} = 1.4$ is a factor used to scale the resting fibre length, to the optimum fibre length [12]. Equation (3.49) is a mathematical simplification of the length tension relationship outlined in the introduction (see Figure 2.22). The plots of these graphs are depicted in Figure 3.4.

The addition of extra stiffness values to the fibre direction of isotropic material laws has been used previously by Oomens *et.al.* [85] to model the mechanics of skeletal muscle. The method specified in (3.46) and (3.47) differ from Oomens *et.al.* as the stiffness components added in the fibre direction are dependant on the output a biophysically-based cellular model, currently the Shorten *et.al.* model. The cellular model is included using the following assumptions. Firstly, the passive stress is assumed to be dependant on the total number of crossbridges that are attached and this is then normalised by the total concentration of crossbridges states ($140\mu M$) which is derived from the Shorten *et.al.* model. As A_1 and A_2 are calculated at optimal fibre length this normalised value is then scaled by the passive force-length relationship (given the fibre stretch), $f^{\text{fibre}}_{\text{passive}}(\lambda)$ and finally multiplied by the maximum possible

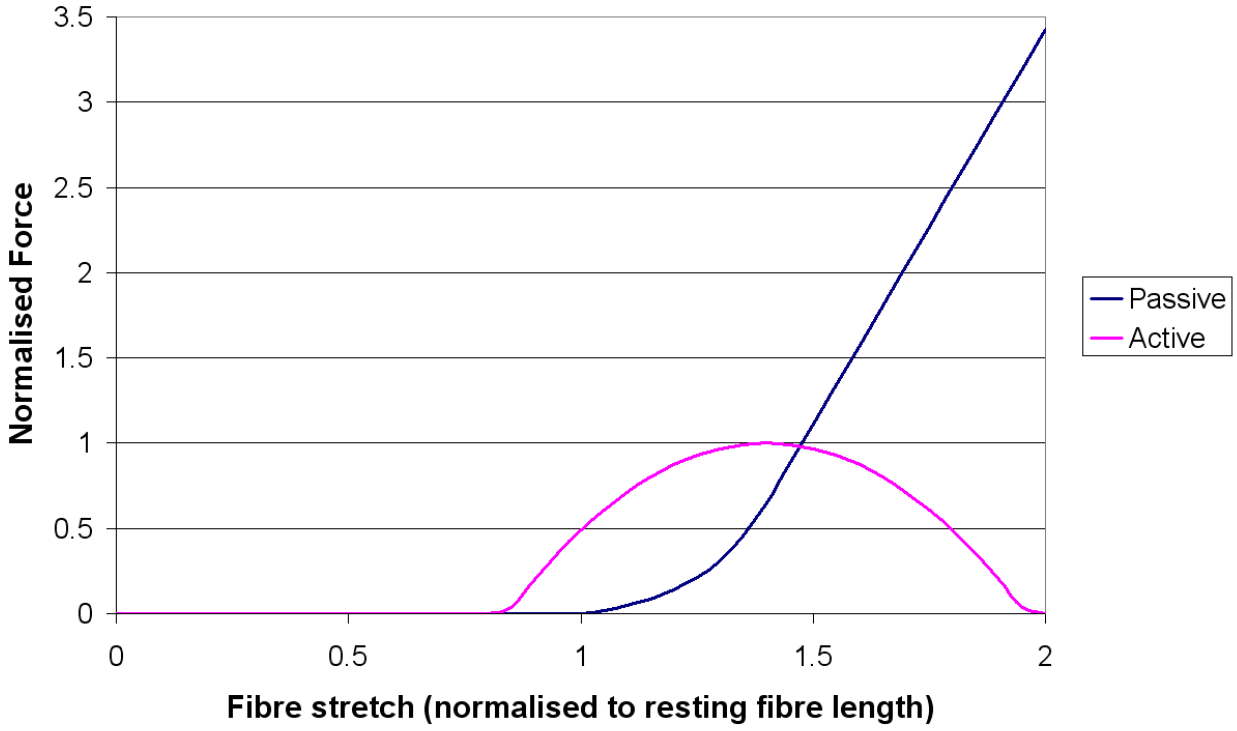

Fig. 3.4: The active and passive normalised force plots based on the normalised resting muscle fibre length

passive force of the muscle $\sigma^{ff}_{\text{passive}}$. This relationship is given by

$$\frac{A_1 + A_2}{140}\sigma^{ff}_{\text{passive}} f^{\text{fibre}}_{\text{passive}}(\lambda). \tag{3.50}$$

The active tension is assumed to be totally dependant on the value of A_2, as these are the crossbridges that have gone through the powerstroke to generate force. The A_2 value is normalised by the maximum possible value of A_2 and then, similarly to the passive relationship, is scaled by the active force-length relationship (given the fibre stretch), $f^{\text{fibre}}_{\text{active}}(\lambda)$, and the maximum active force $\sigma^{ff}_{\text{active}}$ giving,

$$\frac{A_2}{A_2^{max}}\sigma^{ff}_{\text{active}} f^{\text{fibre}}_{\text{active}}(\lambda). \tag{3.51}$$

Finally, combining (3.46), (3.47), (3.50), and (3.51), a relationship that can be used to link the output of the cellular model to the equations of finite elasticity is given by,

$$T^{\alpha\beta} = T^{\alpha\beta}_{\text{iso}} + JF^{-1}\left(\frac{A_1 + A_2}{140}\sigma^{ff}_{\text{passive}} f^{\text{fibre}}_{\text{passive}}(\lambda) + \frac{A_2}{A_2^{\max}}\sigma^{ff}_{\text{active}} f^{\text{fibre}}_{\text{active}}(\lambda)\right)\left(F^T\right)^{-1}. \tag{3.52}$$

The A_1 and A_2 values at each gauss point of the Finite Element mesh are calculated by taking a volume average of the A_1 and A_2 values of the surrounding area. These volume averaged values are the parameter values used in (3.52).

Boundary Conditions

The external surface pressures applied to the boundary ($\int_{S_2} \mathbf{s}\cdot\delta\mathbf{u}\, dS$) can be represented using a physically applied pressure, p_{appl}, applied at a surface with normal vector, $\hat{\mathbf{n}} = \hat{n}_j\mathbf{i}_j$, as follows,

$$\int_{S_2} \mathbf{s}\cdot\delta\mathbf{u}\, dS = \int_{S_2} p_{appl}\hat{n}_j\delta u_j\, dS. \tag{3.53}$$

Substituting back into (3.41) gives,

$$\int_V T^{MN}\frac{1}{J}\frac{\partial x_j}{\partial X_M}\frac{\partial \delta u_j}{\partial X_N}\, dV = \int_V \rho b^j \delta u_j\, dV + \int_{S_2} p_{appl}\hat{n}_j\delta u_j\, dS, \tag{3.54}$$

which is the finite deformation elasticity equation with respect to Cartesian coordinates.

Modelling skeletal muscle using the above equations of finite elasticity and the constitutive law requires that at rest there is an intrinsic force within the muscle. This resting force can be considered a preload applied by the tendons. As the A_1 and A_2 values are modulated by the cellular model, the intrinsic stiffness of the muscle is changed, and this change in stiffness results in a change of the intra-muscular force, measured as a change in the boundary force. The boundary force is measured to be the total unbalanced reaction force at the specified boundary of the muscle. The simulations described in Chapter 5 measure this boundary force as the total force acting on the spatially fixed nodes at the distal end of the muscle. The fixed nodes represent the anatomical location where the muscle would be connected to the distal tendon.

3.2 Numerical Solution of Governing Equations

In this section the numerical solutions of the cellular transmembrane model, the Bidomain equations, and the equations of Finite Elasticity are described. A brief description of the Finite Element Method is presented, including the description of linear and quadratic basis functions. The Finite Element Method is used to solve the Bidomain equations and the equations of Finite Elasticity.

3.2.1 Numerical Solution of the Transmembrane Model

The cellular equations of the Shorten *et.al.* transmembrane model are implemented using the CellML[1] mark-up language. This mark-up language is specifically designed to represent cellular models, cellular processes, and other biological equations and is built on the XML specification. This language has the advantage of representing the equations in a format that can be automatically converted between formats that are used to solve the equations computationally, and view the equations in standard notation. Automatic conversion for publishing, eliminates any typographical errors which can occur with other methods. Current software used for editing and solving CellML

[1] www.cellml.org

models include JSIM[2], COR[3], PCEnv[4] and CMISS[5].

The Shorten *et.al.* system of ordinary differential equations can be solved using a variety of methods. There exist numerous algorithms to solve this system of ODEs. In general one can separate the algorithms into implicit and explicit schemes. An explicit integration scheme is one where the state of the next time instant is calculated as a function of the state at the previous time [107]. An example of the derivation of an explicit Euler scheme is presented from first principles.

From any point on a curve, an approximation to a nearby point on the curve can be found by moving along the tangent. From first principles, the tangent to the curve can be found,

$$\lim_{h\to 0} \frac{dy}{dt} = \frac{y(t+h) - y(t)}{h}, \tag{3.55}$$

where $y(t)$ is a function in time and h is the time step. Rearranging (3.55) gives,

$$y(t+h) \approx y(t) + h \cdot \frac{dy}{dt}. \tag{3.56}$$

Evaluating $\frac{dy}{dt}$ at time point t then gives the approximation,

$$y_{n+1} = y_n + h * f(t_n, y_n), \tag{3.57}$$

where y_{n+1} is the state at the time step t_{n+1}, y_n is the state at t_n, and $f(t_n, y_n)$ is the derivative of $y(t)$ evaluated at t_n. This integration scheme is called the Euler method (or forward Euler method) and is explicit as y_{n+1} is calculated from the previous time step values. If, instead of (3.55), the following approximation was used,

$$\lim_{h\to 0} \frac{dy}{dt} = \frac{y(t) - y(t-h)}{h}, \tag{3.58}$$

then by following a similar process to the derivation of the explicit Euler

[2]http://nsr.bioeng.washington.edu/jsim/
[3]http://cor.physiol.ox.ac.uk/
[4]www.cellml.org
[5]www.cmiss.org

scheme,

$$y_{n+1} = y_n + h * f(t_{n+1}, y_{n+1}). \tag{3.59}$$

Equation 3.59 is the backwards Euler method, an implicit integration scheme as it depends on the value of $y(t_{n+1})$. As can be seen, (3.59) is an equation in the unknown y_{n+1} and therefore can not be solved as simply as the forward Euler scheme.

A root finding algorithm such as the Newton-Raphson method can be employed to find the solution for y_{n+1}. The derivation of the Newton-Raphson method is as follows. Consider a function e.g. $f(x)$. An initial guess as to the root ($f(x) = 0$) is taken, x_n, then the function is approximated by its tangent, and the intercept of the tangent with the x axis is assumed to be a better approximation of the actual root of $f(x)$. The tangent of a function is given by,

$$f'(x_n) = \frac{f(x_n) - 0}{x_n - x_{n+1}}. \tag{3.60}$$

Rearranging gives an update to the root,

$$x_{n+1} = x_n - \frac{f(x_n)}{f'(x_n)}, \tag{3.61}$$

which can then be iterated until desired convergence criteria are met. The process of root finding using the Newton-Raphson method is shown graphically in Figure 3.5.

The fact that a root finding method such as the Newton-Raphson method is required to find subsequent values in an implicit scheme increases the numerical complexity of the solution process. However, implicit schemes have the advantage that they are stable over a larger range of step sizes (h values) than explicit integration schemes. Even with the increased computational effort, implicit schemes can be less computationally expensive than explicit schemes [107]. A further type of integrator is the predictor-corrector method. These methods use an explicit step to predict the approximate value at t_{n+1}, and then use an implicit step (the corrector step) which improves the accuracy of the solution.

One of the major requirements in selecting an integrator to solve cellular models is its ability to handle *stiff* systems of equations. The stiffness is

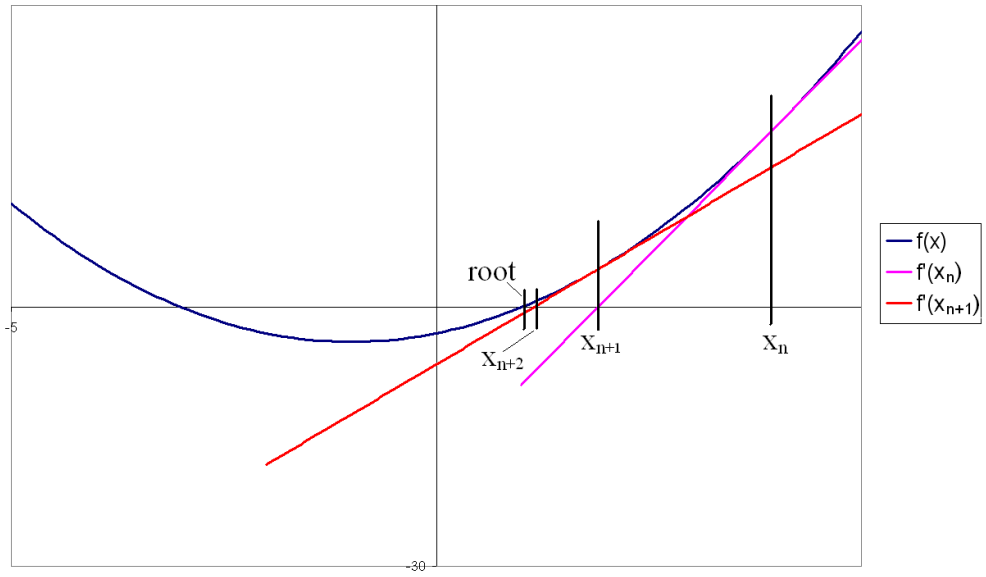

Fig. 3.5: The function of interest is shown in blue ($f(x)$). The initial guess at the root is selected (x_n) and the tangent to the curve is found ($f(x_n)$ in pink). The intercept of $f'(x_n)$ with the x axis is then assumed to be the new estimate of the root of $f(x)$ (x_{n+1} light blue). The tangent at the x_{n+1} is then constructed $f'(x_{n+1})$, and the intercept of this curve is taken to be the new estimate of the root of $f(x)$. This process is continued until convergence criteria are met.

a measure of how difficult it is to solve a system of equations numerically and is characterised by a large difference in time scales between equations. Stiffer systems of cellular equations are becoming more and more common as modellers include more and more multi-scale information into the equations representing the underlying properties of cells [96]. For example, a system that has a variable modelled in the order of μs and another in ms will require time steps 1000 times smaller than is necessary for the ms order variable. The unnecessary solutions of the variable in ms will lead to an accumulation of round off errors and possible numerical instability. As a result, specialised solvers have been developed to handle such problems. The solver used in this work is the LSODA integrator package [57, 92]. This package automatically detects the stiffness of the system and switches between the Adams-Moulton method (an explicit integrator) for non-stiff systems and Gear methods [38] (a predictor-corrector method) for stiff systems.

3.2.2 The Finite Element Method

The Finite Element Method (FEM) is used to numerically approximate solutions to equations which do not necessarily have an analytic solution. The domain over which the equations are to be solved is divided into discrete elements, and approximations to the equations are solved over these elements. The FE method used in this thesis involves creating non-overlapping elements which are defined by a node point mesh. An example of a finite element representation of the geometry of the human femur can be seen in Figure 3.6. This is termed a Finite Element mesh.

Each element can be mapped from rectangular Cartesian coordinates (x, y, z), into a normalised orthogonal system (ξ_1, ξ_2, ξ_3). Each ξ-direction in each element is normalised to be of unit length [0, 1]. Values such as geometric coordinates and, as will be used later, membrane potential or material deformation can be interpolated over an element using the nodal values and interpolation functions, termed basis functions. Linear, and quadratic basis functions will be described in the following section.

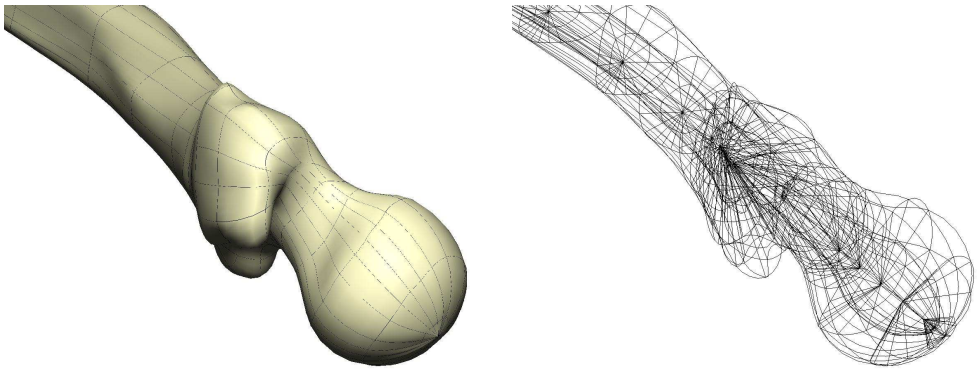

(a) (b)

Fig. 3.6: Subfigure (a) shows the surface of a finite element mesh of the human femur, b) shows the element boundaries. Nodes are located at each of the vertices

Linear Basis Functions

As the name suggests, linear basis functions provide a linear interpolation between nodal values in an element. In one dimension, they can be written as,

$$\phi_1(\xi) = 1 - \xi, \tag{3.62}$$

$$\phi_2(\xi) = \xi, \tag{3.63}$$

where the subscript refers to the local node number. These basis functions can also be thought of as weighting functions as they sum to 1 at every point along the element and each prescribes a unit weight at one node while being zero at the other as shown in Figure 3.7.

Thus values can be approximated over this element by multiplying the nodal field values with the basis functions giving,

$$u(\xi) = (1 - \xi) u_1 + \xi u_2 = \phi(\xi) u_n, \tag{3.64}$$

where u_n is a nodal based quantity at local node number n. The basis functions can also be extended into higher dimensions by taking the tensor product of the one-dimensional functions. For a two-dimensional bi-linear

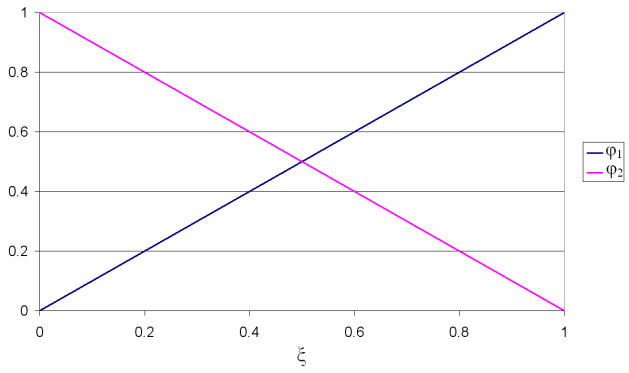

Fig. 3.7: The two independent linear basis functions for one element in one dimension

approximation, let,

$$u(\xi_1, \xi_2) = \phi_1(\xi_1, \xi_2)\, u_1 + \phi_2(\xi_1, \xi_2)\, u_2 + \phi_3(\xi_1, \xi_2)\, u_3 + \phi_4(\xi_1, \xi_2)\, u_4, \quad (3.65)$$

where,

$$\phi_1(\xi_1, \xi_2) = (1 - \xi_1)(1 - \xi_2) \quad (3.66)$$

$$\phi_2(\xi_1, \xi_2) = \xi_1(1 - \xi_2) \quad (3.67)$$

$$\phi_3(\xi_1, \xi_2) = (1 - \xi_1)\xi_2 \quad (3.68)$$

$$\phi_4(\xi_1, \xi_2) = \xi_1\xi_2 \quad (3.69)$$

A three-dimensional scheme could then be created by taking the tensor product of the two-dimensional scheme and the one-dimensional scheme.

Higher-order basis functions can be generated in a similar way to linear functions and used to approximate fields. For example a quadratic scheme can be devised,

$$u(\xi) = \phi_1(\xi)\, u_1 + \phi_2(\xi)\, u_2 + \phi_3(\xi)\, u_3, \quad (3.70)$$

where,

$$\phi_1(\xi) = 2(\xi - 1)(\xi - 0.5), \quad (3.71)$$

$$\phi_2(\xi) = 4\xi(1 - \xi), \quad (3.72)$$

$$\phi_3(\xi) = 2\xi(\xi - 0.5). \quad (3.73)$$

As can be seen the quadratic scheme has three nodes in the ξ direction

as opposed to two in the linear approximation. The quadratic interpolation scheme can be extended into higher dimensions using the same methodology as shown in the linear elements. Thus the three-dimensional scheme is,

$$u(\xi_1, \xi_2, \xi_3) = \sum_{n=1}^{27} \Phi_n(\xi_1, \xi_2, \xi_3) u_n, \tag{3.74}$$

and thus,

$$
\begin{aligned}
\Phi_1(\xi_1,\xi_2,\xi_3) &= \phi_1(\xi_1)\phi_1(\xi_2)\phi_1(\xi_3)\\
\Phi_2(\xi_1,\xi_2,\xi_3) &= \phi_2(\xi_1)\phi_1(\xi_2)\phi_1(\xi_3)\\
\Phi_3(\xi_1,\xi_2,\xi_3) &= \phi_3(\xi_1)\phi_1(\xi_2)\phi_1(\xi_3)\\
\Phi_4(\xi_1,\xi_2,\xi_3) &= \phi_1(\xi_1)\phi_2(\xi_2)\phi_1(\xi_3)\\
\Phi_5(\xi_1,\xi_2,\xi_3) &= \phi_2(\xi_1)\phi_2(\xi_2)\phi_1(\xi_3)\\
\Phi_6(\xi_1,\xi_2,\xi_3) &= \phi_3(\xi_1)\phi_2(\xi_2)\phi_1(\xi_3)\\
\Phi_7(\xi_1,\xi_2,\xi_3) &= \phi_1(\xi_1)\phi_3(\xi_2)\phi_1(\xi_3)\\
\Phi_8(\xi_1,\xi_2,\xi_3) &= \phi_2(\xi_1)\phi_3(\xi_2)\phi_1(\xi_3)\\
\Phi_9(\xi_1,\xi_2,\xi_3) &= \phi_3(\xi_1)\phi_3(\xi_2)\phi_1(\xi_3)\\
\Phi_{10}(\xi_1,\xi_2,\xi_3) &= \phi_1(\xi_1)\phi_1(\xi_2)\phi_2(\xi_3)\\
\Phi_{11}(\xi_1,\xi_2,\xi_3) &= \phi_2(\xi_1)\phi_1(\xi_2)\phi_2(\xi_3)\\
\Phi_{12}(\xi_1,\xi_2,\xi_3) &= \phi_3(\xi_1)\phi_1(\xi_2)\phi_2(\xi_3)\\
\Phi_{13}(\xi_1,\xi_2,\xi_3) &= \phi_1(\xi_1)\phi_2(\xi_2)\phi_2(\xi_3)\\
\Phi_{14}(\xi_1,\xi_2,\xi_3) &= \phi_2(\xi_1)\phi_2(\xi_2)\phi_2(\xi_3)\\
\Phi_{15}(\xi_1,\xi_2,\xi_3) &= \phi_3(\xi_1)\phi_2(\xi_2)\phi_2(\xi_3)\\
\Phi_{16}(\xi_1,\xi_2,\xi_3) &= \phi_1(\xi_1)\phi_3(\xi_2)\phi_2(\xi_3)\\
\Phi_{17}(\xi_1,\xi_2,\xi_3) &= \phi_2(\xi_1)\phi_3(\xi_2)\phi_2(\xi_3)\\
\Phi_{18}(\xi_1,\xi_2,\xi_3) &= \phi_3(\xi_1)\phi_3(\xi_2)\phi_2(\xi_3)\\
\Phi_{19}(\xi_1,\xi_2,\xi_3) &= \phi_1(\xi_1)\phi_1(\xi_2)\phi_3(\xi_3)\\
\Phi_{20}(\xi_1,\xi_2,\xi_3) &= \phi_2(\xi_1)\phi_1(\xi_2)\phi_3(\xi_3)\\
\Phi_{21}(\xi_1,\xi_2,\xi_3) &= \phi_3(\xi_1)\phi_1(\xi_2)\phi_3(\xi_3)\\
\Phi_{22}(\xi_1,\xi_2,\xi_3) &= \phi_1(\xi_1)\phi_2(\xi_2)\phi_3(\xi_3)\\
\Phi_{23}(\xi_1,\xi_2,\xi_3) &= \phi_2(\xi_1)\phi_2(\xi_2)\phi_3(\xi_3)\\
\Phi_{24}(\xi_1,\xi_2,\xi_3) &= \phi_3(\xi_1)\phi_2(\xi_2)\phi_3(\xi_3)\\
\Phi_{25}(\xi_1,\xi_2,\xi_3) &= \phi_1(\xi_1)\phi_3(\xi_2)\phi_3(\xi_3)\\
\Phi_{26}(\xi_1,\xi_2,\xi_3) &= \phi_2(\xi_1)\phi_3(\xi_2)\phi_3(\xi_3)\\
\Phi_{27}(\xi_1,\xi_2,\xi_3) &= \phi_3(\xi_1)\phi_3(\xi_2)\phi_3(\xi_3)
\end{aligned}
$$

The Finite Element discretisation and interpolation described above can be used to solve systems of equations numerically. Instead of describing a known field, such as geometry, approximations to equations describing a field over the region can be represented.

3.2.3 The Finite Element Method Applied to the Bidomain Equations

The Bidomain equations are used, along with the Shorten *et.al.* transmembrane model, to mathematically represent the physiology of a skeletal muscle fibre. The modelled muscle fibre is represented using one-dimensional, linear finite elements, over which the Bidomain equations and the Shorten *et.al.* model are solved. The one-dimensional fibre model must be able to replicate the intrinsic physiological properties of a muscle fibre as outlined in Chapter 2. Such properties include depolarisation and Action Potential formation in response to an applied intracellular current (activation), Action Potential propagation from the point of activation, replication of the Action Potential wave form, and a physiologically realistic Action Potential velocity.

Parameters and Formulation

The Bidomain equations are a set of coupled reaction diffusion equations (refer to Section 3.1.2). In order to solve the coupled partial differential equations, 3.19 and 3.20, the Finite Element Method was used. We assume that the transmembrane voltage, V_m, and the extracellular potential, ϕ_e can be approximated by solutions, $\tilde{V}$ and $\tilde{\phi}$, respectively. Thus the two Bidomain equations become

$$\nabla \cdot \left(\left(\sigma_e + \sigma_i \right) \nabla \tilde{\phi} \right) + \nabla \cdot \left(\sigma_i \nabla \tilde{V} \right) + i_{app} = R_2, \tag{3.75}$$

and,

$$A_m C_m \frac{\partial \tilde{V}}{\partial t} - \nabla \left(\sigma_i \nabla \tilde{V} \right) - \nabla \left(\sigma_i \nabla \tilde{\phi} \right) - A_m I_{ion} = R_1, \tag{3.76}$$

where R_1 and R_2 are the residuals as a result of the transmembrane potential and extracellular potential approximations and i_{app} is any externally applied current. We want to minimise R_1 and R_2, and can achieve this minimisation in a weighted sense by taking the volume integral of them, over the tissue volume

(Ω), and setting the integral to zero, i.e.

$$\int_{\Omega} R_1 W \, d\Omega = 0, \tag{3.77}$$

and,

$$\int_{\Omega} R_2 W \, d\Omega = 0, \tag{3.78}$$

where W are weighting functions used to interpolate $\tilde{V}$ and $\tilde{\phi}$. Substituting (3.77) and (3.78) into (3.75) and (3.76) gives,

$$\int_{\Omega} \nabla \cdot \left((\sigma_e + \sigma_i) \nabla \tilde{\phi} \right) W \, d\Omega = - \int_{\Omega} \nabla \cdot \left(\sigma_i \nabla \tilde{V} \right) W \, d\Omega - \int_{\Omega} i_{app} W \, d\Omega, \tag{3.79}$$

and,

$$\begin{aligned} \int_{\Omega} A_m C_m \frac{\partial \tilde{V}}{\partial t} W \, d\Omega - \int_{\Omega} \nabla \cdot \left(\sigma_i \nabla \tilde{V} \right) W \, d\Omega = \\ \int_{\Omega} \nabla \cdot \left(\sigma_i \nabla \tilde{\phi} \right) W \, d\Omega - \int_{\Omega} A_m I_{ion} W \, d\Omega. \end{aligned} \tag{3.80}$$

Using Green's theorem, (3.79) and (3.80) can be re-written as,

$$\int_{\Omega} \left((\sigma_e + \sigma_i) \nabla \tilde{\phi} \right) \cdot (\nabla W) \, d\Omega = \int_{\Omega} \left(\sigma_i \nabla \tilde{V} \right) \cdot (\nabla W) \, d\Omega - \int_{\Omega} i_{app} W \, d\Omega, \tag{3.81}$$

and,

$$\begin{aligned} \int_{\Omega} A_m C_m \frac{\partial \tilde{V}}{\partial t} W \, d\Omega + \int_{\Omega} \left(\sigma_i \nabla \tilde{V} \right) \cdot (\nabla W) \, d\Omega = \\ - \int_{\Omega} \left(\sigma_i \nabla \tilde{\phi} \right) \cdot (\nabla W) \, d\Omega - \int_{\Omega} A_m I_{ion} W \, d\Omega. \end{aligned} \tag{3.82}$$

Now, assume $\tilde{V}$ is able to be represented by finite element interpolation functions and nodal transmembrane values,

$$\tilde{V}(\tilde{x}, t) = \varphi_M(\tilde{x}) V_M(t), \tag{3.83}$$

where V_M is the value of the transmembrane potential at node point M, and $\tilde{x}$ is the spatial coordinate, and $\varphi_M(\tilde{x})$ is an element based interpolation function.

Similarly, we can write the extracellular potential as,

$$\tilde{\phi}(\tilde{x},t) = \varphi_M(\tilde{x})\phi_M(t), \tag{3.84}$$

where ϕ_M is the value of the extracellular potential at node point M. If we then select the weighting function W to be the same as the interpolations functions for transmembrane potential and extracellular potential (i.e. $W = \varphi_N$), we get,

$$\begin{aligned}\phi_M \int_\Omega \left(\left(\sigma_e + \sigma_i\right)\nabla\varphi_M\right)\cdot\left(\nabla\varphi_N\right)\,d\Omega = V_M(t)\int_\Omega \left(\sigma_i\nabla\varphi_M\right)\cdot\left(\nabla\varphi_N\right)\,d\Omega \\ - i_{app}\frac{1}{A_m C_m}\int_\Omega A_m C_m \varphi_M\varphi_N\,d\Omega,\end{aligned} \tag{3.85}$$

(the reason for the expansion of the far right term will become apparent in the next step) and,

$$\begin{aligned}\frac{dV_M(t)}{dt}\int_\Omega A_m C_m\varphi_M\varphi_N\,d\Omega + V_M(t)\int_\Omega \left(\sigma_i\nabla\varphi_M\right)\cdot\left(\nabla\varphi_N\right)\,d\Omega = \\ - \phi_M\int_\Omega \left(\sigma_i\nabla\varphi_M\right)\cdot\left(\nabla\varphi_N\right)\,d\Omega - I_{ion}\frac{1}{C_m}\int_\Omega A_m C_m\varphi_M\varphi_N\,d\Omega.\end{aligned} \tag{3.86}$$

If we then let,

$$\bar{M}_{MN} = \int_\Omega A_m C_m\varphi_M\varphi_N\,d\Omega, \tag{3.87}$$

$$\bar{K}_{MN} = \int_\Omega \left(\sigma_i\nabla\varphi_M\right)\cdot\left(\nabla\varphi_N\right)\,d\Omega, \tag{3.88}$$

and,

$$\bar{L}_{MN} = \int_\Omega \left(\left(\sigma_e + \sigma_i\right)\nabla\varphi_M\right)\cdot\left(\nabla\varphi_N\right)\,d\Omega, \tag{3.89}$$

then (3.85) and (3.86) can be written as,

$$\bar{L}_{MN}\phi_M(t) = \bar{K}_{MN}V_M(t) - \frac{1}{A_m C_m}\bar{M}_{MN}i_{app}, \tag{3.90}$$

and,

$$\bar{M}_{MN}\frac{dV_M(t)}{dt} - \bar{K}_{MN}V_M(t) = \bar{K}_{MN}\phi_M(t) - \frac{1}{C_m}\bar{M}_{MN}I_{ion}. \tag{3.91}$$

The variables $V_M(t)$ and $\phi_M(t)$ are both functions of time and to solve for them we need to approximate time into discrete steps. For an arbitrary time interval, $t^n \rightarrow t^{n+1}$ the above equations can be rewritten as,

$$\bar{L}_{MN} \int_{t^n}^{t^{n+1}} \phi_M(t)\, dt = \bar{K}_{MN} \int_{t^n}^{t^{n+1}} V_M(t)\, dt - \frac{1}{A_m C_m} \bar{M}_{MN} \int_{t^n}^{t^{n+1}} i_{app}(t)\, dt, \tag{3.92}$$

and,

$$\begin{aligned} \bar{M}_{MN} \int_{t^n}^{t^{n+1}} \frac{dV_M(t)}{dt}\, dt - \bar{K}_{MN} \int_{t^n}^{t^{n+1}} V_M(t)\, dt = \\ \bar{K}_{MN} \int_{t^n}^{t^{n+1}} \phi_M(t)\, dt - \bar{M}_{MN} \int_{t^n}^{t^{n+1}} \frac{I_{ion}}{C_m}\, dt. \end{aligned} \tag{3.93}$$

We can then assumed that $V_M(t)$ and $\phi_M(t)$ can be approximated by,

$$\phi_M(t) \simeq (1-\theta)\phi_M(t^n) + \theta\phi_M(t^{n+1}) = (1-\theta)\tilde{V}^n + \theta\tilde{V}^{n+1}, \tag{3.94}$$

and,

$$V_M(t) \simeq (1-\theta)V_M(t^n) + \theta V_M(t^{n+1}) = (1-\theta)\tilde{\phi}^n + \theta\tilde{\phi}^{n+1}. \tag{3.95}$$

In the above equations, θ represents an arbitrary weighting between the present and future values of the time dependant variables, and is chosen to be $\theta = 1$ (refer to (3.97) and (3.99)). The solution then proceeds in three separate steps. Firstly, the far right term in (3.93) is evaluated. This term is referred to as the reaction term, as it defines the change in membrane voltage as a result of the transmembrane currents, thus we can substitute,

$$\int_{t^n}^{t^{n+1}} -\left[\frac{I_{ion} - I_{stim}}{C_m}\right] dt = \hat{V}^{n+1}. \tag{3.96}$$

The term $\hat{V}^{n+1}$ will provide the initial guess at the transmembrane voltage. If we compare (3.96) with (3.1) we see that the both equations provide representations of the transmembrane potential. We use the transmembrane potential calculated from the Shorten *et.al.* cellular model as the initial predicted value for the transmembrane voltage, thus linking the Shorten *et.al.* model with the

Bidomain equations.

The second step in the solution process then involves solving for the diffusion of the membrane potential through the medium,

$$\bar{M}_{MN}\left(\frac{\tilde{V}^{n+1}-\tilde{V}^{n}}{\Delta t}\right)-\bar{K}_{MN}\tilde{V}^{n+1}=\bar{K}_{MN}\tilde{\phi}^{n}+\bar{M}_{MN}\hat{V}^{n+1}, \tag{3.97}$$

which can be rearranged to,

$$\left(\bar{M}_{MN}-\Delta t\bar{K}_{MN}\right)\tilde{V}^{n+1}=b, \tag{3.98}$$

or $Ax = b$ which can be solved using LU factorisation. Thus (3.97) gives an updated value of $\tilde{V}^{n+1}$, which is then used in the third step of the solution procedure, solving for the extracellular potential,

$$\bar{L}_{MN}\tilde{\phi}^{n+1}=\bar{K}_{MN}\tilde{V}^{n+1}-\frac{1}{A_m C_m}\bar{M}_{MN}i_{app}(t^{n+1}). \tag{3.99}$$

The values of the surface to volume ratio (A_m), membrane capacitance (C_m) and intra and extracellular conductivity of skeletal muscle were obtained from the literature. As muscle fibres in humans are of a relatively consistent diameter of approximately $80-100\mu m$ [70, 78, 106], the surface to volume ratio was set at $50mm^{-1}$ (assuming a diameter of $80\mu m$). The capacitance of the membrane was set at $0.01\mu F mm^{-2}$ for the fast twitch fibres and $0.0058\mu F mm^{-2}$ for the slow twitch fibres [105]. As one dimensional fibre models were being solved, the only conductivities that were required were the intracellular and extracellular conductivities in the fibre direction (σ_e^f and σ_i^f). This is because there is no mathematical link between the electrophysiology of adjacent fibres in the framework, and as such conductivities in any direction other than the fibre direction are not required. The intracellular conductivity was set at $0.893mSmm^{-1}$ [16] and the extracellular conductivity was set at $0.67mSmm^{-1}$ [102, 104].

3.2.4 The Finite Element Method for Finite Elasticity

The Finite Element Method is used to numerically solve the equations of Finite Elasticity. The numerical solution will then be used to calculate the deforma-

tion of the whole muscle as a result of the physiological data conveyed through the constitutive law (refer to Section 3.1.3). Transforming (3.54) in normalised, orthogonal ξ space, we get,

$$\int_0^1\int_0^1\int_0^1 T^{MN}F_M^j\frac{\partial\delta u_j}{\partial X_N}\sqrt{\mathbf{G}(\xi)}\,d\xi_3\,d\xi_2\,d\xi_1 = \int_0^1\int_0^1\int_0^1 \rho_o b^j\delta u_j\sqrt{\mathbf{G}(\xi)}\,d\xi_3\,d\xi_2\,d\xi_1 + \int_0^1\int_0^1 s^j\delta u_j\sqrt{\mathbf{g}(\xi)}\,d\xi_2\,d\xi_1, \tag{3.100}$$

where $\mathbf{G}$ and $\mathbf{g}$ are Jacobian matrices which are used to map between the real space and ξ space.

$$G_{MN}(\xi) = \frac{\partial\mathbf{X}(\xi)}{\partial\xi_M}\cdot\frac{\partial\mathbf{X}(\xi)}{\partial\xi_N}, \qquad M,N = 1,\ldots,3, \tag{3.101}$$

$$g_{ij}(\xi) = \frac{\partial\mathbf{x}(\xi)}{\partial\xi_i}\cdot\frac{\partial\mathbf{x}(\xi)}{\partial\xi_j}, \qquad i,j = 1,\ldots,3. \tag{3.102}$$

The virtual displacements δu_j can be interpolated using the same basis functions that are used to represent the geometric mesh (see Chapter 4), giving,

$$\delta u_j = \sum_n \phi_n(\xi)\delta u_j^n, \tag{3.103}$$

where the subscript n represents the node number. Equation (3.103) can then be substituted into (3.100) which can be rearranged to give,

$$\int_0^1\int_0^1\int_0^1 \rho_o b^j\phi_n\delta u_j^n\sqrt{\mathbf{G}(\xi)}\,d\xi_3\,d\xi_2\,d\xi_1 + \int_0^1\int_0^1 s^j\phi_n\delta u_j^n\sqrt{\mathbf{g}(\xi)}\,d\xi_2\,d\xi_1 - \int_0^1\int_0^1\int_0^1 T^{MN}F_M^j\frac{\partial\phi_n\delta u_j^n}{\partial X_N}\sqrt{\mathbf{G}(\xi)}\,d\xi_3\,d\xi_2\,d\xi_1 = 0. \tag{3.104}$$

The stresses calculated in (3.104) are calculated with respect to the fibre directions which are defined along with the geometry of the triquadratic mesh (refer Section 4). The fibre directions are also explicitly related to the constitutive law, as mentioned in Section 3.1.3.

Equation (3.104) can be represented in the form of Residuals, and is thus

reduced to,

$$R_j^n \delta u_j^n = 0, \qquad \begin{array}{l} n = 1, \ldots, number \;\; of \;\; nodes, \\ j = 1, \ldots, 3, \end{array} \tag{3.105}$$

In (3.105) the virtual displacements δu_j are taken out as a common factor from (3.104). Equation (3.105) can be represented as a system of equations, $\delta \mathbf{v} \cdot \mathbf{R}(\mathbf{x}) = 0$. As the displacements are by definition arbitrary, the system of equations can be reduced to,

$$\mathbf{R}(\mathbf{x}) = 0, \tag{3.106}$$

where, for an element of degree of freedom x^e, the residual vector is,

$$\mathbf{R^e}(\mathbf{x^e}) = \begin{bmatrix} \mathbf{R_1} \\ \vdots \\ \mathbf{R_i} \\ R^p \end{bmatrix}, \tag{3.107}$$

where R^p is residual which specifies the incompressibility constraint arising from the requirement that the third invariant of the Cauchy-Green tensor, I_3, is equal to 1, which is enforced by,

$$\int_0^1 \int_0^1 \int_0^1 \sqrt{I_3 - 1} \varphi_n^p \sqrt{\mathbf{G}(\xi)} \, d\xi_3 \, d\xi_2 \, d\xi_1 = 0, \tag{3.108}$$

where φ_n^p are the basis functions approximating the internal hydrostatic pressure in the FE mesh. Tri-linear basis functions are used to approximate the hydrostatic pressure.

The residual vector is highly nonlinear. In order to solve this system of equations, a root finding algorithm is used. In this thesis the Newton-Raphson method was used (refer to Section 3.2.1). The initial guess at the value of the root is the undeformed state. Using this, we arrive at,

$$\mathbf{R} + \frac{\partial \mathbf{R}}{\partial \mathbf{x}} \delta = 0, \tag{3.109}$$

where δ are the solution increments between the known solution $\mathbf{x}$ and the unknown solution.

3.2.5 The Grid Based Finite Element Method

The grid based Finite Element Method is a technique that has been integrated into the CMISS computer package (refer to Section 3.3) for the solution of the Bidomain equations. A high resolution computational grid is embedded in a Finite Element geometric model and the Finite Element discretisation of the Bidomain equations is used to integrate the equations over linear Finite Elements defined by the high resolution grid. The use of the grid based Finite Element Method allows a very small spatial resolution (which is required for numerical convergence, as seen in Chapter 4) to be defined between computational points very easily. The grid points used to solve the Bidomain equations (i.e. grid based Finite Element solution points) will hereafter be defined as Bidomain grid points. Bidomain grid points are not to be confused with the grid points that are used to define individual fibres within three-dimensional muscle mesh (refer to Chapter 4). This distinction will be made clear in Chapter 4.

3.3 CMISS

CMISS[6] is an in-house computer program originally developed in the Department of Engineering Science and currently developed at the Bioengineering Institute for **C**ontinuum **M**echanics, **I**mage analysis, **S**ignal processing and **S**ystem identification. Unless stated otherwise, all simulations within this thesis have been run using this software problem. The ODE integrators that were used to solve the transmembrane model, the grid based FEM and Bidomain solvers, and the finite elasticity solvers have all been programmed into the framework by other researchers. To this substantial base of code, routines specific to the solution of skeletal muscle problems have been added as will be detailed in Chapter 4.

[6] www.cmiss.org

Chapter 4

Creation of a Whole Muscle Model

In this chapter the physiology of a single muscle fibre initially represented, followed by an extension of the framework into the representation of a selection, or all, of the fibres within a muscle. The framework will also include anatomical partitioning, fibre angles, motor unit grouping, fibre type distribution, and the geometry of the motor unit territory. For the purposes of this work, the human Tibialis Anterior muscle is used as an example of the framework implementation (the geometric data of the Tibialis Anterior was obtained from the visible human data set [108]).

The Tibialis Anterior muscle is located on the lateral side of the tibia and is thick and fleshy proximally and tendonous distally. It arises from the lateral condyle and upper region of the lateral surface of the tibia and inserts into the medial, lower surface of the first cuneiform bone and the base of the first metatarsal bone [41] (Figure 4.1). It is composed of a superficial and a deep compartment separated by a tendonous aponeurosis, with the fibres of each compartment having a different pennation angle [67]. The Tibialis Anterior muscle was selected to be the muscle subject for the development and testing of these techniques because it is a common target of investigation in the literature and as such, a wealth of information could be gathered on its structure and function.

Within this section, multiple references to 'fibres' and 'grid points' are used. To avoid confusion the following conventions will be used where appropriate.

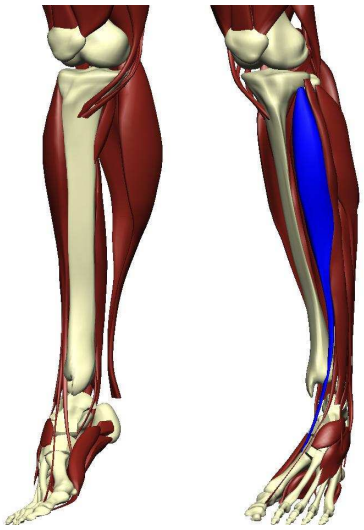

Fig. 4.1: The location of the Tibialis Anterior, shown in blue, in the human lower limb.

When referring to a physiological model of a muscle fibre (see Section 4.1, i.e. where the Bidomain equations are used to replicate the physiology of a muscle fibre using the Shorten *et.al.* model), the term Bidomain fibre will be used. Bidomain grid points will refer to the grid based FEM solution points that make up a Bidomain fibre. Within this chapter the creation of muscle fibres within a three-dimensional muscle geometry is described, and these fibres will be referred to as mechanical fibres. The mechanical fibres are also made up from grid points which shall be referred to as mechanical grid points. It is the mechanical grid points onto which the physiological values calculated from the Bidomain grid points are mapped. Finally, when referring to the actual muscle fibres that compose real muscle tissue, the term physiological muscle fibres will be used.

In Section 4.2 the methods used to reproduce the structure of the Tibialis Anterior are introduced. The structural representation of the Tibialis Anterior includes the large scale characteristics of the muscle, i.e. the geometry and separate muscle compartments, and also the physiological fibre level geometry, i.e. the physiological fibre directions and fibre geometric properties. The functional representation of the Tibialis Anterior is then presented in Section 4.3. The grouping of mechanical fibres into motor units and then the distribution of mechanical fibres within the muscle geometry is described. Finally,

a discussion on the validity of the approaches used is presented.

4.1 Modelling the Electrophysiology of a Skeletal Muscle Fibre

The following section describes the creation and validation of an electrophysiological, and a one-dimensional model of a skeletal muscle fibre. Subsequently in this chapter, a number of these one-dimensional models are used to represent muscle fibres within a three-dimensional muscle geometry. The combination of the one-dimensional physiological model, and the three-dimensional muscle model produces the multi-scale model that is used in the remainder of this thesis. One-dimensional fibres are chosen such that the electrical isolation of skeletal muscle fibres can be replicated. Embedding such one-dimensional models within a three-dimensional geometry allows mechanical coupling while maintaining the electrical insulation.

The first step to creating the fibre model is the solution of the Shorten *et.al.* transmembrane model, which represents skeletal muscle physiology at a single point. The procedure used to do this is outlined in Chapter 3. The numerical implementation of the Bidomain equations, along with the Shorten *et.al.* model, will be used to model a one-dimensional fibre, and validate the parameter set.

4.1.1 Solution of the Shorten *et.al.* Model

The system of ordinary differential equations that comprise the Shorten *et.al.* cell model (see Appendix A) are solved using the LSODA integrator package as outlined in Section 3.2.1. The parameter set that would give an accurate solution to the set of equations was investigated. The input parameters required for LSODA are listed below,

- The time increment.
- The maximum number of iterations that can be taken without reaching a converged solution before sending an error message.

- The type of error control. Error control options were, pure absolute, relative, or Mixed relative/absolute.
- The error tolerance.

Absolute error control uses the general formula,

$$\left|y_{s+1}^{n} - y_{s}^{n}\right| \leq ErrTol, \tag{4.1}$$

where the difference between the solution for state variable n at iteration $s+1$ and the previous solution iteration value is compared with the specified error tolerance $ErrTol$. The solution is deemed to have converged when the difference between all the iterated state values is less than $ErrTol$. Relative error control uses the formula,

$$\left|\frac{y_{s+1}^{n} - y_{s}^{n}}{y_{s+1}^{n}}\right| \leq ErrTol. \tag{4.2}$$

In this case the difference between the successive iteration values is in effect normalised by the current value of the state variable. This form of error control is useful when the values of state variables differ by a number of orders of magnitude, as the error tolerance is always being compared to a normalised value. However, the downside of using relative error control is that, if a state variable is tending towards 0 and starts getting near the floating point error of the machine, then the method can break down. As rounding errors become dominant, the error introduced can effect the implementation of the convergence criteria. Mixed error control, as the name suggests, uses both forms of error control. This form is useful when wanting to employ relative error control, but having some state values that are tending to 0.

For the Shorten *et.al.* model, the time increment and the error tolerance were the variables that were investigated. The maximum number of iterations was set at 999 (the maximum allowable in CMISS), and pure absolute error control was selected. This type of error control was chosen as, even though there was a large difference in the magnitude of some state variables, there were a number of state variables that would tend to get very close to 0, i.e. gaiting variables. As this investigation was to test the convergence of the cell model as a function of time step and error tolerance changes, it was decided

that pure absolute error control would be more appropriate than relative or mixed error control.

The fast type muscle parameterisation of the cellular equations was selected for the time discretisation study as the stiffness of the system of ODEs was, if different to the slow parameterisation, slightly greater due to the faster kinetics of it's ODEs (i.e. rise time of the action potential). The protocol for the numerical experiments was as follows:

1. A $5ms$ simulation of activation of the system of ODE's was run.
2. The membrane potential was outputted at $0.2ms$ intervals.
3. The time discritisation (Time Step) was changed.
4. Steps 1-3 were repeated for the following time discretisations $\Delta t = 0.1ms$, $0.01ms$, $0.001ms$ and $0.0001ms$.
5. The difference between each of the output values with respect to the $0.0001ms$ output value was calculated and squared.
6. For each time discritisation, the square root of the average of the values was calculated (RMS).
7. Steps 1-6 were repeated for the following Absolute Error values 0.1, 0.1^{-4}, and 0.1^{-8}.

Examples of the output from the test protocol can be seen in Figure 4.2. Thus the difference that the input values of Absolute Error and the Time Step had on the Action Potential wave forms could be calculated. The metric used to determine the difference between the Action Potential waveforms resulting from the different input values was the RMS error. The RMS error was calculated by finding the average of the squared difference between the output values, with respect to the output at $\Delta t = 0.001$ (assumed to be the most accurate solution). For example, for the LSODA time step investigation, the difference between the output of each step was compared with the finest step ($0.0001ms$). The results of these simulations can be seen in Table 4.1.

From Table 4.1 it can be seen that there was a negligible increase in accuracy between Absolute Error values of 0.1^{-4} and 0.1^{-8}. Also for Absolute

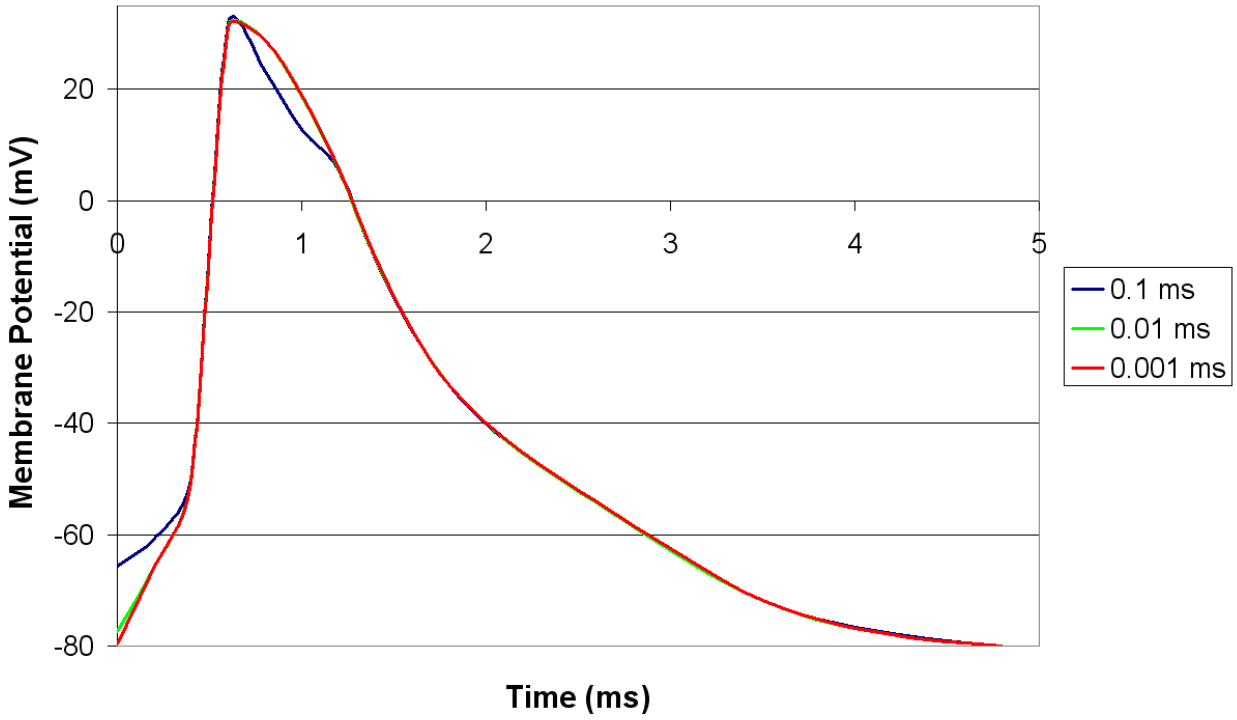

Fig. 4.2: The Action Potential traces for a $5ms$ duration simulation. The membrane potential is plotted at $0.2ms$ intervals. The time step used in the LSODA solver was varied as specified in the legend. As can be seen the trace with a time step on $0.1ms$ displayed much greater variation than the traces of time steps $0.01ms$ and $0.001ms$. The absolute difference between these plots was used to gauge the convergence.

Table 4.1: The RMS error of the Action Potential wave form calculated with respect to the Action Potential of minimum time discretisation. The two parameters that are varying are Absolute Error and the Time Step (both LSODA input parameters).

Time Step (ms)	Absolute Error 0.1	0.1^{-4}	0.1^{-8}
0.1	3.471	3.405	3.405
0.01	0.524	0.526	0.526
0.001	0.062	0.570	0.580

Error values of 0.1^{-4} and 0.1^{-8} we see little change in the RMS error with respect to a decrease in time discritisation from $0.01ms$ to $0.001ms$. From this study it was decided that an Absolute Error value of 0.1^{-4} and a Time Step of $\Delta t = 0.01ms$ were adequate parameter values to use for the LSODA solution of the Shorten *et.al.* transmembrane model.

4.1.2 Fibre Solution Validation

This section demonstrates the use of the Shorten *et.al.* model and the Bidomain equations, solved using the Finite Element Method, to represent the physiology of skeletal muscle fibres. The behaviour of the solution to the change in Bidomain grid point spacing is investigated so that a converged numerical solution is achieved. The metric used to demonstrate convergence of the Bidomain solution on the one-dimensional fibre is the convergence of the Action Potential velocity.

Within the human body, muscle fibres are activated through the inward sodium current at the neuromuscular junction as a result of an Action Potential from a motor neuron. Since no appropriate mathematical description of a neuromuscular junction is available, the activation of a single muscle fibre is simulated by injecting an intracellular current to a single Bidomain grid point. At each desired stimulation time, t_{stim}, an intracellular current is added to the fibre model, via the I_{stim} variable in (3.96). The I_{stim} that is added is spatially varying in that it is only non-zero at the central point of the muscle fibre (the location of the neuromuscular junction). A current of $8000\mu A/mm^3$ is used as this is large enough to cause a depolarisation large enough for the system of ODEs to reach Threshold Potential. Figure 4.3 shows an activated fibre at three different time points. The Action Potential can clearly be seen propagating down the length of the fibre (left to right). As we will see later, the I_{stim} current injection allows the timing of the activation to be controlled to give the desired fibre stimulation frequency.

The grid based Finite Element Method as described in Section 3.2.2 was used to represent the muscle fibre. For these experiments a linear interpolation scheme was used. A single $32mm$ long element was used to represent a muscle fibre.

The metric used to determine the convergence of the Bidomain fibre model

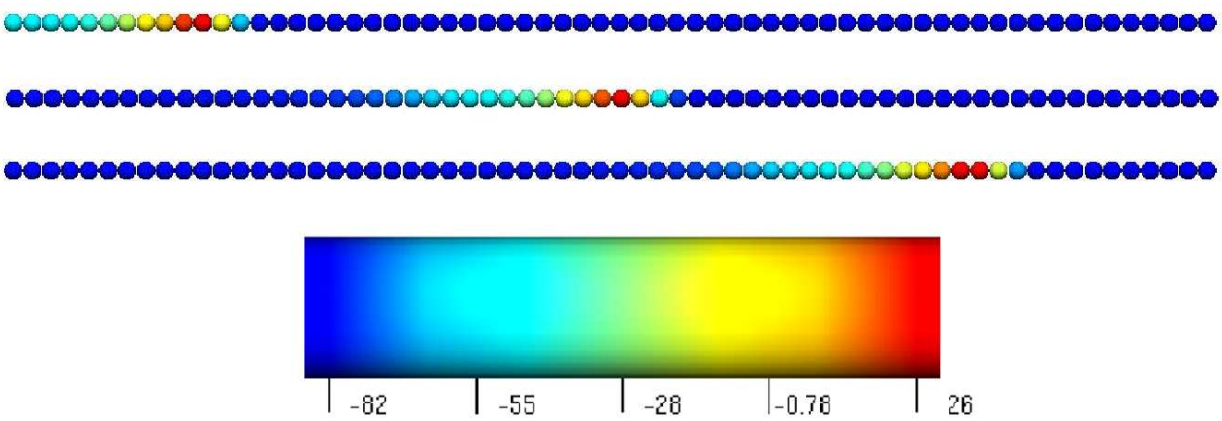

Fig. 4.3: A 32mm finite element representation of muscle fibre membrane potential with a Bidomain grid spacing of 0.5mm at time $3ms$, $8ms$ and $12ms$ after simulation at the left end. The Action Potential can clearly be seen propagating from left to right with a peak amplitude of approximately $35mV$. Note that for this experiment the Action Potential was initiated at the left end of the fibre, where as in real muscle fibres the Action Potential occurs in the middle of the Bidomain fibre (at the neuromuscular junction) and propagates in both directions along the fibre.

was the convergence of the Action Potential velocity (conduction velocity). The conduction velocity was determined by calculating the time of the maximum positive gradient in membrane potential (activation time) at a Bidomain grid point some distance from the site of activation.

$$CV = \frac{GP_{no} \cdot GP_{spacing}}{t^{MaxRise}}, \tag{4.3}$$

where GP_{no} is the Bidomain grid point number were the time of maximum rate of membrane potential rise ($t^{MaxRise}$) was measured, and $GP_{spacing}$ is the spacing between the Bidomain grid points in the finite element mesh. During the convergence experiments GP_{no} was changed for each successive $GP_{spacing}$ so that the total distance between the point of activation, and the sight of maximum membrane potential rise, was the same distance. Simulations were run with progressively smaller Bidomain grid point spacing and the conduction velocities calculated. The results of this study for both fast and slow type muscle fibres can be seen in Figure 4.4. Plots of the Action Potential wave form at a location $25mm$ from the point of stimulation can be seen in Figure 4.5.

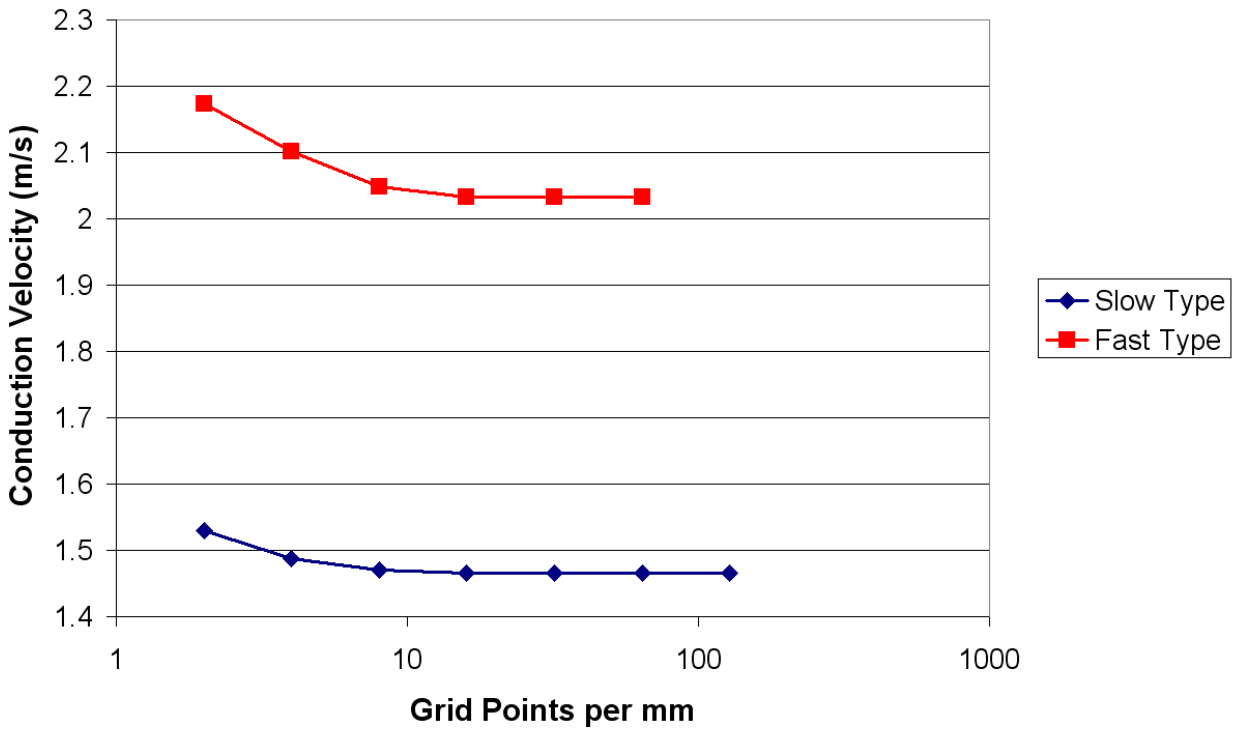

Fig. 4.4: Plot of Action Potential velocity for fast and slow fibre types at different Bidomain grid point spacings. The conduction velocities reduce as the number of Bidomain grid points per millimetre is increased until there is no further change in conduction velocity. The point at which there is no further change in conduction velocity occurs at a Bidomain grid point spacing of $0.0625mm$. Note the difference in conduction velocities between the two muscle types.

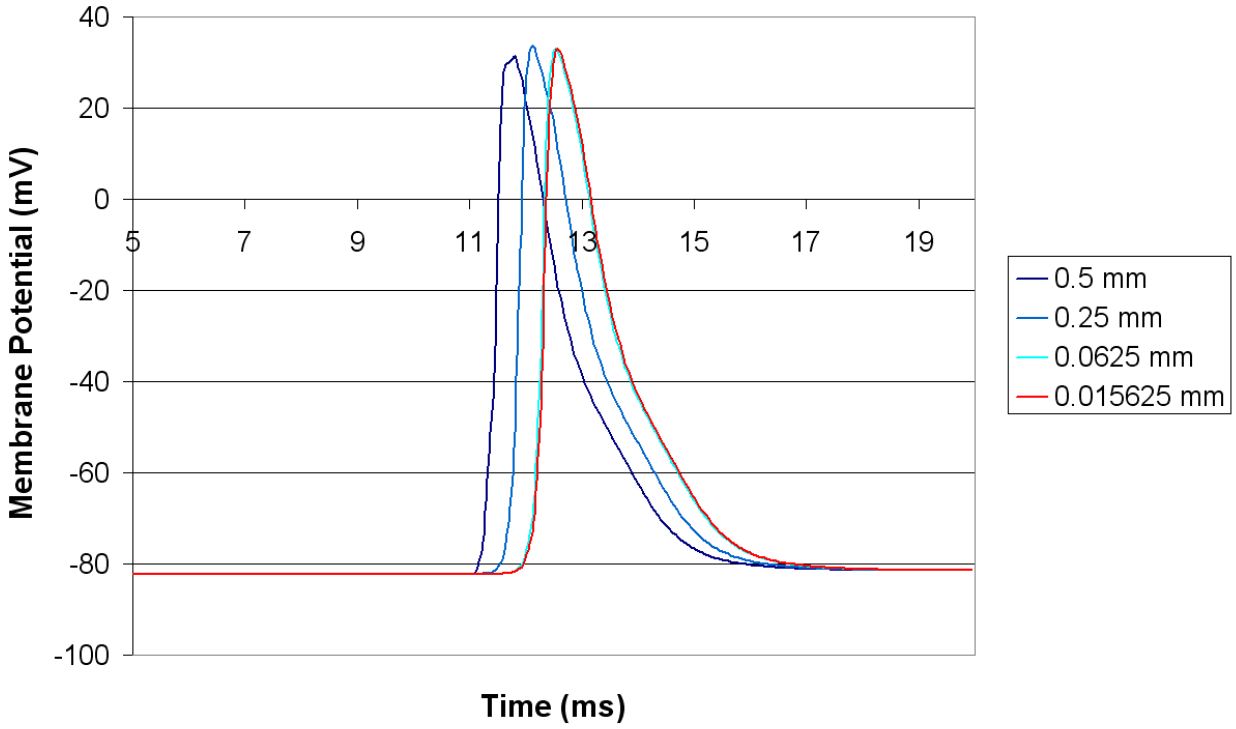

Fig. 4.5: Plot of the Action Potential in the fast fibre at a point $25mm$ from the site of stimulation. Notice as the Bidomain grid point spacing (legend) reduces the Action Potential converges in both form and temporal location.

The converged Action Potential velocities are, for slow type muscle, $1.466m/s$, and for fast type muscle, $2.033m/s$. The action potential peak, duration and velocity are consistent with values from the literature [105].

4.1.3 The Motor Unit Representative Fibre

The one-dimensional Bidomain fibre model described above allows for the simulation of the cellular physiology of individual muscle fibres. The next step of the framework is to be able to represent all, or a section, of the fibres within the three-dimensional geometry of a muscle. As all the fibres within a motor unit receive the same activation from the α-motor neurons, a single one-dimensional Bidomain fibre model is sufficient to represent the physiology of all muscle fibres within a motor unit. Thus we coin the term Motor Unit Representative Fibre (MURF), which is the single Bidomain fibre whose physiological output can be mapped to every mechanical fibre within a motor unit. As a result, for a muscle with 100 motor units, only 100 MURF's are required to be solved. Given that a real muscle made up of 100 motor units could contain hundreds of thousands of individual muscle fibres, this simplification represents a huge saving in computational power.

4.2 Representing the Structure of Skeletal Muscle

4.2.1 Creating Three-Dimensional Muscle Geometry

To produce an anatomically based three-dimensional representation of the Tibialis Anterior muscle, two-dimensional photographic slices of known spacing of the muscle were digitised using CMISS. These images were obtained from the visible human data set [108]. The digitisation produced a three-dimensional data cloud to which an initial mesh consisting of triquadratic lagrange Finite Elements was fitted. The fitting process involved minimising the difference between the surface of the Finite Element volume and the reference points using a least-squares minimisation technique. The mesh that was fitted to the data cloud was a tri-quadratic Finite Element mesh which was generated so that it

could be used to represent the internal structure of the Tibialis Anterior. The method for generating a Finite Element mesh from a cloud of data is presented in detail in Fernandez *et.al.* [34] for tri-cubic Hermite elements. The process is the same for tri-quadratic elements.

The Tibialis Anterior muscle consists of two anatomical compartments divided by an internal tendon. The superficial and deep compartments were digitised and individually fitted with Finite Element meshes. Each of the two meshes was generated and fitted in such a way that the physiological fibre directions described in Lansdown *et.al.* [67] were followed explicitly by one of the primary element directions (ξ_1). The two meshes were then fused at the boundary of the internal tendon which produced the Finite Element mesh, consisting of twelve elements, four representing the superficial compartment and eight representing the deep compartment of the Tibialis Anterior. The Finite Element mesh generated by this procedure can be seen in Figure 4.6.

Tri-quadratic Finite Elements were selected as they were able to provide a more accurate approximation to the geometry than linear basis functions, and the discontinuity in physiological fibre angle at the internal boundary between the two muscle compartments could be represented. The fibre angle discontinuity could not be achieved using tri-cubic Hermite elements without using special meshing techniques that were deemed over complicated for this application.

4.2.2 Generation of Fibres Within the Tibialis Anterior Mesh

Each mechanical fibre within the three-dimensional Tibialis Anterior mesh was to be represented by a string of mechanical grid points. Each string of mechanical fibre grid points was required to conform to a set of constraints so that the anatomical properties of the muscle would be represented accurately, and also, so that the physiological properties, as calculated from the one-dimensional Bidomain fibres models, would be able to be mapped accurately to the embedded mechanical fibre grid points.

1. Each mechanical muscle fibre should have approximately the same cross-sectional area and an approximately uniform diameter, to replicate phys-

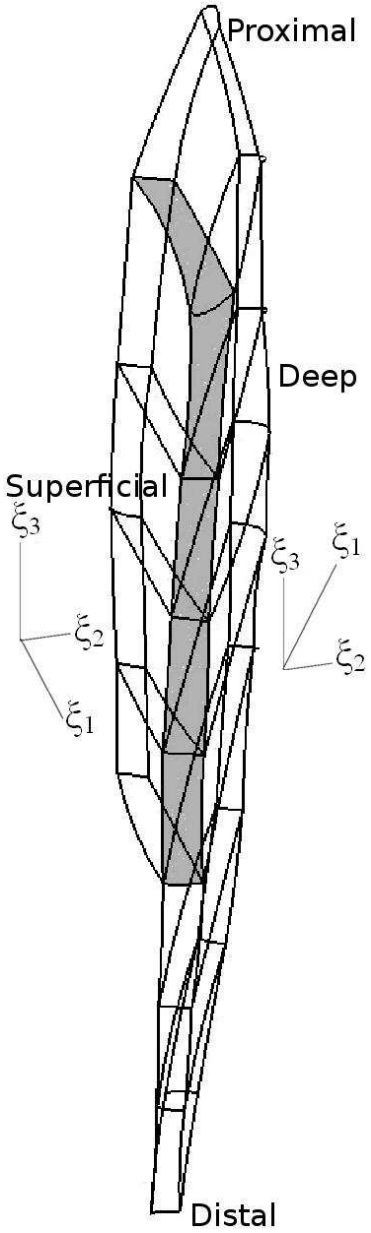

Fig. 4.6: The tri-quadratic mesh of the Tibialis Anterior is shown with the element boundaries represented by wires. The shaded section represents the element boundaries that are aligned with the aponeurosis, separating the superficial and deep compartments of the muscle. Note the skewed angle of the elements as a result of creating the elements so that ξ_1 of every element follows the physiological fibre direction of the real Tibialis Anterior. The approximate directions of the ξ-coordinates of both the superficial and deep muscle compartments can be seen as the two deformed axes. The mechanical fibre direction in both compartments is defined to follow the ξ_1 direction of all of the elements.

iological muscle fibres.

2. Mechanical muscle fibres should follow the physiological fibre direction of the muscle as closely as possible.

3. The spacing of the mechanical grid points representing a fibre must be even in Cartesian coordinates.

An even spacing of mechanical fibres (i.e. similar cross-sectional area and diameter) is necessary as deformations in the mechanical fibre cross-sectional density will cause unwanted deformations in the local stress field. Requirement 3 arises as the mechanical fibres in the muscle mesh are not the solution points for the Bidomain equations, but rather serve as points at which the Bidomain output can be mapped to. As a result the spacing of the mechanical grid points must be even, so that when they are updated with cellular parameters from the uniformly spaced Bidomain fibre simulation (the Bidomain grid points are uniformly spaced), no distortions in the propagation wave occur.

The generation of muscle mechanical fibres within the muscle mesh is highly dependant on the geometry of the elements in the finite element mesh of the three-dimensional muscle geometry. This dependency arises for the following two reasons. Firstly, mechanical fibres are 'grown' through the tri-quadratic Finite Elements (the mechanical fibre growth is described in Section 4.2.2) from predefined 'seed points' (the generation of these seed points is described in Section 4.2.2) and the direction of mechanical fibre growth is constrained to be parallel with one of the ξ directions of the elements. Growth of the mechanical fibres along a ξ axis has the advantage that it is relatively easy to generate mechanical grid points in the intrinsic element direction. In order to generate the mechanical fibres so that they might follow some other arbitrary path, another field describing this path would have to be generated. Another advantage to the mechanical fibres following a ξ direction is that the constitutive law (refer to Section 3.1.3) used requires a description of the material axes so that the 2^{nd} *Piola-Kirchhoff* stress tensor can be updated, and linking the mechanical fibre direction with an intrinsic element direction simplifies the calculations.

Secondly, when defining the mechanical muscle fibres, a physiologically derived starting point and end location are required, so that the properties

of the physiological muscle fibres can be replicated. The start points of each mechanical muscle fibre will hereafter be referred to as the 'seed point' of the fibre, as it is the point from which the mechanical fibre is 'grown' through the mesh. For simplicity, the seed and end points are defined to lie on the boundary of the elements making up the three-dimensional muscle mesh. Given that the mechanical muscle fibres follow an element ξ-direction, the element boundaries are the logical start and end points for the mechanical fibres. The use of element boundaries as the boundaries for mechanical fibres is that the elements defining the superficial and deep compartments of the Tibialis Anterior were constrained to join at the internal tendon, so that individual mechanical fibres could begin and end at this boundary, as they do in the Tibialis Anterior.

In order to generate mechanical fibres within a muscle mesh given the specifications and constraints outlined above, the following specific parameters are required to be input into CMISS. This is done via an input file, designed to convey the grid point parameters for a particular simulation, called the .ipgrid file. For the purposes of skeletal muscle simulations, the .ipgrid format has been altered in CMISS to allow the following skeletal muscle specific parameters to be input. This format is called using the 'skeletal' tag at the end of the command line. The input parameters are:

- The number of muscle compartments (subdivisions of the muscle with different anatomical properties).
- The numbers of the elements that make up individual muscle compartments.
- The numbers of the elements in each compartment in which the mechanical fibre seed points will be generated.
- The mechanical fibre direction in each compartment (ξ direction).
- The value of ξ specifying the seed element face on which the mechanical fibre seed points will be generated (i.e. $\xi = 0$ or 1).
- The mechanical fibre diameter (D^{fibre}).

Specification of more than one muscle compartment allows for the generation of discontinuous mechanical muscle fibres within a single muscle. This is im-

portant when trying to model muscles which have areas with physiological fibres of different pennation angles, e.g., the Tibialis Anterior, or muscles with anatomically separate compartments, e.g., the Semitendinosus [80]. The elements on whose faces the mechanical fibre points are to be seeded (the seed elements) are subgroups of the individual muscle compartments. The face on which the mechanical fibres are to be seeded is calculated from the ξ-direction which the mechanical muscle fibres are constrained to follow, and the input value of ξ for the seed face (See Figure 4.7).

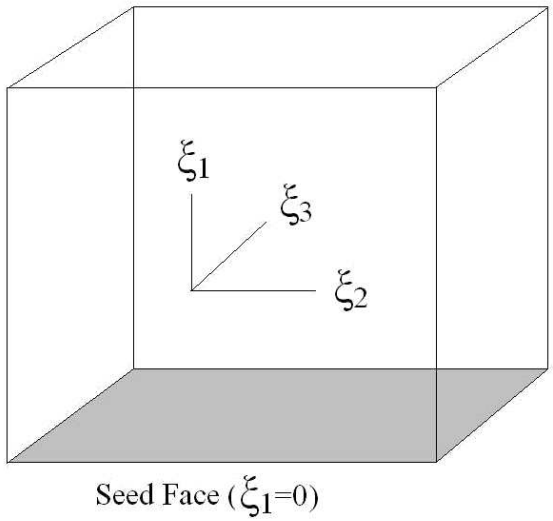

Fig. 4.7: This figure shows an individual element that has been defined to be a seed element, the fibre direction is following ξ_1, and the seed face has been set at 0, thus the seed face for the element is $\xi_1 = 0$.

Generation of the Seed Points

Once the seed elements and the seed faces have been specified as input, the seed points for each mechanical muscle fibre need to be calculated. As the cross-sectional area of the mechanical fibres must be the same, and the diameters have to be uniform in Cartesian coordinates, a subroutine that generates the seed points using these constraints has been implemented. To achieve uniform mechanical fibre spacing at a specified diameter, the following must be taken into account; In an element where the mechanical fibre direction is perpendicular to the face on which the mechanical fibres are to be seeded, evenly spaced seed points will result in evenly spaced mechanical fibres. However, if

the element is skewed, this is not the case. An adjustment to the seed point spacing, dependant on the angle of the mechanical fibre direction with respect to the seed face, can be made to allow equally-spaced mechanical fibres to be generated. As mechanical fibres are being seeded on a two-dimensional surface, the angle of the mechanical fibre direction with respect to both directions must be evaluated and accounted for before seeding the mechanical fibres. This adjustment to the mechanical fibre spacing is defined by,

$$\Delta D_{\lhd} = \frac{D^{fibre}}{sin\theta_{\lhd}}, \quad \text{where} \quad \lhd = \alpha, \beta, \tag{4.4}$$

where $\theta_{\lhd}$ is the angle of the mechanical fibre direction with respect to the seed face in direction α or β, D^{fibre} is the mechanical fibre diameter, and $\Delta D_{\lhd}$ is the seed point spacing with respect to the α or β direction. The angle needs to be calculated for both orthogonal directions to the mechanical fibre direction. With reference to Figure 4.8, the two angles can be calculated using the following relationship,

$$\theta_{\lhd} = \frac{\sum_{i=1}^{n} \theta^{i}_{\lhd}}{n}, \quad \text{where} \quad \lhd = \alpha, \beta, \tag{4.5}$$

where $i = 1..n$ are nodes of the elements, contained in the muscle compartment, in the mechanical fibre direction from the seed face. An example of an element seed face can be seen in Figure 4.9.

At each of the node points on the seed face, the angle of the mechanical fibre direction (specified by the ξ direction, so in the case of Figure 4.9, ξ_1) is evaluated with respect to the other two ξ directions (θ_α and θ_β in Figures 4.9 and 4.8). This process is repeated on the adjacent face of the seed element (in the case of Figure 4.8). If there are any elements contained in the muscle compartment that are adjacent to the seed element in the mechanical fibre direction, then the angles of the mechanical fibre direction are evaluated at the four node points on the face of these elements as well (i.e. all twelve nodes in Figure 4.8). The average length of the element in each non-fibre direction is found in a similar way to the average angle (refer to ℓ_α and ℓ_β in Figure 4.8). Using the average length of the element boundaries and the seed point

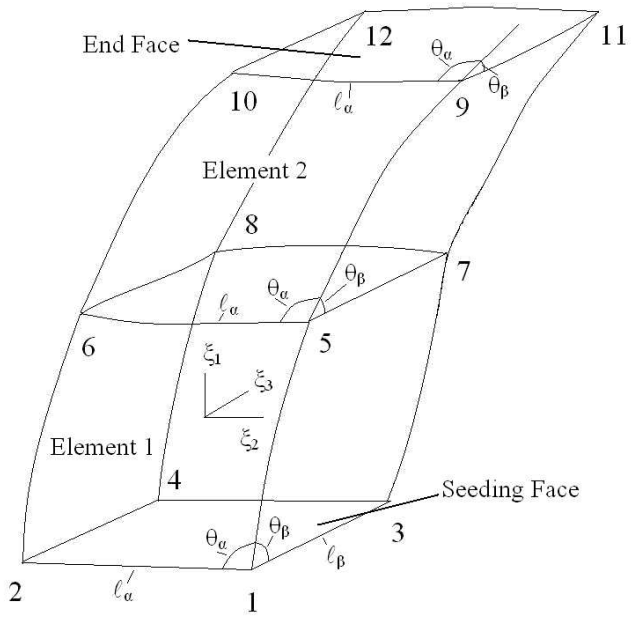

Fig. 4.8: Showing the locations of θ_α and θ_β, and ℓ_α and ℓ_β for nodes $1-12$. Note that the element defined by node points $5\ldots12$ is in the same muscle compartment as the seed element and so the mechanical muscle fibres will be grown from the $1\ldots4$ face (Seeding Face) to the $9\ldots12$ face (End Face).

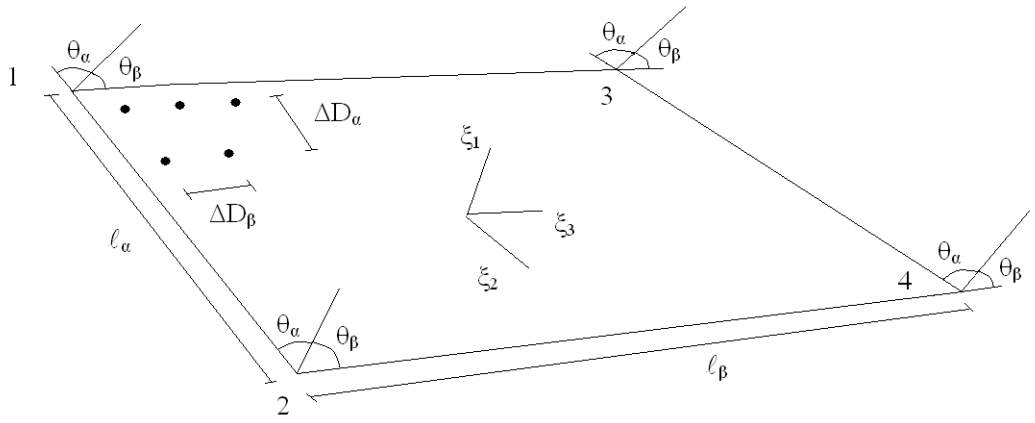

Fig. 4.9: The seed face of a seed element is shown with the four corner node points. The angles θ_α and θ_β are the angles of the ξ_1 unit vector at each corner node point with respect to the directions α and β. The lengths of the element edges ℓ_α and ℓ_β are shown for two of the four element edges. In the top left corner of the element, 5 seed points are shown. The two seed point spacings in both directions, ΔD_α and ΔD_β, are shown.

spacing (calculated from (4.4)) the number of seed points in each direction is calculated. Seed points are then spaced in even ξ increments on the seed face. Equal ξ spacing does not necessarily give the seed points equal spacing in Cartesian coordinates, and so, the shape of the muscle geometry elements is very important in maintaining consistent seed point spacing, and thus mechanical fibre diameter. The seeding technique described requires not only that the mechanical fibres follow an element ξ direction, but also that the perpendicular element faces be as close to rectangular as possible, and approximately the same dimensions along the mechanical fibre direction.

Growth of Mechanical Fibres From the Seed Points

After the seed points are calculated, mechanical grid points of even spacing ($GP_{spacing}$) need to be generated along the mechanical fibre direction to represent the mechanical muscle fibres. To achieve this, firstly the geometric coordinates of the seed point being extended are calculated. Then a test point is generated with the same ξ coordinates as the seed point, with the exception of the ξ_i value, where i is the mechanical fibre direction. The ξ_i value is modified by $\Delta\xi$. Being able to step in just one ξ direction is a direct benefit of creating the elements which follow the physiological fibre direction. The geometric coordinates of this test point are then calculated, and the distance between the test point and the seed point is calculated (ΔX), as in (4.6) and Figure 4.10.

$$\Delta X = \sqrt[2]{(x_1 - x_2)^2 + (y_1 - y_2)^2 + (z_1 - z_2)^2} \tag{4.6}$$

If $|GP_{spacing} - \Delta X| > ErrTol$ then the $\Delta\xi$ value is modified using the following equation,

$$\Delta\xi^{new} = \frac{\Delta\xi^{old}}{\frac{GP_{spacing} - \Delta X}{GP_{spacing}}}. \tag{4.7}$$

The distance between the two points (ΔX) is then recalculated. The $\Delta\xi$ value is iterated using (4.6) and (4.7) until the calculated ΔX value satisfies,

$$|GP_{spacing} - \Delta X| \leq ErrTol. \tag{4.8}$$

The test point then becomes a mechanical fibre grid point and the next test point is determined to be $\Delta\xi^{new}$ away in the mechanical fibre direction. So in

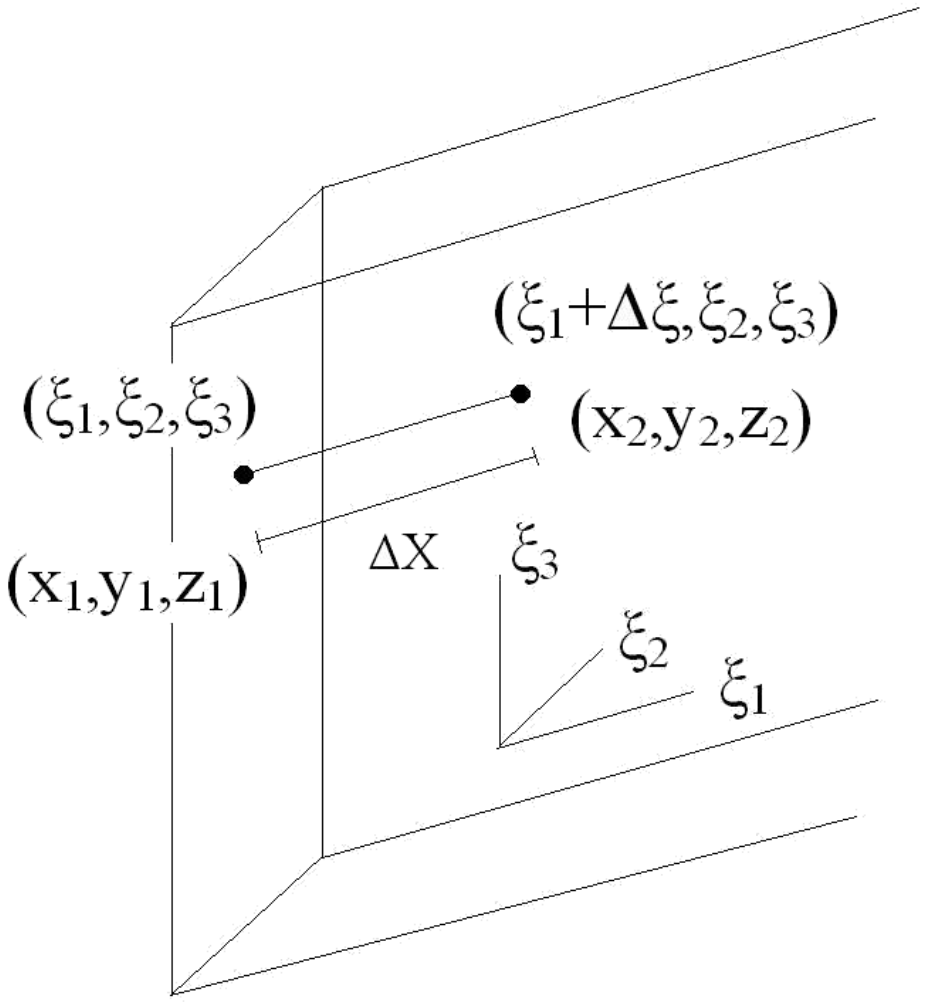

Fig. 4.10: This figure shows the location of the ξ, and the geometric coordinates, of the seed point on the element face and new test grid point. The distance between the two points is calculated in Cartesian space as ΔX.

general (using the example of a ξ_1 fibre direction) the local ξ coordinates of mechanical grid point $n+1$ are described as,

$$(\xi_1^{n+1}, \xi_2, \xi_3) = (\xi_1^n + \Delta\xi^{new}, \xi_2, \xi_3). \tag{4.9}$$

The updated $\Delta\xi$ is used as the initial guess for the displacement of the next mechanical grid point. The $ErrTol$ used in this work is set to be $0.01 \cdot GP_{spacing}$.

The mechanical fibre growth routine is implemented so that if the ξ coordinate in the mechanical fibre direction is greater or less than 1 (i.e. the test point is outside the current element), then if, as in Figure 4.8, there is an element in the mechanical fibre direction that is within the same muscle compartment (i.e. Element 2 in Figure 4.8), the mechanical fibre grows into the adjacent element. The growth through element boundaries is achieved by keeping two of mechanical fibre direction ξ values constant, and either adding or taking away 1 from the ξ value in the mechanical fibre direction (depending on whether the mechanical fibres are being grown positively or negatively in ξ space). Thus ΔX can be calculated across element boundaries and $GP_{spacing}$ can be maintained as the mechanical fibres move through element boundaries.

4.3 Representing Functional Organisation of Skeletal Muscle

The details of the functional grouping of mechanical muscle fibres are presented in this Section. The required properties of the functional grouping, as derived from Section 2, are first outlined (Section 4.3.1). Following this, the grouping of the mechanical fibres generated within the three-dimensional mesh into the calculated motor units is described (Section 4.3.3).

4.3.1 Functional Properties

In order to be able to perform physiologically realistic electromechanical simulations it is necessary to add further functionality to the model. Each individual mechanical muscle fibre needs to be assigned a physiological fibre type (fast or slow) and needs to be grouped into a motor unit. This process is again

automated within the CMISS framework, and required further input via the .ipgrid file. The following extension to the skeletal muscle model has been included in the proposed framework:

- The total number of motor units (MU).
- The ideal motor unit fibre ratio between the last (biggest) motor unit and the first (smallest) motor unit (MU_{ratio}).
- The percentage of mechanical fibres that are to be slow twitch.
- The desired density of mechanical fibres within a motor unit territory (ρ_{MUT} fibres per mm^2).
- The percentage of the slow mechanical fibres to have their location non-randomly selected (location weighting $0 - 100\%$).
- The centre of the weighting function.
- The value of the weighting function $WTFN$ (the larger this value, the more likely the fibres are to be located near the specified weighting point).
- The same weighting input for fast twitch mechanical muscle fibres.

4.3.2 Calculating the Motor Unit Distribution

First, the motor unit distribution within the muscle is determined. The distribution is defined to be an exponential function and is based on the work of Enoka *et.al.* [30]. The general equation for calculating the number of fibres in each motor unit is given by

$$Mu_i = Mu_1 + exp\left(\frac{\ln \frac{Mu_n}{Mu_1}}{(MU-1)\cdot i}\right) \tag{4.10}$$

where Mu_i, $i = 1..n$, is the number of fibres in motor unit i, Mu_n is the number of fibres in the last (largest) motor unit and MU is the number of motor units. Mu_1 and Mu_n can be calculated in an iterative process by using

the ratio of Mu_n to Mu_1 (MU_{ratio}) and the formula

$$Mu_1 = \frac{T_{tot} \cdot ln\left(MU_{ratio}\right)}{MU \cdot \left(MU_{ratio} - exp\left(ln\frac{MU_{ratio}}{MU}\right)\right)} \tag{4.11}$$

where T_{tot} is the total number of fibres generated in the three-dimensional muscle geometry. Note, rearranging (4.10) leads to (4.11). Based on (4.11) and MU_{ratio}, one can compute the MU_n for the current iteration of MU_1. Using the new values of MU_1 and MU_n, (4.10) is used to calculate the motor unit distribution. The value for each motor unit is rounded to an integer and summed to give the total number of fibres in the motor unit distribution, MU_{Ftot}, which is then compared to the total number of mechanical fibres that has been generated in the muscle mesh, T_{tot}. The values of Mu_n and Mu_1 are then iterated using (4.11) and (4.10) using the following steps:

1. MU_n is calculated from MU_1 (using (4.11) and the input MU_{ratio}).
2. The motor unit distribution and MU_{tot} are calculated using (4.10).
3. If $T_{tot} - MU_{Ftot} < 0$ then $MU_1 = MU_1 - 1$, else if $T_{tot} - MU_{Ftot} > 0$ then $MU_1 = MU_1 + 1$.
4. The previous three steps are repeated until the value of MU_1 giving the lowest $\mid T_{tot} - MU_{Ftot} \mid$ value is determined.
5. MU_n is then iterated in a similar way (keeping MU_1 constant) until the lowest $\mid T_{tot} - MU_{Ftot} \mid$ value is determined.
6. If $T_{tot} - MU_{Ftot} \neq 0$ then the difference is subtracted from MU_n (without recalculating the MU distribution).

Thus the following two criteria are met. The number of fibres in the calculated motor unit distribution are the same as the number of mechanical fibres generated in the muscle mesh, and the ratio of the actual Mu_n/Mu_1 is as close as possible to the ideal MU_{ratio}. Motor units are defined to contain slow fibres starting from Mu_1 until the total number of fibres in these slow motor units is as close as possible to the input percentage of slow muscle fibres defined in the .ipgrid file, the balance of the motor units are defined as containing fast type fibres.

4.3.3 Assigning Fibres to Motor Units

After the motor unit distribution has been calculated, each of the generated mechanical fibres in the muscle mesh needs to be associated to one of the motor units. This assignment is achieved by defining motor unit territories within the muscle mesh and then assigning random mechanical fibres within the territories to a motor unit. The location of each motor unit territory centre point is either randomly selected from all of the mechanical fibre centre points, or if a weighting is specified, it is selected randomly using a Gaussian function and the specified weighting value. Gaussian weighting of the motor unit territories is achieved as follows.

The distances of the centres of all of the mechanical muscle fibres (potential motor unit territory midpoints) from the weighting centre are calculated using,

$$MPR_j = \sqrt{(x_j - X^W)^2 + (y_j - Y^W)^2 + (z_j - Z^W)^2}, \tag{4.12}$$

where MPR_j is the distance of mechanical fibre midpoint j, (x_j, y_j, z_j), from the weighting centre, (X^W, Y^W, Z^W). The range specified by the minimum and maximum distance from the weight centre ($MPR_{max} - MPR_{min}$) is divided into 100 equally spaced groups (or bins, Bin_d, where $d = 1 \ldots 100$). Each mechanical fibre midpoint is assigned to a bin depending on the midpoint's distance from the weighting centre. This process results in each mechanical fibre midpoint being grouped into bins with other midpoints of approximately the same radius from the weight centre, and thus Bin_d is in fact an array of midpoints, $Bin_d[1 \ldots noMidpoints_d]$, where $noMidpoints_d$ is the number of fibre midpoints in Bin_d. The centre point of motor unit i can then be selected using the following set of equations.

$$d = R_{Gauss} * \frac{100}{3} * WTFN, \tag{4.13}$$

$$CentreMU_i = Bin_d[|Rand * noMidpoints_d|], \tag{4.14}$$

where R_{Gauss} is a random number with a Gaussian (normal) distribution, a centre of 0 and a standard deviation of 1, $WTFN$ is the value of the weighting function used (input), 100/3 is a factor that scales the Gaussian distribution so that the first standard deviation contains a third of the possible bins, $Rand$

is a random number between $0 \ldots 1$, and $CenterMU_i$ is the centre point of motor unit i.

The value of $WTFN$ alters the probability of the selected bin being close to the weighting centre. As can be seen in (4.13), the factor of 100/3 scales the random Gaussian number so that its standard deviation is 100/3. Thus specifying a $WTFN$ value of < 1 will increase the range of bins contained within 1 standard deviation, and decrease the probability of a motor unit centre being close to the weighting centre. The weighting protocol is demonstrated in Figure 4.11. A $WTFN$ value of 1 is used, giving a 68.26% probability that the bin selected will be within the closest third of possible bins to the weighting point. The above mechanism of weighting the motor unit territory locations is not derived from a biophysical mechanism. Instead it represents an attempt to reproduce the areas of the motor unit territories as described by [17, 35, 80, 101].

Once the centre of the motor unit territory has been calculated, the distance between the motor unit centre and the centre of all mechanical fibres that are available to be grouped into motor units (those that have not already been selected for a motor unit) is calculated (same procedure as (4.12)). Mechanical fibres whose centre points lie within the radius of the motor unit territory are grouped as the pool of possible mechanical fibres for the motor unit. The radius of the motor unit territory is dependant on the number of mechanical fibres within the motor unit and is selected as follows:

$$R_i = \sqrt{\frac{Mu_i}{\rho_{MUT} \cdot \pi}}, \tag{4.15}$$

where R_i is the radius of motor unit territory i, and ρ_{MUT} is the input density of the motor unit territories. The mechanical fibres for motor unit i are then selected randomly from the pool of mechanical fibres defined by motor unit territory i and can no longer be selected for any other motor unit. Examples of mechanical fibres grouped into motor units using this method can be seen in Figure 4.12.

If there are insufficient mechanical fibres available in the motor unit territory pool to meet the requirements of the motor unit being specified, the radius of the territory is increased by 5% ($R_i = R_i * 1.05$ until the number

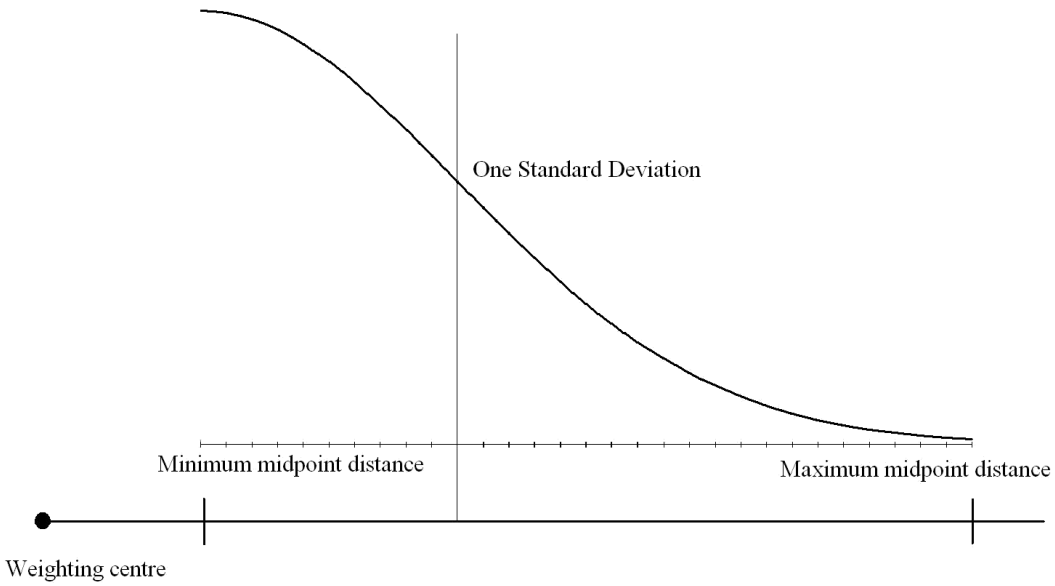

Fig. 4.11: The probability of a bin being selected given a weighting function value of one. The point on the far left denotes the weighting centre. The two points denoting the closest, and most distant mechanical muscle fibre centres are shown on the horizontal line. The distance between the closest and most distant mechanical fibre centres is divided into equally spaced subdivisions (in the case of this figure, 30 divisions, in the framework, 100 divisions). The centre of each mechanical muscle fibre is by definition located between the closest and farthest point, and the centre points are assigned to one of the subdivisions (bins). The half bell curve denotes the probability that a bin is selected to be a motor unit centre. The bell curve associated with a weighting function ($WTFN$) of 1 is depicted. The vertical line depicts the location of 1 standard deviation, thus the probability of a mechanical fibre from one of the closest third of the bins being selected to be a motor unit weighting factor is 68.26% (refer to (4.13)). A $WTFN$ value greater than one would shift the location of the 1 standard deviation line to the right, decreasing the likelihood of motor units being located near the weighting centre. If no weighting is used, the probability of any one bin being selected is equal.

of mechanical fibres in the pool is greater than or equal to the number of mechanical fibres required for MU_i. Increasing R_i can lead to a large fluctuation in the actual densities of the motor unit territories. For example, if the value of the specified weighting function is very high then the mechanical fibres surrounding the weight point will be assigned very quickly, meaning that subsequent motor unit territories (which will also have their centre located close to the weight point) will have to extend their radius to capture enough mechanical fibres to fill their motor unit. Also as a result of increasing R_i, the last (largest) motor unit can have a territory that covers the entire muscle, as all remaining mechanical fibres in the three-dimensional geometry need to be selected. While this is physiologically realistic, it can cause a variation in the density of this motor unit compared to the preceding motor units.

Generating accurate motor unit territories in the model is further complicated by the fact that a rigorous description of all the parameters that define the distribution of physiological fibres in a motor unit is not available from the literature [80]. The motor unit territory is defined by Bodine-Fowler *et.al.* to be the smallest possible convex area that contains all of physiological fibres of the motor unit [14]. Roy *et.al.* [101] define it as the outer perimeter of the motor unit (physiological) fibres. These descriptions and their associated densities predominantly describe the motor unit territory in two dimensions, and even though Roy *et.al.* do characterise motor units in three-dimensions, densities can only be meaningful in two dimensions if the number of physiological fibres is to be used as the dependant variable. This presents problems given that any measurement of density is only valid at a specific cross-section of the muscle, and is further complicated if the muscle has (physiological) fibres of more than one pennation angle, with motor unit (physiological) fibres being distributed across the muscle (as any plane through the muscle is by definition oblique to at least some of the (physiological) fibres).

4.4 Validation

The validation of the distribution of motor units throughout the Tibialis Anterior is very difficult as not much data describing the distribution of the motor unit territory in detail exists [80]. Motor unit territories have generally been

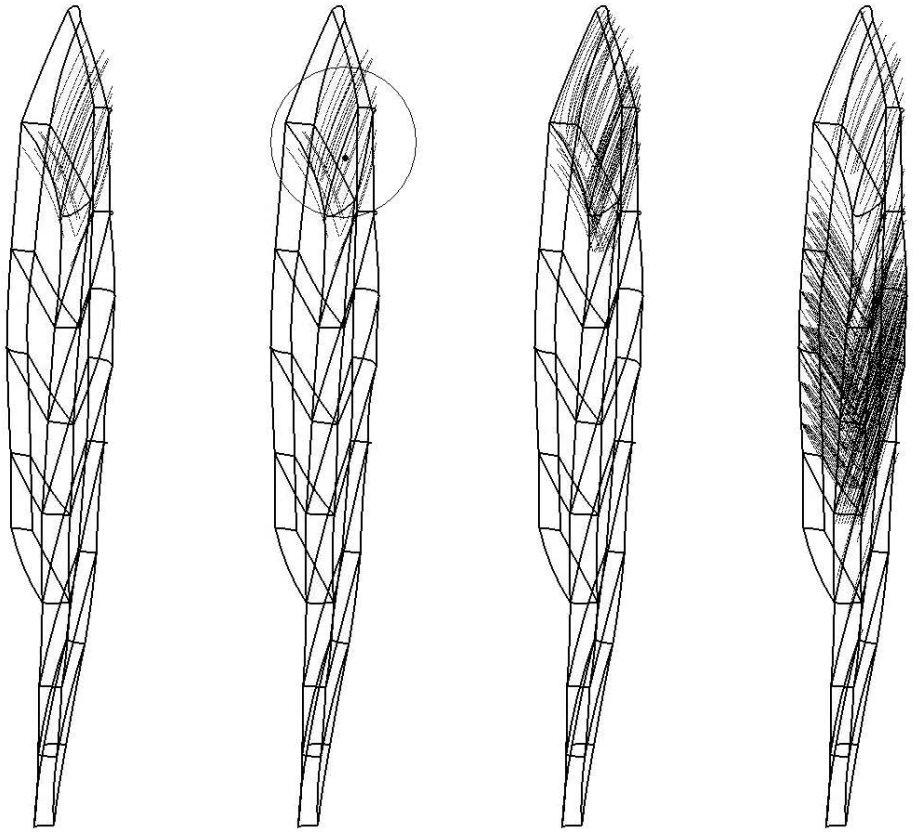

Fig. 4.12: A depiction of the Tibialis Anterior. In this case the mechanical fibres within the muscle have been divided into 10 motor units. Subfigures (a), (c) and (d) show the mechanical fibres contained in motor units 1, 5 and 10 respectively. Subfigure (b) shows motor unit 1 along with the centre point of the motor unit territory and the radius that was used to select the mechanical fibres for that motor unit. Of interest is the large change in the number of mechanical fibres between motor unit 1 and 10. Also of note is that the slow type mechanical fibres (thus the small motor units) were weighted to be near the proximal end of the muscle, and as can be seen, motor units 1 and 5 are made up of mechanical fibres that are closer to the proximal end of the muscle.

viewed in two dimensional slices [14, 80]. This has been done in the cat by selecting a single motor neuron and stimulating it to deplete the physiological muscle fibre glycogen stores [80]. The muscle was then sectioned and stained for glycogen content. In this way, the physiological fibres of the motor unit that was being stimulated could be distinguished from the other fibres of the muscle. The metric used to describe the size of the motor unit is the motor unit density $fibres/mm^2$ [101, 14, 117], with reported values ranging between $10 - 30 fibres/mm^2$ [101, 14, 117]. The above method has also been extended into three dimensions by sectioning the muscle in to $10 - 20\mu m$ thick segments, repeating the straining procedure and associating physiological fibre points using three-dimensional visualisation tools [101]. Motor units occupy three-dimensional space. A two-dimensional metric (i.e. muscle slices) is unable to capture a full description of geometry, which is needed in the modelling context presented. Physiological muscle fibres can terminate, enter the two-dimensional slice at different angles, and furthermore, a density value gives no information on the shape of the motor unit.

In conclusion the structural and functional modelling framework presented is able to replicate many feature of skeletal muscle, given the limitations of the current body of knowledge. The mechanical fibres generated by the modelling framework are evenly spaced, their origin and insertion are anatomically realistic and their orientation agrees with published data [67]. The motor unit distribution is consistent with published physiological data [80] and is also similar to the method used by other numerical studies [30, 117]. The motor unit territories are located realistically through the muscle volume so that the spatial distribution of fibre types is able to be conserved, and the motor unit territory size is consistent with published physiological data [101] as well as the methods of other numerical work [117]. The motor endplate band, as defined by the centre points of all the mechanical muscle fibres, forms a parabola with its apex at the proximal end as described in Aquilonius *et.al.* [4].

4.5 Modelling the Activation of Skeletal Muscle

In Chapters 4.1 and 4, representations of the physical structure and functional organisation of the Tibialis Anterior were implemented within the modelling framework. Chapters 3 and 4 also described how the physiological output is used to create mechanical output. In this section, the methods used to activate the modelling framework are presented. Firstly, the protocols and equations used to replicate normal physiological muscle function are described, followed by the approach used to model muscle activation during Functional Electrical Stimulation.

Muscle is a finely tuned and highly responsive actuator. The force that is produced from muscular contraction is controlled via two main mechanisms, recruitment level and rate coding. The recruitment level is the number of motor units that are active at any one time, the more motor units recruited, the greater the force generated. Rate coding refers to the modulation of motor unit discharge rates [62], in general increasing the stimulation frequency of a motor unit increases the amount of force produced, although this does not hold true over certain physiological maxima, or in cases of fatigue. In order for a motor unit to be activated, the sum of all of the excitatory and inhibitory signals reaching the motor neuron cell body (soma) must be enough to depolarise the membrane of the constituent muscle fibres past the Threshold Voltage [111]. Each of these signals modifies the potential of the soma by

$$PSP_{ss} = I_N \cdot R_N, \tag{4.16}$$

where PSP_{ss} is the steady-state synaptic potential recorded at the soma, I_N is the effective synaptic current as seen by the soma, and R_N is the impedance of the cell. It has been shown that cellular impedance can vary $8 - 10$ fold, depending on the cell surface area and the membrane resistivity [48]. Effective synaptic current has been shown to co-vary with cellular impedance [48]. Motor units are recruited, and de-recruited, in a highly conserved order. The cellular impedance and effective synaptic current are theorised to be the source of this variation in recruitment levels [48].

In order to include the effect of synaptic current on recruitment into a

model of the motor neuron pool, it is possible to consider the level of effective current required to induce repetitive activation of the motor neuron over the entire motor neuron pool. This was first done by Heckman and Binder [49] and later followed up by Fuglevand *et.al.* [36] where this was referred to as the 'excitatory drive'. Thus, using known relationships from experimental data, it is possible to specify both recruitment level and rate coding for the entire motor pool with a single variable. The implementation of this concept in this work is described below.

4.5.1 Physiological Recruitment

In order to model the activation of muscle under normal physiological conditions, a modified version of the Fuglevand *et.al.* 1993 model [36] was implemented in CMISS. This model consists of a prediction of recruitment level and rate coding with respect to excitatory drive. The recruitment threshold of excitation (RTE) is defined to be the level of excitatory drive that will cause a motor unit to fire at its minimum frequency, and is assumed to be exponentially distributed over the motor unit pool. This is in accordance with the distribution of motor neuron sizes, and is represented with the following equation,

$$RTE_i = e^{(ln(RR)/n)\cdot i}, \tag{4.17}$$

where RTE_i is the recruitment threshold excitation for motor neuron i, RR is the range of the recruitment threshold values, and n is the total number of motor units. A motor unit is defined as being active if the excitatory drive to its motor neuron is greater than or equal to its recruitment threshold excitation (i.e. $E(t) \geq RTE_i$).

The determination of the rate coding for each motor neuron with respect to the excitatory drive was broken down into four steps.

- Calculation of the minimum firing rates of the motor neuron.

  The Fuglevand *et.al.* model assumes a uniform minimum firing rate over the motor neuron pool [36]. This is supported by findings that during voluntary contraction in human muscles, minimum firing rates are similar for all motor neurons [21, 79]. However, other studies using current

injection have found a relationship between the minimum firing rate and the recruitment threshold of a motor neuron [36]. For the purpose of generality, the model implemented here allows a linearly varying minimum firing rate for the motor neurons.

- Determining the excitatory drive to firing rate relationship for the motor neurons.

  The average firing rate is assumed to vary linearly with the excitatory drive supplied to the motor neuron. This is represented in the equation below.

$$ISI_i = \begin{cases} G_e \cdot (E(t) - RTE_i) + MFR & \text{if } E(t) >= RTE_i, \\ 0 & \text{otherwise,} \end{cases} \tag{4.18}$$

  where ISI_i is the average Inter-Spike Interval for the motor neuron at excitatory drive level $E(t)$, G_e is the gain of the motor neuron as $E(t)$ increases and MFR is the minimum firing rate of the motor unit. This equation is valid for all $E(t)$ values equal to, or greater than, the recruitment threshold excitation for the motor unit.

- Calculation of the peak firing rates of the motor neurons.

  The peak rate of firing of the motor neurons in a human motor pool is believed to vary depending on the recruitment threshold of the motor neuron, however the exact relationship has yet to be resolved [36]. Studies have shown the peak firing rates of motor units can vary with contraction intensity, the direction of contraction and motor unit fibre type [25, 21, 97, 42]. It is possible to investigate the result of changing the peak force across the motor unit pool by representing the distribution linearly with the following equation.

$$PFR_i = PRF_1 - PFRD \cdot \frac{RTE_i}{RTE_n}, \tag{4.19}$$

  where PFR_i is the peak firing rate of motor neuron i, PFR_1 is the peak firing rate of the motor neuron with the lowest recruitment threshold and RTE_n is the peak firing rate of the motor neuron with the highest

recruitment threshold.

- Calculation of the timing of each activation signal, for each motor neuron, using a Gaussian distribution to determine variability.

  Motor neuron firing is determined by the excitatory drive to the cell body, and in vivo this value fluctuates over time, which causes motor neurons to fire at intervals randomly distributed about the mean firing rate (ISI) [36]. To represent this phenomenon the time of the first activation is calculated by

$$Stimulation_{i,0} = ISI_i \cdot 0.5 + ISI_i \cdot CV \cdot Z, \tag{4.20}$$

  where Z is a random number with a Gaussian distribution of mean 0 and standard deviation 1, and CV is the coefficient of variation of the stimulation times. This provides a starting point for the following algorithm which calculates the time of the $j + 1^{st}$ activation.

$$Stimulation_{i,j+1} = ISI_i + ISI_i \cdot CV \cdot Z + Stimulation_{i,j}, \tag{4.21}$$

  The coefficient of variation, CV, can be modified to determine the effects of activation variability on the whole muscle force response.

In order to be able to compare the relative performance of muscles with different ranges of recruitment thresholds, different gains, and different maximum and minimum firing rates, the RTE_i values were normalised. The normalisation of RTE_i also simplified the implementation of inverse recruitment (see Section 4.5.2). The normalisation factor that was selected was the $E(t)$ value that would cause the last motor unit, MU_n, to reach its peak firing rate (E_{max}), and is calculated as follows,

$$E_{max} = \frac{PFR - MFR}{G_e} + RR. \tag{4.22}$$

Visualisation of the firing rate verses $E(t)$ for the largest motor unit, and the basis for (4.22), can be seen in Figure 4.13. In the case of MU_n, RTE_n by

definition (Equation 4.17) is RR. From this point, on RTE_i will refer to the normalised value.

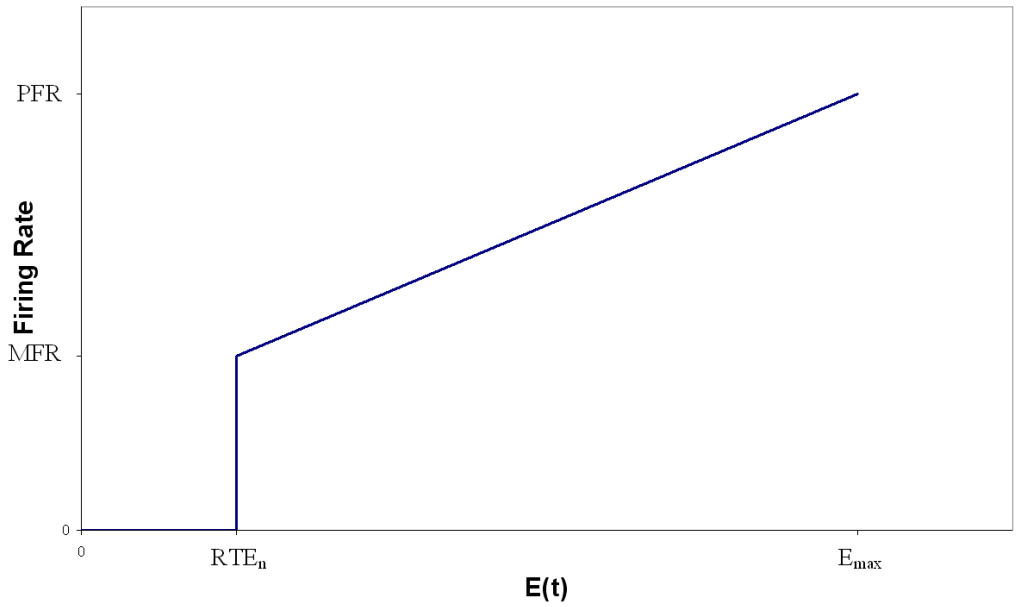

Fig. 4.13: Firing rate as a function of $E(t)$ for MU_n. At $E(t) = RTE_n$ the firing rate of MU_n is MFR. The peak $E(t)$ value occurs when PFR is reached and is denoted E_{max}. The E_{max} is used to normalise all RTE_i values as increasing $E(T)$ above E_{max} no longer changes the rate coding of the motor units (all motor units already at PFR).

4.5.2 Inverse Recruitment

Inverse recruitment is a phenomenon that occurs during Functional Electrical Stimulation and results in a reversal of the normal recruitment order of motor units (refer Section 2). Inverse recruitment can thus be modelled using the following equation,

$$RTE_i^{inv} = 1 - RTE_i. \tag{4.23}$$

Thus, (4.23) gives an accurate representation of the order of recruitment. Moreover, (4.23) qualitatively represents the size of the applied electric field required to activate the motor neurons, as the diameter of the α-motor neurons is exponentially distributed across the motor pool (from Henneman *et.al.* , the diameter of motor neurons is correlated with the motor unit size [53, 52]), and

the excitability of a motor neuron to external stimulation is correlated to the inverse of its diameter [29]. When modelling inverse recruitment, the timing of each motor unit depolarisation is set at the driving frequency of the applied electric field ($Hz_{inverse}$), and thus there is no need for calculations of ISI or firing times.

It should be noted that the $E(t)$ value does not quantitatively represent any specific applied current or voltage but rather, in combination with the RTE^{inv} values, replicates the order and 'intensity' required to activate motor units, via the α-motor neurons using an external stimulus. As the actual motor neurons and the external stimulus, that are activating them, are not explicitly modelled, there is very little justification for assigning a specific numerical voltage or current value to the inverse recruitment process. Instead the generalised recruitment pattern is being replicated independent of any absolute measure of applied electrical stimulus.

Chapter 5

Results of Whole Muscle Activation Simulations

In this chapter simulation protocols are outlined and the results of the activation of the full muscle are presented. Section 5.2 details the initial numerical experiments and explores a number of downscaling techniques used to reduce the computational load. In Section 5.3, simulations are run to demonstrate the ability of the numerical framework to model changes in a number of intrinsic muscle properties, and to assess the effect, if any, of these changes. The output of inverse recruitment simulations are also presented in Section 5.3, showing marked changes in the force output of the muscle. Finally, in Section 5.4, the possibility of designing an inverse recruitment protocol that matches normal physiological function is investigated. In addition a similar protocol is constructed for a Tibialis Anterior muscle with a different fibre composition (representing the physiological changes due to FES) to determine if and how the response of muscle to FES changes over time.

In all cases, the Tibialis Anterior was simulated as being in isometric conditions. To achieve the isometric representation of the muscle, the Finite Element nodes composing the proximal and distal faces of the muscle are constrained to be fixed in space. Fixing the nodes in effect represents fixing the ankle joint so that it cannot rotate. The total muscle force is then calculated from the reaction force at the fixed muscle boundary as the vector sum of all of the fixed boundary node forces.

5.1 Numerical Experiment Protocols

Each simulation was run for a time of length $Time_{sim}$, which was broken down into equally spaced time intervals of T_{phys}. Each numerical stimulation then consisted of the following two basic steps. First, the Bidomain simulations for each $MURF$ were run for input time T_{phys}. Then the physiological output for T_{phys} was used as an input into the mechanics simulation, by copying the A_1 and A_2 values calculated in the $MURFs$ to the mechanical grid points, and then using the constitutive law (Section 3.1.3) to calculate the whole muscle reaction. The mechanics solution necessarily lasted for the same time period as the Bidomain solution (T_{phys}). The Biodomain and corresponding mechanics simulations were repeated, in intervals of T_{phys}, for the duration of $Time_{sim}$. The experiments were able to be run using distinct Bidomain and mechanics steps for the following reasons.

- There was no force or length feedback to the Shorten *et.al.* transmembrane model, and so the only data needed for each Bidomain simulation was the activation timing (from rate coding).
- The kinetics of A_1 and A_2 were of the order of $10 - 100$ times slower than the kinetics of the Action Potential, and so the time scale of the mechanics step (also T_{phys}) could be of the order of $100ms$, allowing a huge computational speed-up, without sacrificing accuracy.

The experimental protocol that was used was as follows. A linearly increasing $E(t)$ function was applied to the muscle, the motor response to the function was calculated, and the resulting muscle force as a result of the motor activity was determined. A break down of the steps involved in the simulation protocol is:

1. Activation times, as calculated from (4.20) and (4.21), were applied to each $MURF$ and the simulations were run for T_{phys} (A_1 and A_2 values were stored at time intervals of $1ms$).
2. The output, A_1 and A_2 values, from each $MURF$ was mapped to the associated mechanical grid points of mechanical fibres within the Tibialis Anterior geometry.

3. The volume average of the mechanical grid points A_1 and A_2 values was taken around each Gauss point, and these values were used to calculate the active and passive stress components of the macroscopic constitutive law.

4. The muscle deformation was calculated for each $1ms$ time step (2-4 were repeated for every $1ms$ time step in T_{phys}).

5. At the end of the mechanics simulation $E(t)$ was calculated, either as a linear function or as a result of comparison with F_{in}.

6. The new $E(t)$ was used to calculate new activation times for the $MURFs$.

7. These steps were repeated for the total time of the muscle simulation.

The specific protocol used in the simulations involved a total stimulation time ($Time_{sim}$) of $500ms$ with the mechanics solutions being computed, and thus the physiological stimulation being updated, every $100ms$ (T_{phys}). The linearly increasing $E(t)$ function was necessarily modelled using a step function (refer to Figure 5.1), although the linear function is the desired input to the motor pool (similar to the work of [36, 49]). A step function was used because the design of the simulations required that the input to the Bidomain simulations was calculated at the end of the mechanics simulation (so that mechanical feed back could be included at a later stage), and thus the $E(t)$ was unable to be modified during the Bidomain simulation (i.e. $E(t)$ was constant for each individual T_{phys}). As a result a step function was used as it is the closest approximation to a linear function using discrete constant values. As can be deduced from Figure 5.1, as $T_{phys} \rightarrow 0$, the step function tends towards a linear function. However, if T_{phys} were to be reduced below $100ms$, the ability to represent the firing frequency of slow motor units would begin to accumulate errors and eventually fail. A motor unit firing at $10Hz$ has a period of $100ms$ and so to it would be impossible to maintain a $10Hz$ stimulation frequency over the duration of multiple T_{phys} steps without the use of some history component. A history component was not implemented, and T_{phys} was set at $100ms$ for all simulations as the error caused by using a step approximation was not believed to warrant further attention.

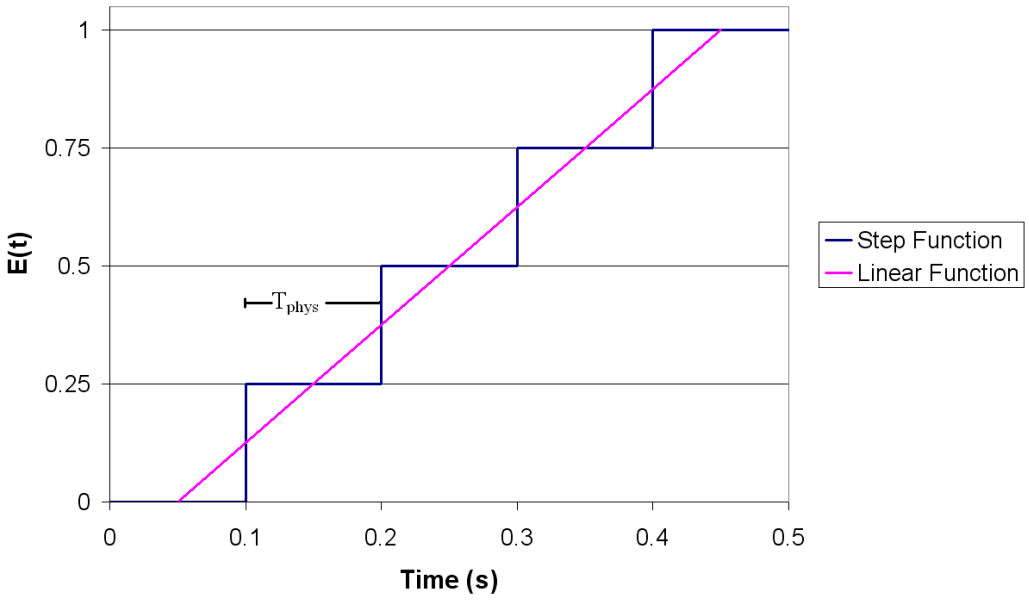

Fig. 5.1: The linear function shown is the desired $E(t)$ input function for the subsequent test simulations. The ramp increase in $E(t)$ allows a full range of recruitment and rate coding of all motor units. As the simulations are run in discrete steps, of duration T_{phys}, the approximation that is used to the linear function is shown as the step function.

The force produced as a result of the activation of the motor units is calculated as the sum of all of the reaction forces at the fixed boundary of the muscle. For all experiment the reaction forces at the distal face of the Tibialis Anterior were calculated, however, for equilibrium, these had to be identical to the reaction forces at the proximal end. It should be noted that the magnitude of the calculated force is not directly related to the actual force magnitude of a real Tibialis Anterior for the following reasons. The A_1 and A_2 values are normalised to their respective maximum values, the constitutive law is not accurate enough to give realistic force values, and the magnitude of the A_1 and A_2 need to be further scaled to prevent numerical instabilities in the mechanics solution step. Thus the force produced by the simulations in the following chapters is a qualitative representation of the force behaviour of the Tibialis Anterior under different conditions, and does not represent the absolute magnitude of force produced by the real Tibialis Anterior.

5.2 Whole Muscle Simplifications

This section details numerical experiments designed to decrease the computational expense of full muscle Tibialis Anterior simulations. Although it would be theoretically possible to model every single physiological muscle fibre and motor unit with the Tibialis Anterior, the time and computational power required would be restrictive, with millions of grid point being required. It was therefore of interest to determine what effect scaling of muscle properties would have on the simulation output. A number of potential simplifications were identified.

1. A reduction in the mechanical grid point discritisation level of mechanical fibres within the simulation.

2. Representing a smaller number of fibres in the mechanics mesh.

3. A reduced number of motor units within the muscle.

Simulations to test the validity and limitations of the above simplifications were run and the outcomes are displayed in the following sections. The muscle force plots generated by modifying each of the above simplification criteria were compared using the methods specified in Secion 5.2.

Data Analysis

In order to provide a quantitative measure of muscle force smoothness, and also to compare the output of different muscle simulations, a polynomial function was fitted to the data. The deviation of the muscle force data from the best fit gives an indication of the smoothness of the data, and best fit curves can be compared between simulations. The force output from the full muscle simulations is fitted to a 6^{th} order polynomial using the method of least squares to determine the coefficients of,

$$y = c_0 + c_1 x + c_2 x^2 + c_3 x^3 + c_4 x^4 + c_5 x^5 + c_6 x^6, \tag{5.1}$$

where $c_0 \dots c_6$ are constants. A 6^{th} order polynomical was used as it provided a visually accurate fit to the data and was easy to implement in a Microsoft Excel spreadsheet. The deviation of the force output from the best fit curve is then given by the R^2 value, which is defined as,

$$R^2 = 1 - \frac{\sum \left(Y_i - \hat{Y}_i \right)^2}{(\sum Y_i^2) - \frac{(\sum Y_i)^2}{n}}, \tag{5.2}$$

where Y_i are the force output values, i is the range of discrete x values where Y exists, and $\hat{Y}_i$ are the fitted values coming from (5.1). The R^2 value gives an indication of the closeness of the sixth order polynomial approximation to the data, with a value of 1 indicating a perfect fit.

5.2.1 Fibre Discritisation Level

For an accurate solution of the Shorten *et.al.* cellular model using the Bidomain equations, a Bidiomain grid point spacing of $0.0625mm$ is ideal (see Section 4.1). As the output of each simulated $MURF$ is being mapped to the associated mechanical grid points within the Tibialis Anterior mesh, and not being calculated directly on the mechanical grid points, there exists the possibility of sampling the output of the $MURF$ (the Bidomain grid points) at a different grid point spacing. The effect, if any, of the change in mechanical grid point discritisation was the subject of the following simulations.

To test whether a change in mechanical grid point spacing would affect

the output of the mechanics simulation, two different full muscle mechanics simulations were run, each with the same physiological input. The following input was used:

- Mechanical grid point spacing: $0.625mm$, $6.25mm$
- Mechanical fibre diameter: $2000\mu m$
- Number of motor units: 10
- Motor unit fibre ratio (MU_{ratio}): 10
- Percentage of slow type mechanical fibres: 70%
- Motor unit territory density: $0.01 fibres/mm^2$

Both simulations were run for $500ms$ with a linearly increasing $E(t)$ value (updated every $100ms$). Note that these input values were not selected to replicate physiological data, or the data of other numerical models, but rather so that comparison experiments could be run. The force versus time plots can be seen in Figure 5.2 and the same force plot along with the corresponding activation times of the motor units can be seen in Figure 5.3. A simulation with a mechanical grid point spacing of $0.0625mm$ was not run as it was computationally expensive. The effect of increasing the coarseness of the mechanical grid scheme can be seen using spacing of $0.625mm$ and $6.25mm$.

As depicted in Figure 5.2, the force output plots for a mechanical grid point spacing of $0.625mm$ and $6.25mm$ did not vary substantially. The maximum difference between the plots was 2.4% and the average difference was $< 1\%$). The relative independence of the force plots to the mechanical grid point spacing meant that future simulations can be run with coarser grid point spacing, saving computational resource. The output of the simulation with a mechanical fibre grid point spacing of $6.25mm$ can be seen in detail in Figures 5.4. This figure also shows the A_2 concentration at the mechanical grid points as well as the muscle force vector.

It was expected that the force output would not vary substantially with an increase in the spacing of the mechanical grid points, as increasing the mechanical grid point spacing amounted to decreasing the sampling resolution of the physiological output of the $MURF$s. There were two possible ways

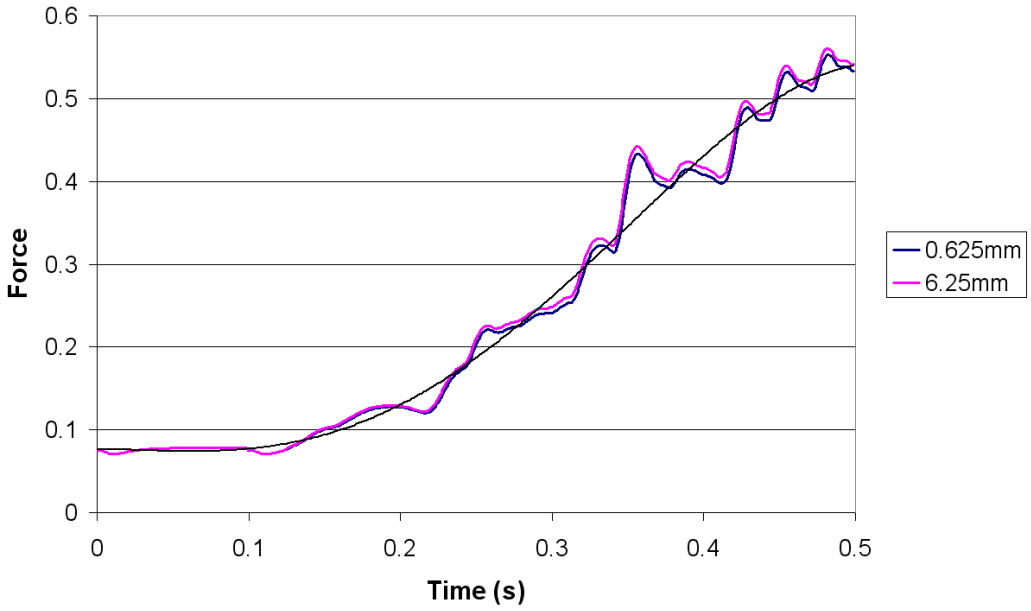

Fig. 5.2: The force output of linearly increasing $E(t)$ simulations of the Tibialis Anterior. In each case the distance between the Bidomain grid points was $0.0625mm$. Mechanical grid point spacing were either $0.625mm$ or $6.25mm$. Qualitatively the plots match each other identically and quantitatively, the average difference between the plots is $< 1\%$. The plots demonstrate that there is not a significant error added to the force output by increasing the mechanical grid point spacing. The polynomical best fit curve to the $0.625mm$ force output can be seen as the black curve.

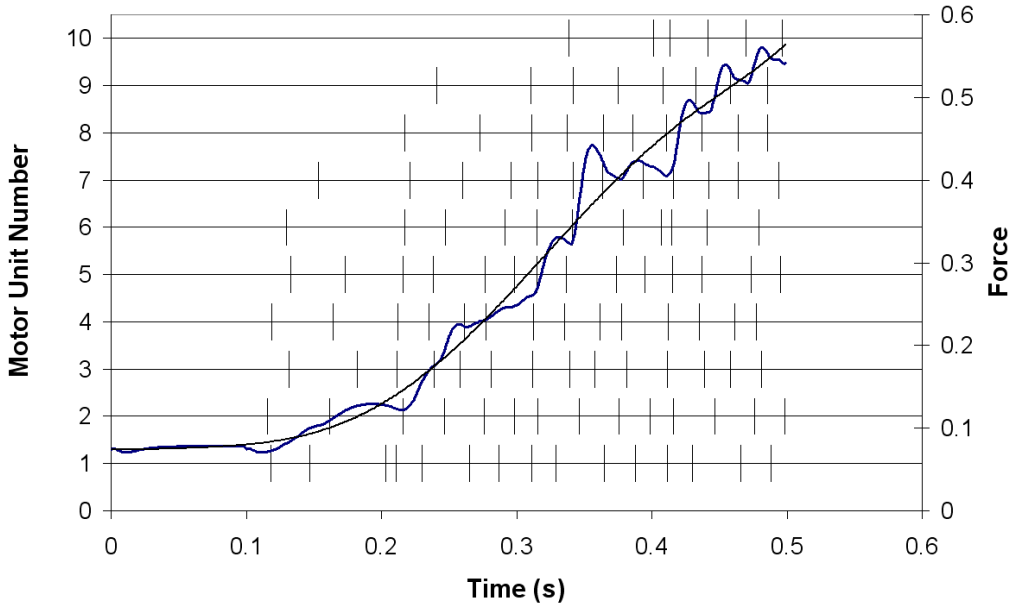

Fig. 5.3: The activation times of each motor unit in the 10 motor unit simulation is shown. Each vertical strike indicates the time when an Action Potential activated each $MURF$ fibre in the corresponding motor unit. The resulting force can be seen in the force trace with a sixth order polynomial curve fitted to it. Note the delayed onset of activation of the larger motor units, and the increase in average firing rate of all motor units as $E(t) \rightarrow 1$ (refer to Figure 5.1 for $E(t)$ plot).

that error could be introduced by decreasing the sampling resolution of A_1 and A_2. Firstly, the A_1 and A_2 waveforms (refer to Figures 3.3(a) and 3.3(b)) might not be able to be represented accurately at lower resolution levels, and secondly a decrease in the number of mechanical grid points surrounding the Gauss points could cause local fluctuations in the volume averages of A_1 and A_2. Neither of these two forms of error were thought to be substantial, as it was known from the output of the Bidomain fibre model (Section 4.1) that A_1 and A_2 could be represented with a much coarser grid and time discretisation than was required for the Action Potential, and the number of mechanical grid points was still much greater than the number of Gauss points.

5.2.2 Fibre Diameter

The mechanical fibre diameter (specified in the input file) determines the perpendicular distance between the mechanical fibres (refer to Section 4.2). Human skeletal muscle fibres have a diameter of approximately $80\mu m$ [70, 78, 106]. It was of interest to see the effect of increasing the input mechanical fibre diameter, and thus in effect representing a number of physiological fibres with one mechanical fibre. For example, an input mechanical fibre diameter of $1000\mu m$ would produce mechanical fibres which represented approximately 156 physiological fibres using the following relation,

$$RF = \frac{D_{mod}^2}{D_{phys}^2}, \tag{5.3}$$

where RF is the number physiological fibres of diameter D_{phys}, represented by the mechanical fibres of diameter, D_{mod}. This form of simplification greatly decreases the number of mechanical fibres, and thus mechanical grid points. As a result the computational effort is reduced, but this occurs at the expense of accuracy when defining the diffusive spread of fibre activation. However, the representation of a number of physiological fibres as one mechanical fibre should be valid as long as the total number of mechanical fibres is able to represent the smallest motor unit in a given motor unit distribution. This criterion was deemed to have been met if the number of mechanical fibres in the smallest motor unit was greater than 10. Ensuring that the smallest motor unit fibre number is 10 or more depends on the number of motor units,

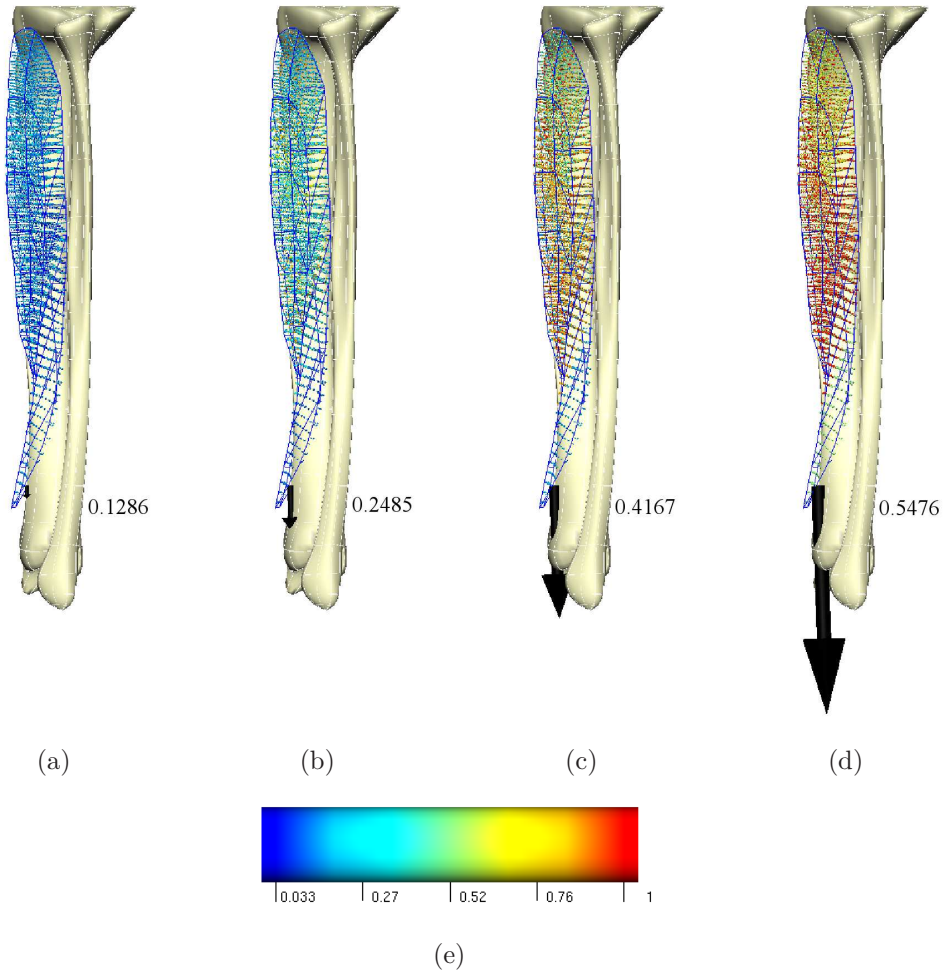

Fig. 5.4: The output of the simulated Tibialis Anterior with mechanical grid point spacing of 6.25mm and mechanical fibre diameter 2000μm. The muscle is shown in its anatomical location next to the tibia and fibula. The vector representing the negative of the sum of the reaction forces on the distal face of the muscle can be seen at the base of the muscle. Figures (a) - (d) show the normalised A_2 value at each mechanical grid point and the force vector at simulation time points 200, 300, 400, and 490ms respectively. The inhomogeneous A_2 values are a result of the different motor unit activation states and level of force can be seen to be correlated with the A_2 values. The force values shown are the same as those plotted as trace 6.25mm in Figure 5.2.

the motor unit fibre ratio, and the total number of mechanical fibres, all of which can be adjusted during model creation. The number of mechanical fibres compared to the mechanics Gauss points would also affect the force output, but given the relative size of the tri-quadratic elements and the minimum number of mechanical fibres required to accurately represent the fibre pool, the mechanical fibre to Gauss point ratio was not thought to be significant.

In order to determine the effect of changing the mechanical fibre diameter, three experiments were run using the following parameters:

- Mechanical grid point spacing: $6.25mm$
- Mechanical fibre diameter: $2000\mu m$, $1000\mu m$ and $500\mu m$
- Number of motor units: 10
- Motor unit fibre ratio: 10
- Percentage of slow type fibres: 70%
- Motor unit territory density: $0.01 fibres/mm^2$

All other input variables remained constant with the exception of the motor unit territory density. It was determined that the density was required to vary as a function of mechanical fibre diameter if the relative territory size between subsequent experiments was to remain constant. For this the following conversion equation was used.

$$\rho_{new} = \left(\sqrt{\rho_{old}} \cdot \frac{D^f_{old}}{D^f_{new}} \right)^2 , \tag{5.4}$$

where ρ_{new} and ρ_{old} are the motor unit territory densities of the new mechanical fibre spacing (D^f_{new}) and old mechanical fibre spacing (D^f_{old}) respectively. Thus for the three simulations the mechanical fibre diameters and motor unit territory spacing were as shown in Table 5.1. The output of these three simulations can be seen in Figure 5.5.

From Table 5.2 it can be seen that the total force increased with decreasing mechanical fibre diameter, i.e. force increase with an increase in the number of mechanical fibres. The increase in force magnitude with a reduction in

Table 5.1: The different values of mechanical fibre diameter and MUT density used in the mechanical fibre diameter calculations. The MUT densities were calculated using Equation 5.4.

Mechanical fibre diameter $D^f(\mu m)$	MUT density $\rho(fibres/mm^2)$
2000	0.01
1000	0.04
500	0.16

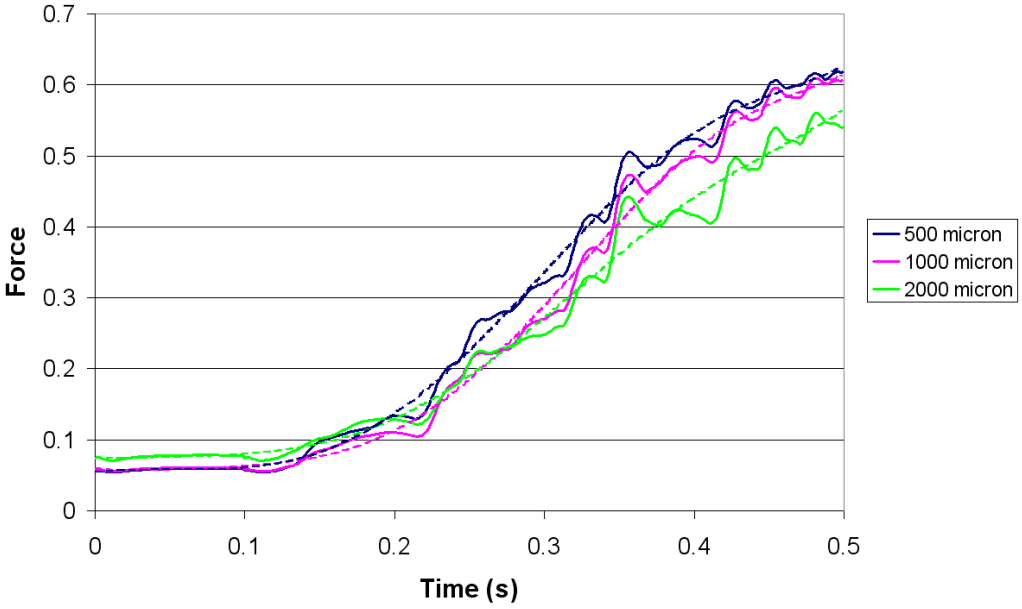

Fig. 5.5: The force output of a Tibialis Anterior muscle simulation with mechanical fibre spacings of $2000\mu m$, $1000\mu m$, and $500\mu m$. The $6th$ order polynomial best fit curves for each trace can be seen as dashed lines. The different initial force values are a result of the different location of fibre types throughout the three different muscles. The fast type fibres, as a result of the normalisation of A_1 and A_2, produce a higher resting tension. If there are more fast type mechanical fibres in areas with lower pennation angles, then a higher resting force will occur.

Table 5.2: The force output and total number of mechanical fibres for simulations with varying mechanical fibre diameter.

Fibre diameter $D^f(\mu m)$	Number of Fibres	Force Magnitude
2000	903	0.553
1000	3565	0.609
500	14577	0.618

mechanical fibre diameter is most likely due an increased likelihood of active fibres being located near the distal end of the muscle. From Figure 4.6 it can be seen that the distal end of the Tibialis Anterior mesh is of a smaller cross-section, and from Figure 4.12 it can be seen that the pennation angle of the fibres at the distal end of the muscle is lower than in other areas. As a result of these geometrical features, a decrease in mechanical fibre diameter will result in a larger relative increase in the number of mechanical fibres in the distal section of the muscle, which means that the probability of mechanical fibres in the distal area of the muscle becoming active earlier in the simulation will also increase. As muscle force, especially in slow twitch muscle fibres, does not sum linearly over time, the earlier a muscle fibre is activated, the higher its force will be at the end of the simulation (given current simulation times). The distally located fibres have a lower pennation angle and thus contribute more to the overall force output of the muscle (their force vectors more closely align with the total muscle force vector) and so a decrease in overall mechanical fibre diameter will lead to a higher total muscle force. As mechanical fibre diameters become even lower the increase in force becomes less pronounced as the relative change in distally located mechanical fibre numbers decreases.

From Figure 5.5 we can also see that the force profile became smoother as the number of mechanical fibres was increased. The measure of smoothness used was the R^2 value of the best fit 6th order polynomial, which is a measure of goodness of fit. For mechanical fibre spacings $2000\mu m$, $1000\mu m$, and $500\mu m$, the R^2 values were, 0.9884, 0.9950, and 0.9958 respectively. The smoothing of the force profile is expected with a decrease in mechanical fibre diameter, because the resulting increase in the number of mechanical fibres results in a more uniform muscle force distribution.

5.2.3 Number of Motor Units

The Tibialis Anterior in humans is thought to have 150 ± 43 motor units [76]. Representing the Tibialis Anterior with fewer than the actual number of motor units has similar benefits and drawbacks as reducing the number of represented fibres. Fewer motor units means that fewer $MURF$s need to be solved, and consequently fewer input files are required to be read in as input to the mechanics simulations. However, it is possible that the force output of

the muscle with fewer motor units is less smooth than it would otherwise be. To test the effect of a variation in motor unit numbers, simulations with the following parameters were run.

- Mechanical grid point spacing: $6.25mm$
- Mechanical fibre diameter: $2000\mu m$
- Number of motor units: 10, 30, 50
- Motor unit fibre ratio: 10
- Percentage of slow type fibres: 70%
- Motor unit territory density: $0.01 fibres/mm^2$

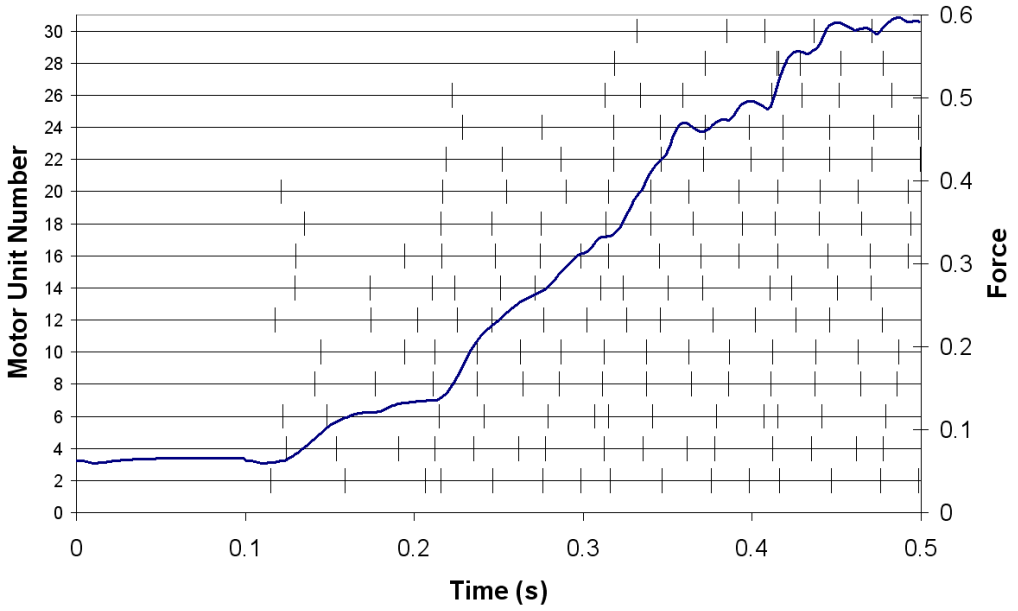

Fig. 5.6: The force output profiles of the Tibialis Anterior with 30 motor units. The stimulation times of every second motor unit are shown with vertical strikes. Similarly to Figure 5.3 it can be seen that the larger motor units become active later in the simulation and the average frequency of all motor units increases throughout the simulation. The sigmoidal shape of the force curve can be seen, with a slow average change in curvature at the beginning and end of the simulation and a relatively linear section in the middle.

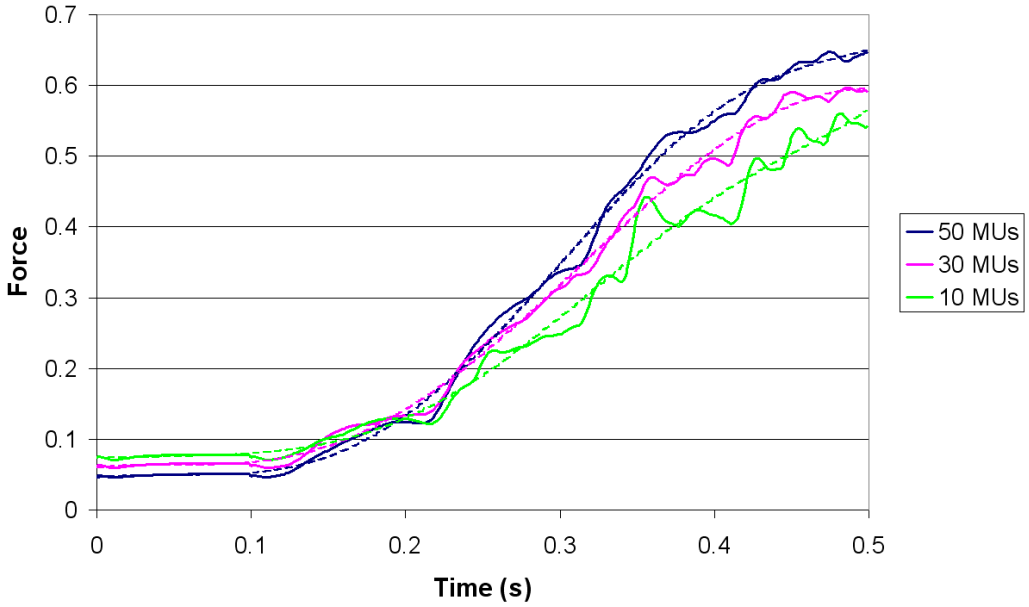

Fig. 5.7: The force output profiles of the Tibialis Anterior with 10, 30 and 50 motor units. The sigmoidal shapes of the force profile can be clearly seen in the best fit curves of the plots of 30 motor units and 50 motor units (dashed lines). The change in curvature of the 10 motor unit simulation is more subtle. The variations in the base line force of the simulations are due to the changing location of the slow and fast fibre types. Increasing the number of motor units increases the maximum value of the force, which is also a result of fibre type location.

The output of these simulations can be seen in Figures 5.6, and 5.7. The excitatory input to the motor unit pool was the same in each case (refer Figure 5.1). The force output becomes smoother as more motor units are added and the maximum force increases. The number of fibres in the muscle remained constant over the different simulations. As the number of motor units was increased from 10, to 30, to 50, the total muscle force output increased. The reason for this force increase is that with a greater number of motor units, the likelihood of distally located fibres being activated earlier in the simulation increases. Early activation allows the fibres to obtain a higher total force by the end of the simulation, and their distal location means that their pennation angle is less and thus their effect on total force is greater.

The smoothness of the force profile also increased as the number of motor units was increased. The measure of smoothness used was the R^2 value of the best fit 6th order polynomial, which is a measure of goodness of fit. For the 10, 30, and 50 motor unit muscles the R^2 values were, 0.9884, 0.9967, and 0.9972 respectively. From the R^2 values it can be seen that all three simulations were very accurately represented by the sigmoidal shaped 6th order polynomial, as an R^2 value of 1 would be a perfect fit, with the deviation from the best fit curve decreasing as the number of motor units was increased. An increase in the number of motor units, given the same number of total mechanical fibres, leads to a reduction in the average number of mechanical fibres per motor unit and a more independent activation pattern of mechanical fibres. The force fluctuation due to the addition of another motor unit to the active pool is therefore reduced and the smoothness of the force profile is increased.

The reason for the different starting force values of the three simulations is due to the relative location of slow and fast fibres within the muscle. The difference in initial conditions caused by the normalisation of A_1 and A_2 means that the local stiffness of the muscle can be altered depending on the location of fast and slow twitch fibres. The differences in the A_1 and A_2 values can cause local distortions in the stress field, and these distortions may be amplified depending on the location of the distortions. For example if a localisation of low stress occurred in the smaller diameter distal section of the muscle, compared to a more homogenous mix of stress, the total force output might be reduced as the fibre angles in this area have a smaller pennation angle and

thus have a greater relative contribution to the overall muscle force.

5.3 Whole Muscle Simulations

In this section a number of simulations are run which aim to demonstrate the ability of the modelling framework to replicate the effect of changing a number of muscle properties. The simulations use a mechanical fibre diameter of $2000\mu m$, a mechanical grid point spacing of $6.25mm$, and a Bidomain grid point spacing of $0.0625\mu m$. The simulations performed include models of changes in fibre type proportion, alterations to the location of fibre types, changes in Motor Unit Territory density, the effect of a constant excitatory drive, and the effect of different FES protocols on normal muscle and muscle that has undergone chronic FES.

5.3.1 The Tibialis Anterior Composed of a Single Fibre Type

The average proportion of fast and slow type fibres in the human Tibialis Anterior is 30% and 70% respectively. These proportions result in force output profiles as seen in the previous experiments. The effect of modifying the proportions was investigated by generating a Tibialis Anterior composed of 100% fast type fibres and another composed of 100% slow type fibres. The output of these three muscle types can be seen in Figure 5.8.

The difference in the initial forces of the muscles is a result of the normalisation of the fast and slow A_1 and A_2 values. The differences in the final forces of the muscles is due to the fatiguing of the fast fibres, meaning that as a whole the muscle is unable to produce as much force given this stimulation protocol. The fast muscle also produces a much more variable force plot for two reasons. Firstly, the faster fibres react more quickly than the slow fibres and so the discreteness of the Action Potential stimulations is more preserved. Secondly, because the fast fibres react so quickly, the step shape of the $E(t)$ function can be seen in the fast output. The output of the normal composition Tibialis Anterior can be seen to be the weighted sum of the fast and slow type components, with an initial value located between the two extremes, a profile

that more closely follows the 100% slow type muscle (as it is 70% slow) and a drop of in force a the end of the simulation as the late recruited fast type motor units fatigue.

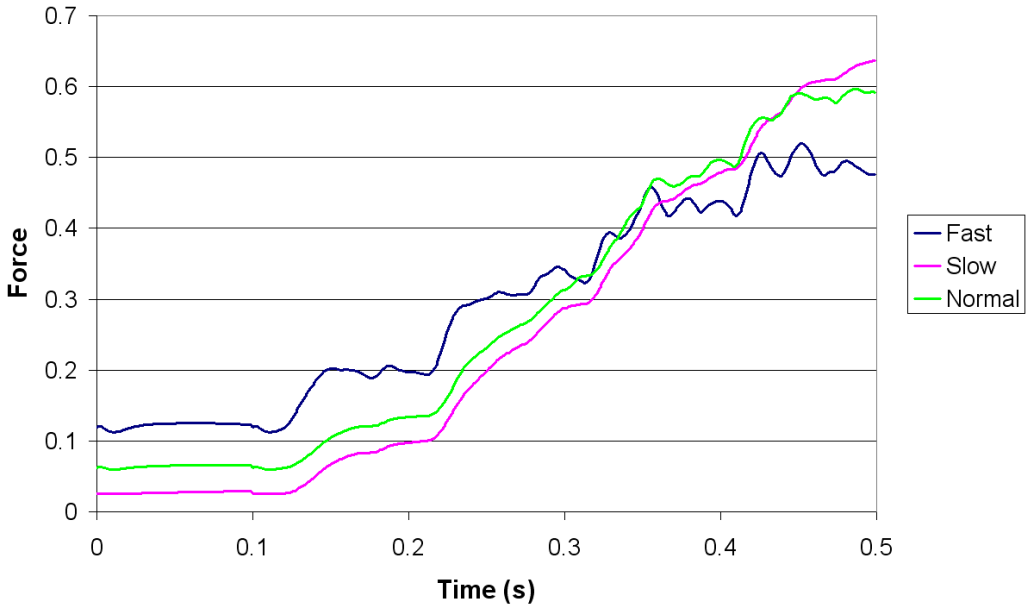

Fig. 5.8: The force profiles of a Tibialis Anterior muscle which is composed of 100% fast type fibres, 100% slow type fibres, and normal composition ratios. The greater final force output of the slow type muscle is a result of fatigue of the fast fibres, while the different force starting points arise from the normalisation of the A_1 and A_2 values for fast and slow type muscle fibres. The faster kinetics of the fast twitch muscle fibres can be seen by the increased variability of the fast twitch plot compared to the slow twitch plot. It can be seen that the normal Tibialis Anterior force profile arises as a weighted combination of the fast and slow twitch plots.

5.3.2 Different Fibre Type Weighting

It has been shown that the distribution of fibre types throughout the volume of the human Tibialis Anterior is not uniform [54]. The following experiments investigated the effects of modifying the location of muscle fibre types through the muscle. Three difference cases were selected, slow fibres weighted proximally, slow fibres weighted distally, and no weighting on fibre location. The results can be seen in Figure 5.9.

Very little difference can be seen between the muscle with slow type fibres

weighted to be proximal and the muscle with no weighting specified. The muscle with the slow type fibres weighted distally does show some increased force output compared to the other two. The increase in force of the distally weighted muscle is a result of the slow fibres being predominantly located in the area of low pennation angle. The fibres with a low pennation angle will have a disproportional effect on muscle force as they are generating force in an axis closer to that of the whole muscle axis. The slow type fibres generate more force than the fast fibres as they do not fatigue as fast, as evidenced by Figure 5.8. Further evidence for this being the reason for the difference in force comes from the fact that in Figure 5.9, the Distal line does not significantly diverge from the other to force outputs until halfway through the simulation, as the fast motor units in the other two plots are beginning to fatigue.

5.3.3 Motor Unit Density

Within human skeletal muscle the average physiological fibre diameter is approximately $80\mu m$ [70, 78, 106], and the Motor Unit Territory density ranges between $10 \leftrightarrow 30 fibres/mm^2$ [101, 117]. It was of interest to determine what effect, if any, the changing of Motor Unit Territory densities on muscle force output. The generated muscles used for these simulations all had mechanical fibre diameters of $2000\mu m$, thus each mechanical fibre represented 625 physiological fibres. Input densities of 0.1, 0.01, and $0.001 fibres/mm^2$ were used, representing real densities of 62.5, 6.25, and $0.625 fibres/mm$ respectively. The force profiles for each of these muscles can be seen in Figure 5.10.

There is no definite trend in the force profiles, the total force does not increase or decrease with decreasing density. The very small differences between the force profiles is a result of the variable location of muscle fibres. This is an interesting result because it was expected that by increasing the density of the motor unit territories a decrease in the total force would be observed along with a more variable force plot, as more discrete areas of the muscle would become active compared to a low density muscle, where it would tend to contract in a more homogenous manner. This points to a limitation in the mechanical implementation of the model. It is likely that the volume averaging of the A_1 and A_2 values causes a more homogeneous stress field than would be expected if the densities of the motor unit territories were increased in real

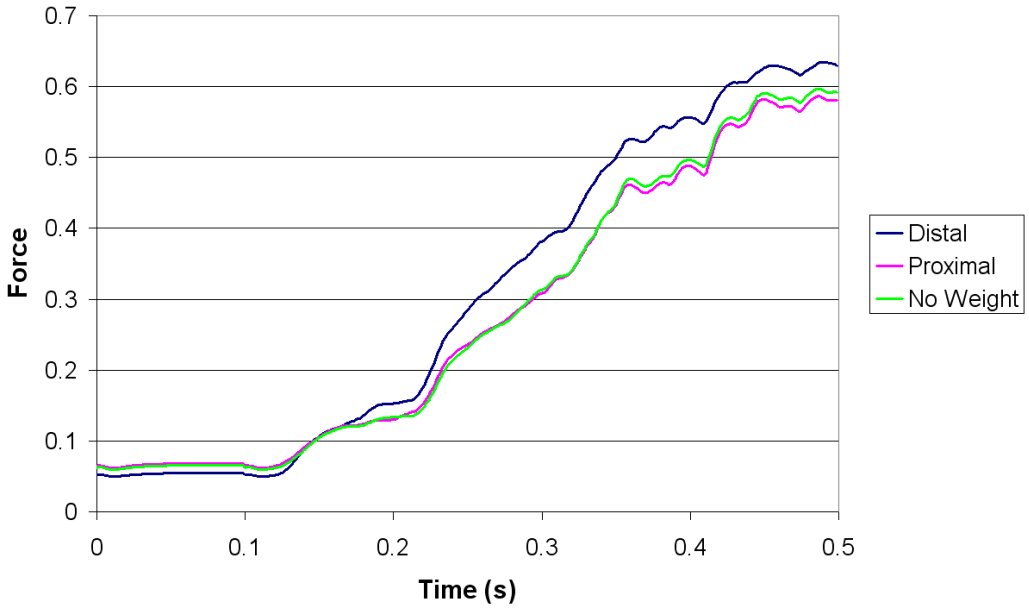

Fig. 5.9: Force output of the Tibialis Anterior with different weightings on the slow type fibres. Output is presented for three weighting cases, firstly, a weighting of 100% of the slow fibres to be at the distal end of the muscle, secondly, 100% of the slow fibres weighted to be at the proximal end of the muscle. In both of these cases, a weighting function of $WTFN = 1$ is used. The final case is no weighting on any of the fibres, so the location of all motor units is random. The differences in force output between the distal weighted muscle and the other two simulations is due to the slow type fibres, which ultimately produce more force (as a result of fatigue resistance, refer Figure 5.8), being located in the section of muscle where the fibres have lower pennation angles, resulting in a greater contribution to the force output of the muscle.

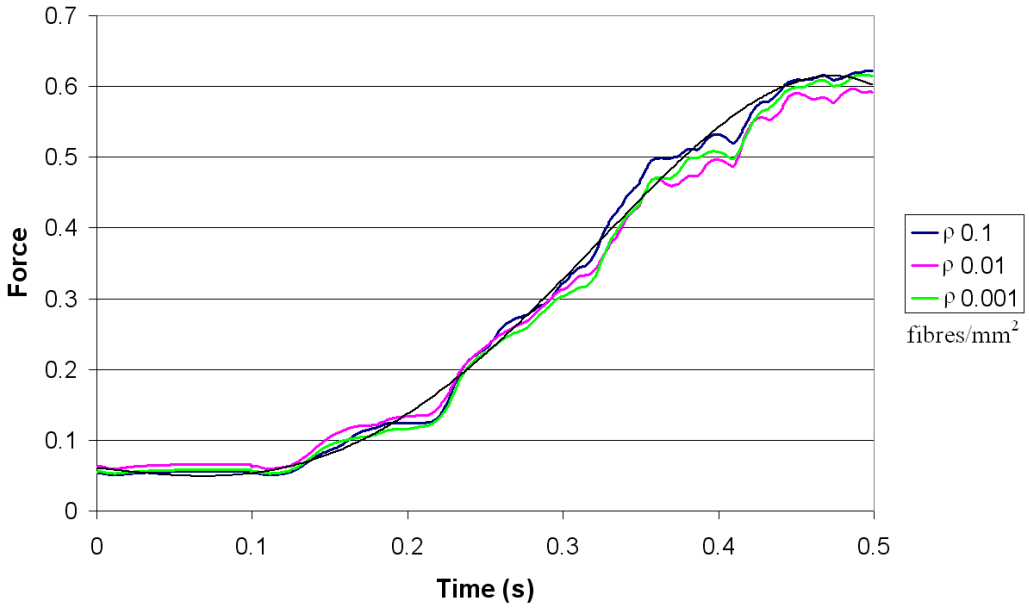

Fig. 5.10: The force output of Tibialis Anterior muscles with different Motor Unit Territory densities are shown. The densities range between 0.1 and $0.001 fibres/mm^2$ with mechanical muscle fibre diameters of $2000\mu m$. As can be seen there is no visible trend related to changing the density of the Motor Unit Territories, and the difference between the three plots is due to random fibre location differences in the three different muscles.

muscle tissue. This is one of the limitations of the constitutive law being used. For further discussion refer to Chapter 6.

5.3.4 Constant Excitatory Drive

The following experiment involved taking the Tibialis Anterior composed of 50 motor units, a normal fibre composition and activating it with a recruitment threshold of excitation (RTE) of 0.8 (i.e. for this experiment, the linearly increasing $E(t)$ function was not used). The output of this can be seen in Figure 5.11. This experiment partially simulates a force hold experiment, except no mechanical feedback is present, and so the input cannot be adjusted as force begins to drop off as the activated muscle fibres fatigue.

The very fast rise in the force profile can be seen at the onset of activation. The peak is followed by a gradual drop in the force of the muscle as some of the motor units begin to fatigue. The reduction of the fluctuations in the force trace over time are indicative of fatiguing of the larger fast type motor units. If this simulation was continued, a further gradual drop in muscle force would be observed.

5.3.5 Inverse Recruitment

Functional Electrical Stimulation causes an inversion of the normal recruitment order as larger diameter motor neurons are actived prefferentially to smaller ones (refer to Section 2.11). Function Electrical Stimulation imposes the applied stimulation train onto the activated motor units. The results of the stimulation of the Tibialis Anterior with different frequencies of stimulation can be seen in Figure 5.12. For this, the $E(t)$ input is the same as the physiologically recruited simulations. The delay in onset of muscle activation at the beginning of the simulation is due to the fact that all motor units in this particular muscle are active below $E = 0.75$ from (4.17). Thus during inverse recruitment, $E(t)$ must drop below 0.75, which occurs at $0.2s$, for motor units to fire. The synchronisation of stimulation causes regular pulses in the force profiles, which decrease the smoothness of the force output. The smoothness of the force profile increases as the stimulation frequency increases, i.e. as the muscle moves more toward a tetanus. Increasing the simulation frequency not

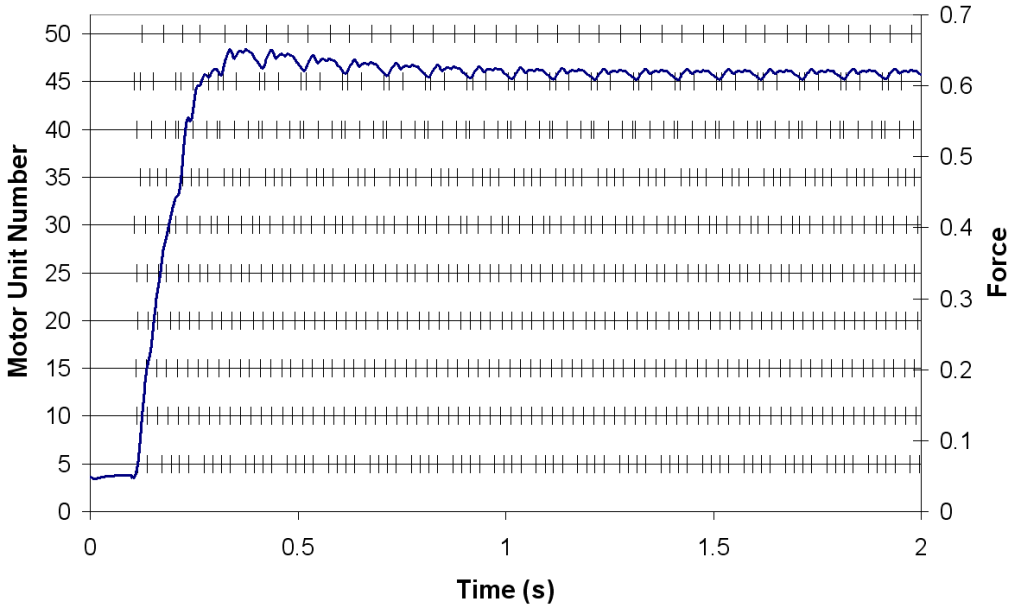

Fig. 5.11: The force output of the Tibialis Anterior with 50 motor units with an RTE value of 0.8. The rapid rise in force can be seen as the motor units are recruited and the force drop off can be seen as the fast twitch motor units begin to fatigue. The reduced magnitude of the fluctuations in the force trace after 1s further indicate the fatiguing of the larger motor units. The activation times of every fifth motor unit can be seen as vertical strikes. It can be seen that the randomness generated to replicate physiological firing conditions is less evident at this time resolution, and repetitiveness can be seen in the action potential trains.

only increases the smoothness of the force profiles but also increases the rate of force production as the force summation effects become more prominent. In the 20 to $40Hz$ simulations a distinct change in gradient can be seen at about $0.3s$. The change in gradient results from predominantly fast type fibres being activated and fatiguing slightly, before slow type motor units are added to the active pool which do not fatigue as easily.

Stimulating a muscle using FES over a long period of time induces compositional changes in the muscle [91]. The muscle tends to move toward a slower [74] and a more fatigue resistant [1] overall muscle composition. Figure 5.13 shows exactly the same protocol as Figure 5.12, however the composition of the muscle has changed from 70% slow type fibres to 95% slow type fibres, representing the change in fibre type composition that could be expected in a muscle that has undergone chronic FES. The force profile for each frequency is smoothed somewhat as a result of the slower kinetics of the predominantly slow type fibres.

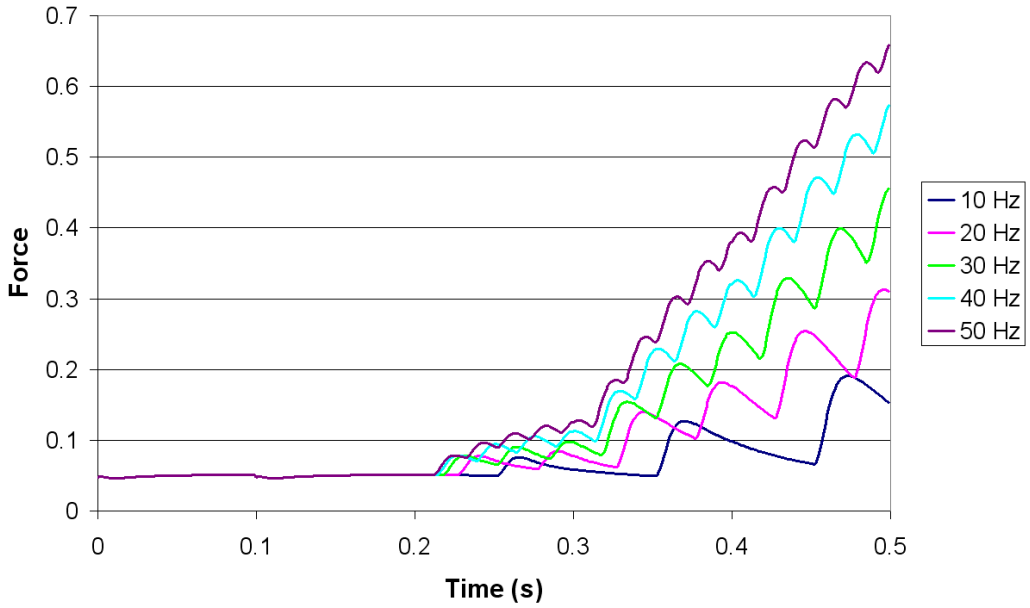

Fig. 5.12: The force profiles of a Tibialis Anterior of normal fibre type composition undergoing Functional Electrical Stimulation at different driving frequencies. The synchronisation of the stimulation results in a pulsitile force response. The smoothness of the force output increases as the stimulation frequency increases as the muscle is moving closer to tetanus.

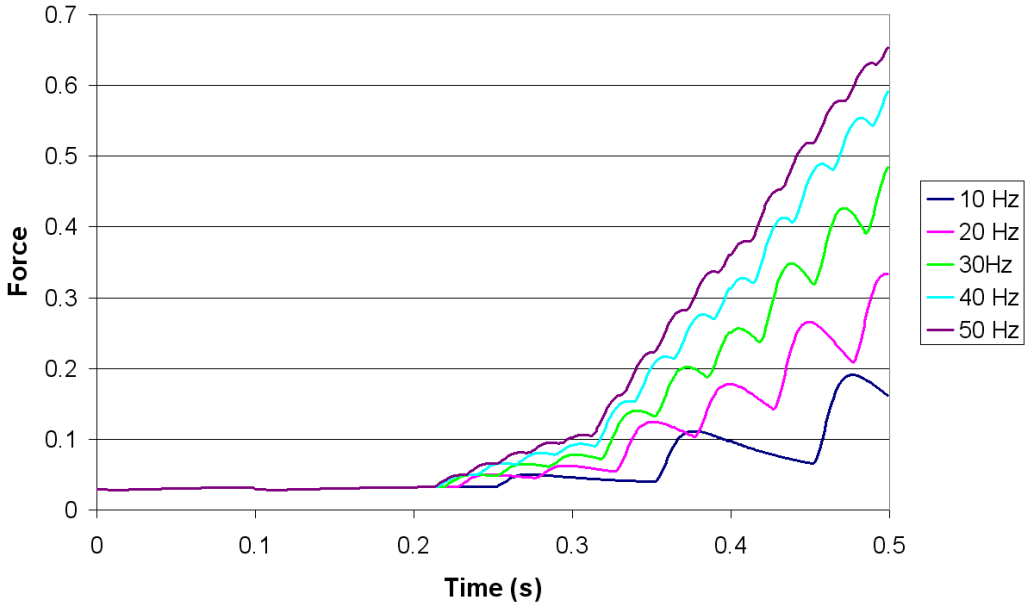

Fig. 5.13: The force profiles of a Tibialis Anterior of a predominantly slow fibre type composition (95%) undergoing Functional Electrical Stimulation at different driving frequencies. The force output profiles are similar to those of the normal Tibialis Anterior except the smoothness of the plots is increased and the curvature is slightly increased.

Table 5.3: The inverse protocol used to replicate normal physiological behaviour

Time step (s)	$E(t)$ value	Frequency (Hz)
$0 - 0.1$	0	0
$0.1 - 0.2$	0.5	50
$0.2 - 0.3$	0.75	50
$0.3 - 0.4$	1	40
$0.4 - 0.5$	1	40

5.4 Design of an Inverse Recruitment Protocol to Match Physiological Recruitment

The usefulness of Functional Electrical Stimulation may be enhanced if the protocol used is able to match normal physiological behaviour as closely as possible. A more natural force profile means that the upper and lower limits and rates of change of force are implicitly the same as normally recruited muscle. As muscle composition changes over time with chronic use of FES, it was of interest to determine the robustness of protocols to the change in muscle fibre composition. To achieve this, a protocol was designed to replicate as closely as possible the physiological output of a Tibialis Anterior muscle of normal fibre composition. Following this a second muscle was created with a fibre composition of 95% slow type fibres and the previous FES protocol was used to activate it.

Figure 5.14 shows the best fit curves of the force profile plot of the physiologically recruited muscle (PR) and the best fit curves for the force plots resulting from the inverse recruitment of the same muscle at frequencies between $10Hz$ and $50Hz$. Horizontal lines have been added to the figure to indicate the force levels obtained by the normal muscle at $0.1s$ intervals.

Using these force levels it is theoretically possible to build this normal force profile out of the inversely recruited profiles. Figure 5.15 gives the same information for the slower composition muscle. Using Figure 5.14 the stimulation protocol displayed in Table 5.3 was devised. This inverse stimulation protocol primarily uses high frequency stimulation as a close fit to the physiological profile was desired and it was thought that high frequency stimulation would mean a smoother force output and thus a better fit. The output from this

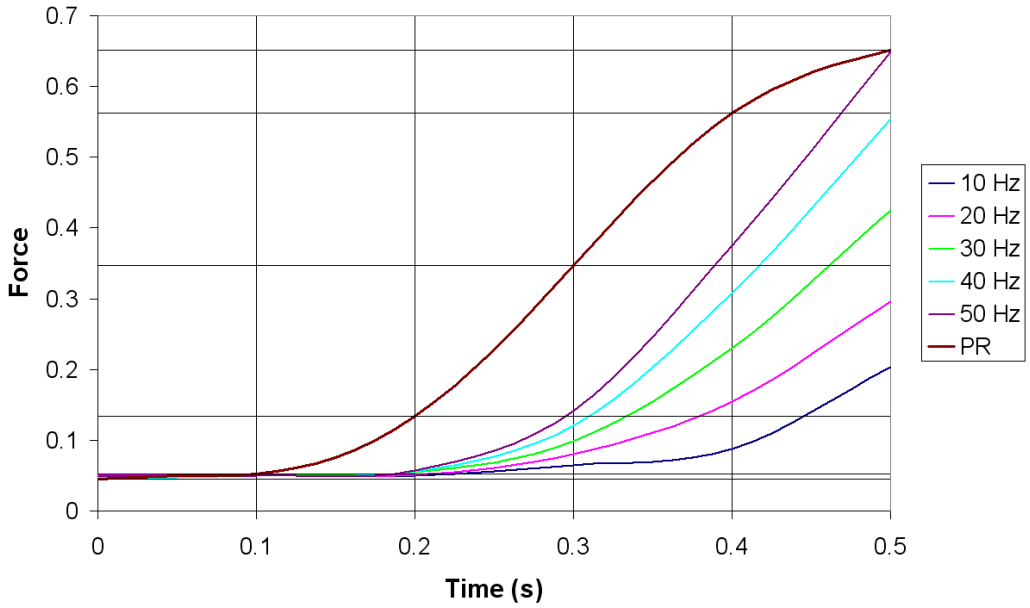

Fig. 5.14: The plots on this graph are all 6th order best fit approximations of the original functions. Each simulation was run with 50 motor units. The normal physiological recruitment (PR) curve can be seen as well as the curves for the inverse recruitment of the same muscle at five different driving frequencies.

inverse simulation with a normal fibre composition can be seen as trace *Inv. Norm.* in Figure 5.16 and compared to the normal physiological force profile in a muscle of normal composition which is trace *Phys. Norm.* in the same Figure. The same simulation protocol was then applied to the slower muscle (95% slow type) to see if the change in muscle composition as a result of chronic FES would alter the force profile of the muscle (trace *Inv. Slow* in Figure 5.16).

From Figures 5.12 and 5.13 it is apparent that there are many ways in which the physiological force profile could be reconstructed from the inverse protocols. To demonstrate this, another inverse protocol was created. This protocol can be seen in Table 5.4. This inverse stimulation protocol uses lower frequency stimulations, and higher $E(t)$ values at the beginning of the simulation. The force output of a normal composition Tibialis Anterior using this new profile can be seen as trace *Inv. New* in Figure 5.16. It can be seen that the force profile is less smooth at the beginning of the simulation however the force profile still matches the shape of the physiologically recruited muscle

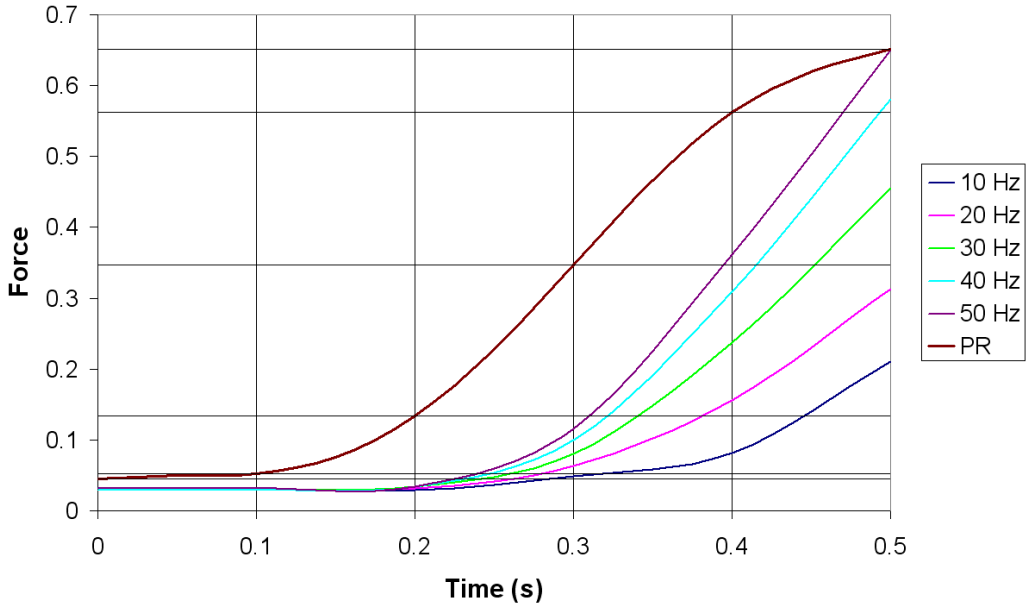

Fig. 5.15: The best fit curve for the force of the physiologically recruited (PR) muscle is shown along with the best fit curves for the inverse stimulation of the same muscle. The muscle in question is composed of 95% slow type muscle fibres but is otherwise the same as the muscle depicted in Figure 5.14.

Table 5.4: An inverse protocol to replicate normal physiological behavior using lower frequency stimulation

Time step (s)	$E(t)$ value	Frequency (Hz)
$0 - 0.1$	0	0
$0.1 - 0.2$	0.75	20
$0.2 - 0.3$	0.1	30
$0.3 - 0.4$	1	40
$0.4 - 0.5$	1	40

well. The best fit curves using sixth order polynomials for the three inverse simulations and the physiological force profile can be seen in Figure 5.17.

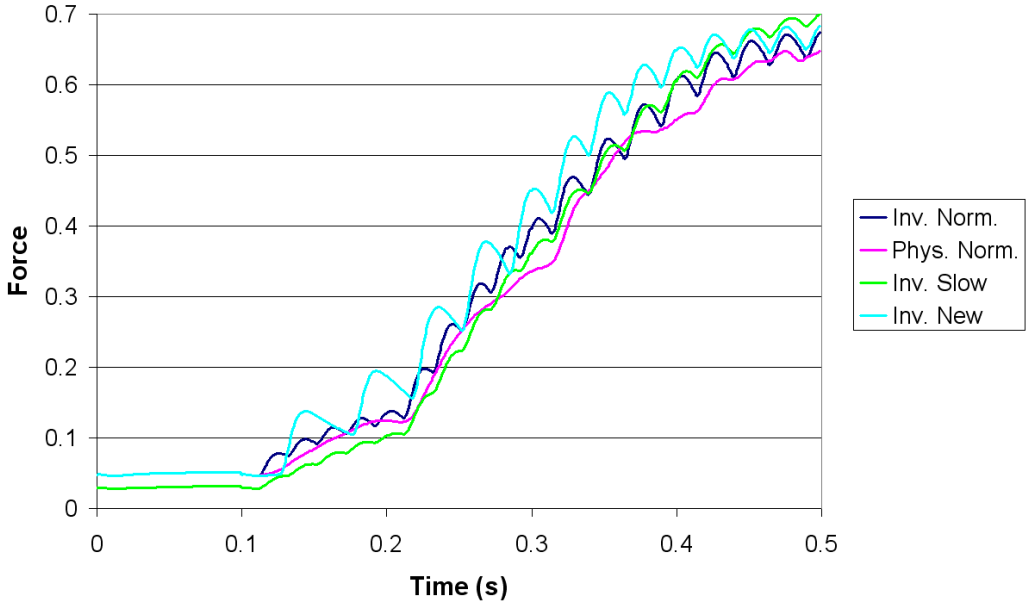

Fig. 5.16: The normal physiological force output of a Tibialis anterior (Phys. Norm.) is shown along with force profiles of Tibialis Anteriors of different fibre compositions (normal or slow) under the influence of different FES protocols. The inverse protocol used in both cases is given in Table 5.3. The first force plot shows the output of a Tibialis Anterior of normal fibre composition (i.e. 70% slow 30% fast) (Inv. Norm.). The second is the output of a Tibialis Anterior composed of 95% slow type muscle fibres (Inv. Slow). As can be seen the inverse protocols qualitatively match the physiological force profile well in that the changes in curvature are similar in magnitude and location and the absolute force values are also the same (more clearly seen in Figure 5.17). The root mean square of the difference between the physiological trace and the inverse traces are as follows, 0.027, 0.029, and 0.056 for *Inv. Norm.*, *Inv. Slow*, and *Inv. New* respectively.

The three inverse protocols were able to qualitatively match the normal physiological output of the Tibialis Anterior well. To try and quantify the difference between the force traces the RMS difference was used.

$$RMS_{diff} = \sqrt{\frac{\sum_{t=1}^{N} \left(Y_1^t - Y_2^t\right)^2}{N}}, \tag{5.5}$$

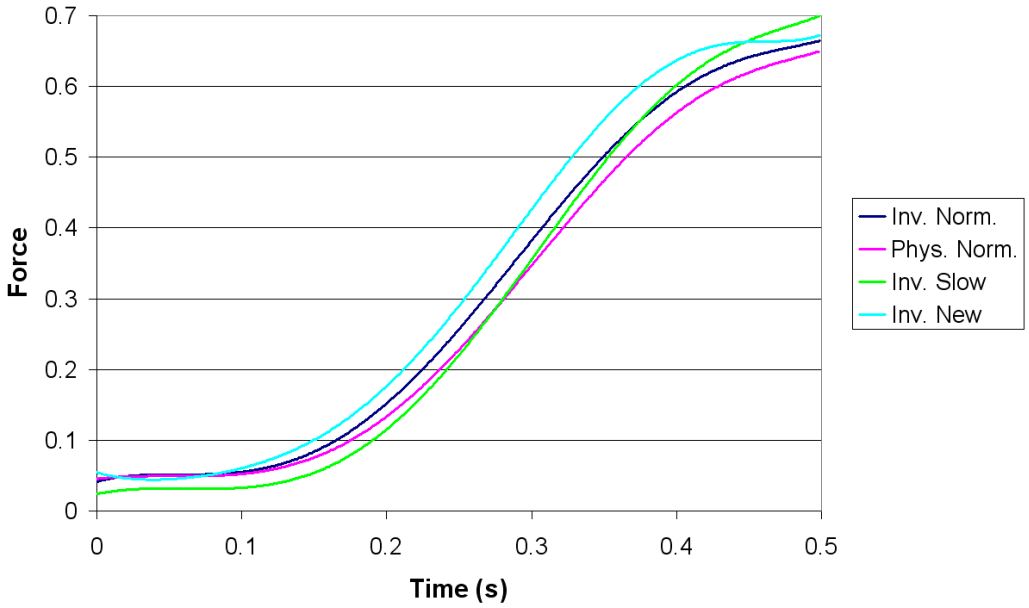

Fig. 5.17: The sixth order polynomial best fit curves of the force profiles in Figure 5.16. The inverse protocols match the shape of the physiological data well, with the Inv. Norm. fit giving the closest representation (RMS error 0.023, followed by the Inv. Slow fit (RMS error of 0.027) and then Inv. New (RMS error of 0.053).

where Y_1^t and Y_2^t are the force values of the two traces being compared at time t. The RMS difference can give an indication of which of the three inverse protocols most closely matched the physiological force trace. The RMS difference values for the force traces from the physiological data were 0.027, 0.029, and 0.056 for Inv. Norm., Inv. Slow, and Inv. New respectively. These RMS values show that the high frequency protocols were able to best match the physiological output, and that there was very little difference between the output of the normal composition, and the slower Tibialis Anterior. The lower frequency inverse protocol matched the physiological output least well because of the large fluctuations in the force as a result of the low frequency, synchronous stimulation. While this protocol did not match the physiological force as well as the other protocols, it may provide an advantage in reducing the over all fatigue of the muscle.

Chapter 6

Discussion and Conclusions

6.1 Discussion

In this thesis a biophysically-based model of skeletal muscle function has been developed. The model aims to incorporate a high level of anatomical and physiological data so that the effects of any changes to the muscle on disparate spatial and temporal scales can be modelled. The framework that has been created has demonstrated the ability to represent the physiological activity of both fast and slow type skeletal muscle fibres, both at points in space and along the length of a muscle fibre. The model is also able to use this physiological data, along with information concerning the functional organisation of the muscle, to contract the muscle, giving qualitatively accurate force profiles.

The physiology of skeletal muscle is modelled in this framework using the Bidomain equations. The Bidomain equations are a continuum approximation to the current flow in a section of tissue, thus using these equations to represent the spread of electrical activity through the muscle fibre treats the fibre as a continuum, which may not be accurate. It is possible that the membrane channel densities or the ionic concentrations may vary systematically through the tissue in some way, although detailed information is not available to the best of the author's knowledge. It is therefore reasonable to use the Bidomain equation for the purpose of representing the electrical flow through the muscle fibre. The Bidomain equations have previously been applied in a similar manner on the motor nerves [63]. Given the use of the modelled fibre to represent more than one real muscle fibre (i.e. fibre diameters greater than physiological

diameters), then applicability of the continuum approximation increases.

The constitutive law that is used to couple the physiological output of the skeletal muscle fibre model to the mechanical contraction of the whole muscle represents a novel method of electromechanical coupling. While this method is theoretically sound, it has not yet been validated against specific experimental results, instead a qualitative validation process is implicit in the work outlined in Section 5. The framework does qualitatively replicate the output of other numerical and physiological studies. A full validation of the coupling method is in fact currently almost impossible as the data required to generate a fully accurate constitutive law does not exist. A large amount of experimental and modelling work needs to be undertaken to fill the gap in the literature regarding the three-dimensional mechanical properties of skeletal muscle tissue in both passive and active states. This work will almost definitely have to begin by looking at the microstructural linkages between muscle fibres and the rolle that the epimysium, perimysium, and endomysium plays in modifying both the force output of muscle fibres, and the path of the generated force through the muscle.

The effects of muscle fibre length changes were neglected in this work, and as a result all of the results presented were of skeletal muscle under isometric conditions. Although this simplification did allow for a more straight forward modelling process, a major reason that muscle length interactions was not included is because to the best of the author's knowledge, no cell models exist which include the length dependant response of intracellular or extracellular physiological species.

The activation of the muscle, via recruitment and rate coding, is an adaptation from previous work by Fuglevand *et.al.* [36] in the area of skeletal muscle modelling. This method has been shown in other studies to produce physiologically-realistic activation data. As a result, realistic force output was produced by incorporating the Fuglevand *et.al.* method of activation in this modelling framework. Further additions to the muscle control system are possible. A methodology for changing the recruitment and rate coding of different motor units as motor units start to fatigue is an area where more work is required. The framework presented in this thesis provides a platform for this sort of research as it includes the muscle control system and physiological represen-

tations of muscle output and fibre fatigue. Simulations aimed at investigating the changes in motor unit activity as a result of motor unit fatigue would need to be done in conjunction with experimental study.

The method used to couple the physiological output of the fibre models (A_1 and A_2) to the mechanics requires that the mechanical and physiological solutions were performed independently of each other. As there was no feedback from the mechanical solution to the physiological model itself, this did not pose a problem to the numerical accuracy of the solution. However, as the recruitment and rate coding information that was applied to the physiological simulations was calculated at the end of the previous mechanics step, each set of recruitment and rate coding information was constant for the duration of that particular solution step. In the simulations presented in Section 5 this time step was $100ms$, which is a reasonable step length if the physiological input is to be modulated over a simulation in the order of seconds. Also, as the duration of the A_1 and A_2 transients is of the order of $100ms$ [105], a time step of $100ms$, within which the control of the muscle can be modulated, seems appropriate. However, as higher stimulation frequencies can cause rapid force summation over time scales less than the $100ms$ used, an improvement in the implementation of the control of the muscle may be appropriate. This would especially true if the response of a muscle, where the input was being very quickly modulated between high and low excitation, was to be modelled.

The method used to represent the Functional Electrical Stimulation of the Tibialis Anterior in Section 5 is a simple, generalised, approximation to what would actually be occurring during the electrical activation of a real muscle. The quantitative value of electrical current or voltage that would be required to activate the Tibialis Anterior depends on the location of the electrode on the body surface, however the principles of the inverse recruitment resulting from this stimulation would be the same. In the future it may be beneficial to model the α-motor neurons and the applied electrical stimulus explicitly so that the Functional Electrical Stimulation protocol could be optimised along with electrode placement and stimulus intensity. Modelling these structures would also give a better insight into the factors that add variability to the inverse recruitment order and the results of the variability on force output, fatigue, and activation sequences.

The force output produced in Section 5, as a result of the modification of a number of intrinsic anatomical and physiological parameters, highlighted the importance of the structure of the muscle in determining the final force output. Throughout the simulations in Chapter 5 it was found that one of the primary determinants on the overall force response of the muscle was the location of the different fibre type through the muscle and the pennation angles associated with these muscle locations. The fact that the Shorten *et.al.* model required the A_1 and A_2 parameters to be normalised between the fast and slow types, and this normalisation resulted in fluctuations of the overall force of the muscle, the distinct differences between the fibre type representations served to highlight the effect of structure. The effect that the internal structure of the muscle plays on the overall behaviour of the muscle is likely to be increased as more information is incorporated concerning the force transduction pathways and the constitutive relations within the muscle.

The Functional Electrical Stimulation protocols designed in Section 5.4 are examples of the sort of output that this modelling framework can produce. In future, protocols could be matched to functional movements instead of a simple linear activation profile. The effect of muscle fatigue on repeated processes could also be taken into consideration, both to minimise fatigue, and to look for optimal changes to protocols once muscle fatigue occurs.

6.2 Conclusions

The skeletal muscle modelling framework detailed in this thesis uses detailed physiological and anatomical information to replicate the overall function of skeletal muscle. The models are built up from the Shorten *et.al.* cellular model which is able to represent the physiological functioning of both fast and slow type muscle. These cellular models are then applied to one-dimensional finite elements and solved using the Bidomain equations to replicate the physiological function of a muscle fibre. Using this method, the Action Potential waveform and velocity can be reproduced, and as a result of the information contained within the cell model, information on the state of the actin-myosin crossbridges can be extracted. The crossbridge information can then be used as input to a three-dimensional finite elasticity model of a skeletal muscle via novel

constitutive laws presented in [99]. The resulting finite elasticity model is solved over a three-dimensional finite element representation of the skeletal muscle in question. The three-dimensional mechanical simulation can produce the whole muscle force output as a result of a defined activation protocol. The activation protocol can represent the normal physiological recruitment pattern of skeletal muscle, or the inverse recruitment of muscle under the influence of Functional Electrical Stimulation. Intrinsic muscle parameters, such as motor unit density, motor unit number, fibre type proportion, fibre type location etc can be altered to determine the effect that these parameters have on total muscle output. The framework can be used to design inverse recruitment protocols that are able to follow the behaviour of skeletal muscle under normal physiological activation, as well as the ability to investigate the total muscle fatigue response to the protocols.

6.3 Future Work

The primary area where future work needs to be directed is the improvement of the skeletal muscle constitutive laws. Without a greater knowledge of the coupling of stress and strain in the complex transversly isotropic, or even orthotropic, material of skeletal muscle, all models will struggle to make quantitative predictions on muscle force output. The creation of these new constitutive laws will require a large amount of experimental research, as well as modelling work, to understand the nonlinear force summation and lateral force transduction seen in skeletal muscle. The mechanical studies will also need to determine the local and whole muscle effects that muscle fascicles produce. Without a more detailed mechanical description of the structure of skeletal muscle, future modelling work will be greatly restricted in its accuracy and predictive ability.

The modelling framework presented may be extended to incorporate a more rigorous description of the skeletal muscle control process. The changes in recruitment and rate coding behaviour as the muscle performs different types of contractions, or as individual motor units begin to fatigue poses an interesting and very complex control problem. Simulations involving multiple muscles and their articulation of a joint would be the next logical step in the skeletal muscle

modelling process. Modelling multiple muscles around a joint would also allow the investigation of another muscle control problem; how compartmentalised muscle control affects the force output vector of the muscle when performing different joint movements.

The use of the Bidomain equations to model the flow of electrical potential through the muscle fibre leads to the calculation of the extracellular potential of the fibre at all solution points. Using the extracellular potential of every fibre in the muscle along with a description of the electrical properties of the muscle and surrounding tissue, such as fat and skin, EMG simulations could be performed. The linking of this framework with an EMG output would have the following benefits. It could provide researchers with a better understanding of how to interpret EMG signals, or filter them so they are able to get the desired information from them, as the specific muscle structural, and control system influences on the EMG could be investigated. The physiological state of a patient's muscle, healthy or diseased, could be inferred with more accuracy, allowing the possible diagnosis of disorders such as muscular dystrophy earlier.

A more detailed investigation into the area of Functional Electrical Stimulation would also be possible with the integration of the nerve modelling work detailed in Kim *et.al.* [63]. Using similar methods to the EMG simulations, the electrical field provided by an electrode on the α-motor neurons of the muscle could be evaluated. This could lead to better electrode placements, in terms of efficacy of treatment and also design of the FES system itself. The FES activation modelling would also be linked in with the design of stimulation protocols that would illicit specific movement or force from the target muscle. The protocols could be optimised to minimise fatigue while replicating as closely as possible normal muscle movement.

There is also the potential for modifying the Shorten *et.al.* model so that the effect of different physiological agents, e.g. drugs, on both electrical and mechanical muscle performance could be assessed. The effect of a specific drug could by modelled by modulating the concentration or permeability of an ion or ion transporters, and the resulting effect on the whole muscle could be evaluated.

Bibliography

[1] J. L. Andersen, T. Mohr, F. Biering-Sorensen, H. Galbo, and M. Kjaer. Myosin heavy chain isoform transformation in single fibres from m. vastus lateralis in spinal cork injured individuals: effects of long-term functional electrical stimulation (fes). Eur. J. Physiol., 431:513–518, 1996.

[2] F. C. Anderson and M. G. Pandy. Dynamic optimization of human walking. J. Biomechanical Engrg., 123:381–390, 2001.

[3] S. Andreassen and L. Arendt-Nielsen. Muscle fibre conduction velocity in motor units of the human tibial muscle: a new size principle parameter. J. Physiol., 391:561–571, 1987.

[4] S. Aquilonius, H. Askmark, P. Gillberg, S. Nandedkar, Y. Olsson, and E. Stalberg. Topographical localization of motor endplates in cryosections of whole human muscles. Muscle & Nerve, 7:287–293, 1984.

[5] T. M. Austin, M. L. Trew, and A. J. Pullan. Solving the cardiac bidomain equations for discontinuous conductivities. IEEE Transactions on Biomedical Engineering, 53(7), July 2006.

[6] J. C. Barbenel. The mechanics of the temporomandibular joint. J. Oral Rehabil., 1:19–27, 1974.

[7] R.J. Barnard, V.R. Edgerton, T. Furukawa, and J.B. Peter. Histochemical, biochemical and contractile properties of red, white, and intermediate fibres. American Journal of Physiology, 220:410–414, 1971.

[8] S.M. Baylor and S. Hollingworth. Model of sarcomeric calcium movements, including atp calcium binding ad diffusion, during activation of frog skeletal muscle. Journal of General Physiology, 112:297–316, 1998.

[9] G.W. Beeler and H. Reuter. Reconstruction of the action potential of ventricular myocardial fibres. Journal of Physiology, 268:177–210, 1977.

[10] F. Bellemare, J. J. Woods, R. Johansson, and B. Bigland-Ritchie. Motor-unit discharge rates in maximal voluntary contractions of three human muscles. Journal of Neurophysiology, 50(6):1380–1392, 1983.

[11] N. Bhadra and P. H. Peckham. Peripheral nerve stimulation for restoration of motor function. J. Clin. Neurophysiol., 14(5):378–393, 1997.

[12] S.S. Blemker, P.M. Pinsky, and S.L. Delp. A 3d model of muscle reveals the causes of nonuniform strains in the biceps brachii. Journal of Biomechanics, 38:657–665, 2005.

[13] S. C. Bodine, A. Garfinkel, R. R. Roy, and V. R. Edgerton. Spatial distribution of motor unit fibers in the cat soleus and tibialis anterior muscles: local interactions. J. Neurosci., 8:2142–2152, 1988.

[14] S. Bodine-Fowler, A. Garfinkel, R.R. Roy, and V.R. Edgerton. Spatial distribution of muscle fibers within the territory of a motor unit. Muscle & Nerve, 13:1133–1145, 1990.

[15] H. Broman, C. J. De Luca, and B. Mambrito. Motor unit recruitment and firing rates interaction in the control of human muscles. Brain Research, 337:311–319, 1985.

[16] S. H. Bryant. Cable properties of external intercostal muscle fibres from myotinic and nonmyotonic goats. J. Physiol, 204:539–550, 1969.

[17] R.E. Burke, D.N. Levine, M. Salcman, and P. Tsairis. Motor units in cat soleus muscle: physiological, histochemical and morphological characteristics. Journal of Physiology, 238:503–514, 1974.

[18] M.B. Cannell and D.G. Allen. Model of calcium movements during activation in the sarcomere of frog skeletal muscle. Biophysical Journal, 45:913–925, 1984.

[19] H. P. Clamann. Motor unit recruitment and the gradation of muscle force. Phys. Ther., 73:830–843, 1993.

[20] A. K. Datta and J. A. Stephens. Synchronization of motor unit activity during voluntary contraction in man. Journal of Physiology, 422:397–419, 1990.

[21] C. J. De Luca, R. S. LeFever, M. P. McCue, and A. P. Xenakis. Behaviour of human motor units in different muscles during linearly varying contractions. J. Physiol. Lond., 329:113–128, 1982.

[22] C. J. De Luca, R. S. LeFever, M. P. McCue, and A. P. Xenakis. Control scheme governing concurrently active human motor units during voluntary contractions. J. Physiol., 329:129–142, 1982.

[23] M. de Zee, M. Dalstra, P. M. Cattaneo, J. Rasmussen, P. Svensson, and B. Melsen. Validation of a musculo-skeletal model of the mandible and its application to mandibular destruction osteogenesis. Journal of Biomechanics, 2006.

[24] M. de Zee, L. Hansen, C. Wong, J. Rasmussen, and E. B. Simonsen. A generic detailed rigid-body lumbar spine model. Journal of Biomechanics, 2006.

[25] A. Del Valle and C. K. Thomas. Firing rates of motor units during strong dynamic contractions. Muscle & Nerve, 32:316–325, 2005.

[26] A. D. V. Do and C. K. Thomas. Firing rates of motor units during strong dynamic contractions. Muscle & Nerve, 32:316–325, 2005.

[27] S.J. Dorgan and J.O. O'Malley. A mathematical model for skeletal muscle activated by n-let pulse train. IEEE transaction on rehabilitation engineering, 6:286–299, 1998.

[28] J. Duchateau, J.G. Semmler, and R.M. Enoka. Training adaptations in the behaviour of human motor units. Journal of Applied Physiology, 101:1766–1775, 2006.

[29] R. M. Enoka. Activation order of motor axons in electrically evoked contractions. Muscle & Nerve, 25:763–764, 2002.

[30] R. M. Enoka and A. J. Fuglevand. Motor unit physiology: some unresolved issues. Muscle & Nerve, 24:4–17, 2001.

[31] D. Farina, R. Merletti, and R. M. Enoka. The extraction of neural strategies from the surface emg. J. Appl. Physiol., 96:1486–1495, 2004.

[32] R. A. Faville, A. J. Pullan, K. M. Sanders, and N. P. Smith. A biophysically based mathematical model of unitary potential activity in interstitial cell of cajal. Biophys J, 95:88–104, 2008.

[33] J. W. Fernandez, M. L. Buist, D. P. Nickerson, and P. J. Hunter. Modelling the passive and nerve activated response of the rectus femoris muscle to a flexion loading: A finite element framework. Medical Engineering and Physics, 27:862–870, 2005.

[34] J. W. Fernandez, P. Mithraratne, S. F. Thrupp, M. H. Tawhai, and P. J. Hunter. Anatomically based geometric modelling of the musculo-skeletal system and other organs. Biomechan. Model. Mechanobiol., 2:139–155, 2004.

[35] A. J. Fuglevand and S. S. Segal. Simulation of motor unit recruitment and microvascular unit perfusion: spatial considerations. Journal of Applied Physiology, 83(4):1223–1234, 1997.

[36] A. J. Fuglevand, D. A. Winter, and A. E. Patla. Models of recruitment and rate coding organization in motor unit pools. Journal of neurophysiology, 70(6):2470–2488.

[37] J. P. Gabriel, L. M. Struder, D. G. Rüegg, and M. A. Schnetzer. A mathematical model for the steady activation of a skeletal muscle. SIAM journal on applied mathematics, 68(3), 2007.

[38] C. W. Gear. The simultaneous numerical solution of differential-algebraic equations. IEEE Trans. Circuit Theory, 18(1):89–95, 1971.

[39] S. J. Goldberg, K. E. Wilson, and M. S. Shall. Summation of extraocular motor unit tensions in the lateral recuts muscle of the cat. Muscle & Nerve, 20:1229–1235, 1997.

[40] D. Graupe, editor. The status of noninvasive functional electrical stimulation and ambulation performance for thoracic-level complete paraplegics, Department of Electrical and Computer Engineering and Department of Bioengineering University of Illinois, Chicargo, May 2005. BEM and NFSI Conference Proceedings.

[41] H. Gray. Gray's Anatomy. Churchill Livingstone, 38th edition, 1995.

[42] L. Grimby and J. Hannerz. Firing rate and recruitment order of toe extensor motor units in different modes of voluntary contraction. J. Physiol., 264:865–879, 1977.

[43] M. D. Grounds, L. Sorokin, and J. White. Strength at the extracellular matrix-muscle interface. Scand. J. Med. Sci. Sports, pages 1–11, 2005.

[44] A. C. Guyton and J. E. Hall. Textbook of medical physiology. W.B. Saunders Company, Philadelphia, Pennsylvania, tenth edition, 2001.

[45] T. Hamada, T. Hayashi, T. Kimura, K. Nakao, and T. Moritani. Electrical stimulation of human lower extremities enhances energy consumption, carbohydrate oxidation, and whole body glucose uptake. J Appl Physiol, 96:911–916, 2004.

[46] P. J. Harrison and A. Taylor. Individual excitatory post-synaptic potentials due to muscle spindle ia afferents in cat triceps surae motoneurons. J. Physiol., 312:455–470, 1981.

[47] C. J. Heckman. Computer simulations of the effects of different synaptic input systems on the steady-state input-output structure of the motoneuron pool. Journal of Neurophysiology, 71(5):1727–1739, 1994.

[48] C. J. Heckman and M. D. Binder. Analysis of effective synaptic currents generated by homonymous ia afferent fibers in motoneurons of the cat. J. Neurophysiol., 1988.

[49] C. J. Heckman and M. D. Binder. Computer simulation of the steady-state input-output function of the cat medial gastrocnemius motoneuron pool. J. Neurophysiol., 1991.

[50] C. J. Heckman and M. D. Binder. Computer simulations of motoneuron firing rate modulation. Journal of Neurophysiology, 96(4):1005–1008, 1993.

[51] E. Henneman and C. Olson. Relations between structure and function in the design of skeletal muscles. Journal of Neurophysiology, 28:581–598, 1965.

[52] E. Henneman, G. Somjen, and D. Carpenter. Excitability and inhibitibility of motoneurons of different sizes. Journal of Neurophysiology, 28:599–620, 1965.

[53] E. Henneman, G. Somjen, and D. Carpenter. Functional significance of cell size in spinal motoneurons. Journal of Neurophysiology, 28:560–580, 1965.

[54] K. B. Henriksson-Larsén, J. Lexell, and Sjöström.

[55] C.S. Henriquez. Simulation the electrical behavior of cardiac tissue using the bidomain model. Critical reviews in biomedical engineering, 21(1):1–77, 1993.

[56] A. V. Hill. The heat of shortening and the dynamic constraints of muscle. Royal Society of London Proceedings Series B, 126:136–195, 1938.

[57] A. C. Hindmarsh. Odepack, a systematized collection of ode solvers. IMACS Transactions on scientific computation, pages 55–64, August 1982.

[58] A.L. Hodgkin and A.F. Huxley. A quantitative description of membrane current and is application to conduction and excitation in nerve. Journal of Physiology, 117:500–544, 1952.

[59] C. J. Houtman, D. F. Stegeman, J. P Van Dijk, and M. J. Zwarts. Changes in muscle fiber conduction velocity indicate recruitment of distinct motor unit populations. J. Appl. Physiol., 95:1045–1054, 2003.

[60] A. F. Huxley. Muscle structure and theories of contraction. Prog. Biophys. Biophys. Chem., 7:255–318, 1957.

[61] R. H. Jensen and D. T. Davy. An investigation of muscle lines of action about the hip: A centroid line approach vs. the straight line approach. J. Biomech, 8:103–110, 1975.

[62] G. Kamen and D. C. C. Du. Independence of motor unit recruitment and rate modulation during precision force control. Neuroscience, 88(2):643–653, 1999.

[63] J. H. K. Kim, J. B. Davidson, O. Röhrle, T. K. Soboleva, and A. J. Pullan. Anatomically based lower limb nerve model for electrical stimulation. Biomedical Engineering Online, 6(1):48, 2007.

[64] M. D. Klein-Breteler, C. W. Spoor, and F. C. T. Van Der Helm. Measuring muscle and joint geometry parameters of a shoulder for modeling purposes. J. Biomech, 32:1191–1197, 1999.

[65] R. Kobetic, R. J. Triolo, J. P. Uhlir, C. Bieri, M. Wibowo, G. Polando, E. B. Marsolais, J. A. Davis Jr., K. A. Ferguson, and M. Sharma. Implanted functional electrical stimulation system for mobility in paraplegia: a follow-up case report. IEEE Trans. Rehab. Eng., 7(4):390–398, 1999.

[66] J. H. Koolstra and T. M. G. J. Van Eijden. A method to predict muscle control in the kinematically and mechanically indeterminate human masticatory system. J. Biomech., 34:1179–1188, 2001.

[67] D. A. Lansdown, A. Ding, M. Wadington, J. L. Hornberger, and B. M. Damon. Quantitative diffusion tensor mri-based fiber tracking of human skeletal muscle. J Appl Physiol, 103:673–681, April 2007.

[68] R. R. Lemos, J. Rocke, G. V. G. Baranoski, Y. Kawakami, and T. Kurihara. Modeling and simulating the deformation of human skeletal muscle based on anatomy and physiology. Comput. Animation Virtual Worlds, 16:319–330, 2005.

[69] Z. Lertmanorat, K. J. Gustafson, and D. M. Durand. Electrode array for reversing the recruitment order of peripheral nerve stimulation: experimental studies. Annals of Biomedical Engineering, 34(1):152–160, 2006.

[70] J. Lexell, D. Downham, and M. Sjöström. Distribution of different fibre types in human skeletal muscles. Journal of the Neurological Sciences, 72:211–222, 1986.

[71] R. L. Lieber and J. Friden. Functional and clinical significance of skeletal muscle architecture. Muscle & Nerve, 23:1647–1666, 2000.

[72] W. T. Lieberson, H. J. Holmquest, D. Scott, and H. Dow. Functional electrotherapy stimulation of the swing phase of the gait in hemiplegic patients. Arch. Phys. Med. and Rehab., 42:101–106, 1961.

[73] L. M. Livshitz, P. D. Einziger, and J. Mizrahi. Current distribution in skeletal muscle activated by functional electrical stimulation: image-series formulation and isometric recruitment curve. Annals of Biomedical Engineering, 28:1218–1228, 2000.

[74] T. P. Martin, R. B. Stein, and D. C. Hoeppner, P. H. Reid. Influence of electrical stimulation on the morphological and metabolic properties of paralyzed muscle. J. Appl. Physiol., 72(4):1401–1406, 1992.

[75] C. C. McIntyre, A. G. Richardson, and W. M. Grill. Modeling the excitability of mammalian nerve fibers: influence of afterpotentials on the recovery cycle. J Neurophyiol, 87(2):995–1006, 2002.

[76] C. J. McNeil, T. J. Doherty, D. W. Stashuk, and C. L. Rice. Motor unit number estimates in the tibialis anterior muscle of young, old, and very old men. Muscle & Nerve, 31:461–467, 2005.

[77] P. A. McNulty and A. G. Cresswell. Recruitment of single human low-threshold motor units with increasing load at different muscle lengths. Journal of Electromyography and Kinesiology, 14:369–377, 2004.

[78] A. E. J. Miller, J. D. MacDougall, M. A. Tarnopolsky, and D. G. Sale. Gender differences in strength and muscle fiber characteristics. European Journal of Applied Physiology, 66:254–262, 1993.

[79] H. S. Milner-Brown, R. B. Stein, and R. Yemm. Changes in firing rate of human motor units during linearly changing voluntary contractions. J. Physiol. Lond., 230:371–390, 1973.

[80] R. J. Monti, R. R. Roy, and V. R. Edgerton. Role of motor unit structure in defining function. Muscle & Nerve, 24:848–866, 2001.

[81] R.J. Monti, R.R. Roy, J.A. Hodgson, and V.R. Edgerton. Transmission of forces within mammalian skeletal muscles. Journal of Biomechanics, 32:371–380, 1999.

[82] C. I. Morse, J. M. Thom, N. D. Reeves, K. M. Birch, and M. V. Narici. In vivo physiological cross-sectional area and specific force are reduced in the gastrocnemius of elderly men. J. Appl. Physiol., 99:1050–1055, 2005.

[83] D. Noble, A. Varqhese, P. Kohl, and P. Noble. Improved guinea-pig ventricular cell model incorporating a diadic space, ikr and iks, and length and tension dependent processes. Can J Cardiol, 14(1):123–134, jan 1998.

[84] R. M. Nussbaumer, D. G. Rüegg, L. M. Struder, and J. P. Gabriel. Computer simulation of the motoneuron pool-muscle complex. i. input system and motoneuron pool. Biol. Cybern., 86:317–333, 2002.

[85] C.W.J. Oomens, M. Maenhout, C.H. van Oijen, M.R. Drost, and F.P. Baaijens. Finite element modelling of contracting skeletal muscle. The Royal Society, 358:1453–1460, 2003.

[86] M. G. Pandy. Computer modeling and simulation of human movement. Ann. Rev. Biomed. Engrg., 3:245–273, 2001.

[87] B. Pasquet, A. Carpentier, and J. Duchateau. Change in muscle fascicle length influences the recruitment and discharge rate of motor units during isometric contractions. J. Neurophysiol, 94:3126–3133, 2005.

[88] A.C. Paul. Muscle length affects the architecture and pattern of innervation differently in leg muscles of mouse, guinea pig, and rabbit compared to those of human and monkey muscles. The Anatomical Record, 262:301–309, 2001.

[89] J.B. Peter, R.J. Barnard, V.R. Edgerton, C.A. Gillespie, and K.E. Stempel. Metabolic profiles of three fiber types of skeletal muscle in guinea pigs and rabbits. Biochemistry, 11:2627–2633, 1972.

[90] C. Pette and S. Staron. Cellular and molecular diversities of mammalian skeletal muscle fibers. Reviews of Physiology, Biochemistry and Pharmacology, 116:1–76, 1009.

[91] D. Pette and G. Vrbová. Adaptation of mammalian skeletal muscle fibers to chronic electrical stimulation. Rev. Physiol. Biochem. Pharmacol., 120:115–202, 1992.

[92] L. R. Petzold. Automatic selection of methods for solving stiff and nonstiff systems of ordinary differential equations. SIAM J. Sci. Stat. Comput., 4:136–148, 1983.

[93] D.B. Popović and T. Sinkjær. Control of Movement for the Physically Disabled. Academic Mind, 11000 Belgrade, Yugoslavia, Center for Sensory-Motor Interaction Aalbourg University, 2nd edition edition, 2003.

[94] M.B. Popović, D.B. Popović, T. Sinkjær, A. Stefanovic, and L. Schwirtlich. Clinical evaluation of functional electrical therapy in acute hemiplegic subjects. Journal of Rehabilitation Research and Development, 40(5):443–454, September/October 2003.

[95] U. Proske and D. L. Morgan. Stiffness of cat soleus muscle and tendon during activation of part of muscle. J. Neurophysiol., 52:459–468, 1984.

[96] A. J. Pullan, M. L. Buist, and L. K. Cheng. Mathematically modelling the electrical activity of the heart. World Scientific Publishing Co. Pte. Ltd., 5 Toh Tuck Link, Singapore 596224, 2005.

[97] Z. A. Riley, A. H. Maerz, J. C. Litsey, and R. M. Enoka. Motor unit recruitment in human biceps brachii during sustained voluntary contractions. J. Physiol., 586(8):2183–2193, 2008.

[98] E. Rios, M Karanek, J. Ma, and A. Gonzalez. An allosteric model of the molecular interactions of excitation-contraction coupling in skeletal muscle. Journal of General Physiology, 102:449–481, 1993.

[99] O. Röhrle, J. B. Davidson, and A. J. Pullan. Bridging scales: A three-dimensional electromechanical finite element model of skeletal muscle. Siam Journal of Scientific Computing, 30(6):2882–2904, 2008.

[100] O. Röhrle and A. J. Pullan. Three-dimensional finite element modelling of muscle forces during mastication. J. Biomech., 40:3363–3372, 2007.

[101] R.R. Roy, A. Garfinkel, M. Ounjian, J. Payne, A. Hirahara, E. Hsu, and V.R. Edgerton. Three-dimensional structure of cat tibialis anterior motor units. Muscle & nerve, 18:1187–1195, 1995.

[102] S. Rush, J. A. Abildskov, and R. McFee. Resistivity of body tissues at low frequencies. Circulation Research, 12:40–50, 1963.

[103] O. H. Schmitt. Biological information processing using the concept of interpenetrating domains. In K. N. Leibovic, editor, Information Processing in the Nervous System. Springer-Verlag, New York, 1969.

[104] H. P. Schwann and C. F. Kay. The conductivity of living tissues. Ann N Y Acad Sci, 65(6):1007–10013, Aug 1957.

[105] P. R. Shorten, P. O'Callaghan, J. B. Davidson, and T. K. Soboleva. A mathematical model of fatigue in skeletal muscle force contraction. Journal of Muscle Research and Cell Motility, 28(6):293–313, August 2007.

[106] M. Sjöström, J. Lexell, A. Eriksson, and C. C. Taylor. Evidence of fibre hyperplasia in human skeletal muscles from healthy young men? Eur. J. Appl. Physiol., 62:301–304, 1991.

[107] E. V. Solodovnik, G. J. Cokkinides, and A. P. Sakis Melipoulos. Comparison of implicit and explicit integration techniques on the non-ideal transformer example. In Systems Theory, 1998, Prodeeding of the Thirtieth Southeastern Symposium on, pages 32–37, 1998.

[108] V. M. Spitzer and D. G. Whitlock. National Library of Medicine: atlas of the visible human male - reverse engineering of the human body. Sudbury, Massachusetts: Jones and Bartlett Publishers, 1998.

[109] M.D. Stern, G. Pizarro, and E. Rios. Local control model of excitation-contraction coupling in skeletal muscle. Journal of General Physiology, 110:415–440, 1997.

[110] S.F. Street. Lateral transmission of tension in frog myofibers: a myofibrillar network and transverse cytoskeletal connections are possible transmitters. Journal of Cell Physiology, 114:346–364, 1983.

[111] G.J. Tortora and S.R. Grabowski. Principles of Anatomy and Physiology. John Wiley & Sons, Inc., 9th edition, 2000.

[112] W. Wallinga, S.L. Meijer, M.J. Alberink, M. Vliek, E.D. Wienk, and D.L. Ypey. Modelling action potentials and membrane currents of mammalian skeletal muscle fibre in coherence with potassium concentration changes in the t-tubular system. European Biophysics Journal, 28:317–329, 1999.

[113] W. A. Weijs and B. Hillen. Cross-sectional areas and estimated intrinsic strength of the human jaw muscles. Acta Morphol. Neerl. Scand., 23:267–274, 1985.

[114] J. M. Winters and L. Stark. Muscle models: what is gained and what is lost by varying model complexity. Biological Cybernetics, 55:403–420, 1987.

[115] J. M. Winters and L-Y. Woo, S, editors. Multiple muscle systems biomechanics and movement organization. Springer-Verlag, 1990.

[116] R. Wuerker, A.M. McPhedran, and E. Henneman. Properties of motor units in a heterogeneous pale muscle (m. gastrocnemius) of the cat. Journal of Neurophysiology, 28:85–99, 1965.

[117] W. Yao, A. J. Fuglevand, and R. M. Enoka. Motor-unit synchronization increases emg amplitude and decreases force steadiness of simulated contractions. J. Neurophysiol., 83:441–452, 2000.

[118] C.A. Yucesoy, B.H.F.J.M. Koopman, P.A. Huijing, and H.J. Grootenboer. Three-dimensional finite element modeling of skeletal muscle using a two-domain approach: linked fiber-matrix mesh model. Journal of Biomechanics, 35:1253–1262, 2002.

Appendix A

The Shorten *et.al.* 2007 Cellular Model

The following equations are obtained from the CellML representation of the Shorten *et.al.* 2007 Skeletal Muscle model [105]. The CellML code can be found on the CellML website [1]. For a full description of all parameters please refer to [105].

The Sarcolemmal and T-tubular Membrane

$$I_T = \frac{1000}{1} * \frac{(vS - vT)}{R_a} \quad \mu A/cm^2 \tag{A.1}$$

$$\frac{\partial(vS)}{\partial(time)} = -\frac{(I_s^{ionic} + I_T)}{C_m} \quad mV/ms \tag{A.2}$$

$$\frac{\partial(vT)}{\partial(time)} = -\frac{\left(I_t^{ionic} - \frac{I_T}{\gamma}\right)}{C_m} \quad mV/ms \tag{A.3}$$

$$I_s^{ionic} = \left(I^{Cl} + I^{IR} + I^{DR} + I^{Na} + I^{NaK} - I^{HH}\right) \quad \mu A/cm^2 \tag{A.4}$$

$$I_t^{ionic} = \left(I_t^{Cl} + I_t^{IR} + I_t^{DR} + I_t^{Na} + I_t^{NaK}\right) \quad \mu A/cm^2 \tag{A.5}$$

$$\begin{aligned}\frac{\partial(K_i)}{\partial(time)} = -f_T * \frac{\left(I_t^{IR} + I_t^{DR} + I_{rest}^{K} - 2 * I_t^{NaK}\right)}{\frac{1000}{1} * FF * tsi} \\ -\frac{\left(I^{IR} + I^{DR} + I_{rest}^{K} - 2 * I^{NaK}\right)}{\frac{1000}{1} * FF * tsi2} \quad mM/ms\end{aligned} \tag{A.6}$$

[1] www.cellml.org

Table A.1: Parameters Associated with the Sarcolemmal and T-tubular Membranes.

Parameter	Unit	Value (fast/slow)
C_m	$\mu F/cm^2$	1/0.05
γ	$-$	4.8/2.79
R_a	Ωcm^2	150
F	C/mol	96485
τ_K, τ_{Na}	ms	350/559
f_T	$-$	0.0032/0.00174
τ_{K_2}, τ_{Na_2}	ms	$350 * \frac{0.2}{f_T}$
I^K_{rest}	$\mu A/cm^2$	1.02/0.34
I^{Na}_{rest}	$\mu A/cm^2$	$-1.29/-0.43$
τ	$-$	0.23/0.14
$\bar{\alpha}_h$	ms^{-1}	0.0081
$\bar{\alpha}_m$	$ms^{-1}mV^{-1}$	0.288
$\bar{\alpha}_n$	$ms^{-1}mV^{-1}$	0.0131
β_h	ms^{-1}	4.38
β_m	ms^{-1}	1.38
β_n	ms^{-1}	0.067
V_m	mV	-46
V_n	mV	-40
V_h	mV	-45
V_a	mV	70
V^∞_S	mV	$-78/-68$
$V^\infty_{h^K_S}$	mV	-40
A_a	mV	150
A^∞_S	mV	5.8/7.1
$A^\infty_{h^K_S}$	mV	7.5
K_{α_h}	mV	14.7
K_{β_h}	mV	9
K_{α_m}	mV	10
K_{β_m}	mV	18
K_{α_n}	mV	7
K_{β_n}	mV	40
R	$mJ/K/mol$	8314.41
T	K	293
$\bar{g}_{Cl}$	mS/cm^2	19.65/3.275
$\bar{g}_K$	mS/cm^2	64.8/10.8
$\bar{g}_{Na}$	mS/cm^2	804/134
K_K	mM^2	950
K_S	mM^2	1
K_{mK}	mM	1
K_{mNa}	mM	13
J_{NaK}	$\mu mol/cm^2/s$	0.000621/0.0001656
V_τ	mV	90/70

$$\frac{\partial(K_t)}{\partial(time)} = \frac{\left(I_t^{IR} + I_t^{DR} + I_{rest}^{K} - 2 * I_t^{NaK}\right)}{\frac{1000}{1} * FF * tsi} - \frac{(K_t - K_e)}{\tau_K} \quad mM/ms \tag{A.7}$$

$$\frac{\partial(K_e)}{\partial(time)} = \frac{\left(I^{IR} + I^{DR} + I_{rest}^{K} - 2 * I^{NaK}\right)}{\frac{1000}{1} * FF * tsi3} + \frac{(K_t - K_e)}{\tau_{K2}} \quad mM/ms \tag{A.8}$$

$$\frac{\partial(Na_i)}{\partial(time)} = -f_T * \frac{\left(I_t^{Na} + I_r^{Na}est + 3 * I_t^{NaK}\right)}{\frac{1000}{1} * FF * tsi} - \frac{\left(I^{Na} + I_{rest}^{Na} + 3 * I^{NaK}\right)}{\frac{1000}{1} * FF * tsi2} \quad mM/ms \tag{A.9}$$

$$\frac{\partial(Na_t)}{\partial(time)} = \frac{\left(I_t^{Na} + I_{rest}^{Na} + 3 * I_t^{NaK}\right)}{\frac{1000}{1} * FF * tsi} - \frac{(Na_t - Na_e)}{\tau_{Na}} \quad mM/ms \tag{A.10}$$

$$\frac{\partial(Na_e)}{\partial(time)} = \frac{\left(I^{Na} + I_{rest}^{Na} + 3 * I^{NaK}\right)}{\frac{1000}{1} * FF * tsi3} + \frac{(Na_t - Na_e)}{\tau_{Na2}} \quad mM/ms \tag{A.11}$$

$$E^K = \frac{RR * TT}{FF} * \ln \frac{K_e}{K_i} \quad mV \tag{A.12}$$

$$E_t^K = \frac{RR * TT}{FF} * \ln \frac{K_t}{K_i} \quad mV \tag{A.13}$$

$$Cl_i = \frac{156.5}{\left(5 + e^{\frac{-FF * E_K}{RR * TT}}\right)} \quad mM \tag{A.14}$$

$$Cl_o = (156.5 - 5 * Cl_i) \quad mM \tag{A.15}$$

$$Cl_{i_t} = \frac{156.5}{\left(5 + e^{\frac{-FF * E_{K_t}}{RR * TT}}\right)} \quad mM \tag{A.16}$$

$$Cl_{o_t} = (156.5 - 5 * Cl_{i_t}) \quad mM \tag{A.17}$$

$$J_K = vS * \frac{\left(K_i - K_e * e^{\frac{-1 * FF * vS}{RR * TT}}\right)}{\left(1 - e^{\frac{-1 * FF * vS}{RR * TT}}\right)} \quad mVmM \tag{A.18}$$

$$J_{K_t} = vT * \frac{\left(K_i - K_t * e^{\frac{-1*FF*vT}{RR*TT}}\right)}{\left(1 - e^{\frac{-1*FF*vT}{RR*TT}}\right)} \quad mVmM \tag{A.19}$$

Sarcoplasmic Chloride Channel

$$a = \frac{1}{\left(1 + e^{\frac{(vS - V_a)}{A_a}}\right)} \tag{A.20}$$

$$J_{Cl} = vS * \frac{\left(Cl_i - Cl_o * e^{\frac{FF*vS}{RR*TT}}\right)}{\left(1 - e^{\frac{FF*vS}{RR*TT}}\right)} \quad mVmM \tag{A.21}$$

$$g_{Cl} = \bar{g}_C l * (a)^4 \quad mS/cm^2 \tag{A.22}$$

$$I^{Cl} = g_{Cl} * \frac{J_{Cl}}{45} \quad \mu A/cm^2 \tag{A.23}$$

Sarcoplasmic Inward Rectifier Potassium Channel

$$K_R = K_e * e^{-del*E_K*\frac{FF}{RR*TT}} \quad mM \tag{A.24}$$

$$\bar{g}_I R = G_K * \frac{(K_R)^2}{\left(K_K + (K_R)^2\right)} \quad mS/cm^2 \tag{A.25}$$

$$y = 1 - \left(1 + \frac{K_S * \left(1 + \frac{(K_R)^2}{K_K}\right)}{(S_i)^2 * e^{\frac{2*(1-del)*vS*FF}{RR*TT}}}\right)^{-1} \tag{A.26}$$

$$g_{IR} = \bar{g}_I R * y \quad mS/cm^2 \tag{A.27}$$

$$I^{IR} = g_{IR} * \begin{cases} 1; & \text{if } J_K > 0, \\ 0 & \text{otherwise.} \end{cases} * \frac{J_K}{50} \quad \mu A/cm^2 \tag{A.28}$$

Sarcoplasmic Delayed Rectifier Potassium Channel

$$\alpha_n = \bar{\alpha}_n * \frac{(vS - V_n)}{\left(1 - e^{-\frac{(vS - V_n)}{K_{\alpha_n}}}\right)} \quad ms^{-1} \tag{A.29}$$

$$\beta_n = \bar{\beta}_n * e^{-\frac{(vS - V_n)}{K_{\beta_n}}} \quad ms^{-1} \tag{A.30}$$

$$h_{K_\infty} = \frac{1}{\left(1 + e^{\frac{\left(vS - V_{hK_\infty}\right)}{A_{hK_\infty}}}\right)} \tag{A.31}$$

$$\tau_h K = 1000 * e^{-\frac{(vS+40)}{25.75}} \quad ms \tag{A.32}$$

$$\frac{\partial(n)}{\partial(time)} = (\alpha_n * (1 - n) - \beta_n * n) \tag{A.33}$$

$$\frac{\partial(hK)}{\partial(time)} = \frac{(hK_\infty - hK)}{\tau_{hK}} \tag{A.34}$$

$$g_{DR} = \bar{g}_K * (n)^4 * hK \quad mS/cm^2 \tag{A.35}$$

$$I^{DR} = g_{DR} * \frac{J_K}{50} \quad \mu A/cm^2 \tag{A.36}$$

Sarcoplasmic Sodium Channel

$$\alpha_h = \bar{\alpha}_h * e^{-\frac{(vS - V_h)}{K\alpha_h}} \quad ms^{-1} \tag{A.37}$$

$$\beta_h = \frac{\bar{\beta}_h}{\left(1 + e^{-\frac{(vS - V_h)}{K_{\beta_h}}}\right)} \quad ms^{-1} \tag{A.38}$$

$$\alpha_m = \bar{\alpha}_m * \frac{(vS - V_m)}{\left(1 - e^{-\frac{(vS - V_m)}{K\alpha_m}}\right)} \quad ms^{-1} \tag{A.39}$$

$$\beta_m = \bar{\beta}_m * e^{-\frac{(vS - V_m)}{K_{\beta_m}}} \quad ms^{-1} \tag{A.40}$$

$$S_\infty = \frac{1}{\left(1 + e^{\frac{\left(vS - V_{S_\infty}\right)}{A_{S_\infty}}}\right)} \tag{A.41}$$

$$\tau_S = \frac{8571}{\left(0.2 + 5.65 * \left(\frac{(vS + V_\tau)}{100}\right)^2\right)} \quad ms \tag{A.42}$$

$$J_{Na} = vS * \frac{\left(Na_i - Na_e * e^{\frac{-1 * FF * vS}{RR * TT}}\right)}{\left(1 - e^{\frac{-1 * FF * vS}{RR * TT}}\right)} \quad mVmM \tag{A.43}$$

$$\frac{\partial(m)}{\partial(time)} = (\alpha_m * (1 - m) - \beta_m * m) \tag{A.44}$$

$$\frac{\partial(h)}{\partial(time)} = (\alpha_h * (1-h) - \beta_h * h) \tag{A.45}$$

$$\frac{\partial(S)}{\partial(time)} = \frac{(S_\infty - S)}{\tau_S} \tag{A.46}$$

$$g_{Na} = \bar{g}_{Na} * (m)^3 * h * S \quad mS/cm^2 \tag{A.47}$$

$$I^{Na} = g_{Na} * \frac{J_{Na}}{75} \quad \mu A/cm^2 \tag{A.48}$$

Sarcoplasmic Sodium Potassium Exchanger

$$\sigma = \frac{1}{7} * \left(e^{\frac{Na_e}{67.3}} - 1\right) \tag{A.49}$$

$$f1 = \left(1 + 0.12 * e^{-0.1*vS*\frac{FF}{RR*TT}} + 0.04 * \sigma * e^{-vS*\frac{FF}{RR*TT}}\right)^{-1} \tag{A.50}$$

$$\bar{I}_{NaK} = FF * \frac{\bar{J}_{NaK}}{\left(1 + \frac{K_{m_K}}{K_e}\right)^2 * \left(1 + \frac{K_{m_{Na}}}{Na_i}\right)^3} \quad \mu A/cm^2 \tag{A.51}$$

$$I^{NaK} = \bar{I}_{NaK} * f1 \quad \mu A/cm^2 \tag{A.52}$$

T-tubular Chloride Channel

$$a_t = \frac{1}{\left(1 + e^{\frac{(vT - V_a)}{A_a}}\right)} \tag{A.53}$$

$$J_{Cl_t} = vT * \frac{\left(Cl_{i_t} - Cl_{o_t} * e^{\frac{FF*vT}{RR*TT}}\right)}{\left(1 - e^{\frac{FF*vT}{RR*TT}}\right)} \quad mVmM \tag{A.54}$$

$$g_{Cl_t} = \bar{g}_{Cl} * (a_t)^4 \quad mS/cm^2 \tag{A.55}$$

$$I_t^{Cl} = eta_{Cl} * g_{Cl_t} * \frac{J_{Cl_t}}{45} \quad \mu A/cm^2 \tag{A.56}$$

T-tubular Inward Rectifier Potassium Channel

$$K_{R_t} = K_t * e^{-del*E_{K_t}*\frac{FF}{RR*TT}} \quad mM \tag{A.57}$$

$$\bar{g}_{IR_t} = G_K * \frac{(K_{R_t})^2}{\left(K_K + (K_{R_t})^2\right)} \quad mS/cm^2 \tag{A.58}$$

$$y_t = 1 - \left(1 + \frac{K_S * \left(1 + \frac{\left(K_{R_t}\right)^2}{K_K} \right)}{\left(S_i\right)^2 * e^{\frac{2*(1-del)*vT*FF}{RR*TT}}} \right)^{-1} \tag{A.59}$$

$$g_{IR_t} = \bar{g}_{IR_t} * y_t \quad mS/cm^2 \tag{A.60}$$

$$I_t^{IR} = eta_{IR} * g_{IR_t} * \frac{J_{K_t}}{50} \quad \mu A/cm^2 \tag{A.61}$$

T-tubular Delayed Rectifier Potassium Channel

$$\alpha_{n_t} = \bar{\alpha}_n * \frac{(vT - V_n)}{\left(1 - e^{-\frac{(vT-V_n)}{K_{\alpha_n}}}\right)} \quad ms^{-1} \tag{A.62}$$

$$\beta_{n_t} = \bar{\beta}_n * e^{-\frac{(vT-V_n)}{K_{\beta_n}}} \quad ms^{-1} \tag{A.63}$$

$$hK_{\infty_t} = \frac{1}{\left(1 + e^{\frac{\left(vT - V_{hK_\infty}\right)}{A_{hK_\infty}}}\right)} \tag{A.64}$$

$$\tau_{hK_t} = 1 * e^{-\frac{(vT+40)}{25.75}} \quad ms \tag{A.65}$$

$$\frac{\partial(n_t)}{\partial(time)} = (\alpha_{n_t} * (1 - n_t) - \beta_{n_t} * n_t) \tag{A.66}$$

$$\frac{\partial(hK_t)}{\partial(time)} = \frac{(hK_{\infty_t} - hK_t)}{\tau_{hK_t}} \tag{A.67}$$

$$g_{DR_t} = \bar{g}_K * (n_t)^4 * hK_t \quad mS/cm^2 \tag{A.68}$$

$$I_{DR_t} = eta_{DR} * g_{DR_t} * \frac{J_{K_t}}{50} \quad \mu A/cm^2 \tag{A.69}$$

T-tubular Sodium Channel

$$\alpha_{h_t} = \bar{\alpha}_h * e^{-\frac{(vT-V_h)}{K_{\alpha_h}}} \quad ms^{-1} \tag{A.70}$$

$$\beta_{h_t} = \frac{\bar{\beta}_h}{\left(1 + e^{-\frac{(vT-V_h)}{K_{\beta_h}}}\right)} \quad ms^{-1} \tag{A.71}$$

$$\alpha_{m_t} = \bar{\alpha}_m * \frac{(vT - V_m)}{\left(1 - e^{-\frac{(vT-V_m)}{K_{\alpha_m}}}\right)} \quad ms^{-1} \tag{A.72}$$

$$\beta_{m_t} = \bar{\beta}_m * e^{-\frac{(vT - V_m)}{K_{\beta_m}}} \quad ms^{-1} \tag{A.73}$$

$$S_{\infty_t} = \frac{1}{\left(1 + e^{\frac{\left(vT - V_{S_\infty}\right)}{A_{S_\infty}}}\right)} \tag{A.74}$$

$$\tau_{S_t} = \frac{8571}{\left(0.2 + 5.65 * \left(\frac{(vT + V_\tau)}{100}\right)^2\right)} \quad ms \tag{A.75}$$

$$J_{Na_t} = vT * \frac{\left(Na_i - Na_t * e^{\frac{-1 * FF * vT}{RR * TT}}\right)}{\left(1 - e^{\frac{-1 * FF * vT}{RR * TT}}\right)} \quad mVmM \tag{A.76}$$

$$\frac{\partial(m_t)}{\partial(time)} = (\alpha_{m_t} * (1 - m_t) - \beta_{m_t} * m_t) \tag{A.77}$$

$$\frac{\partial(h_t)}{\partial(time)} = (\alpha_{h_t} * (1 - h_t) - \beta_{h_t} * h_t) \tag{A.78}$$

$$\frac{\partial(S_t)}{\partial(time)} = \frac{(S_{\infty_t} - S_t)}{\tau_{S_t}} \tag{A.79}$$

$$g_{Na_t} = \bar{g}_{Na} * (m_t)^3 * h_t * S_t \quad mS/cm^2 \tag{A.80}$$

$$I_t^{Na} = eta_{Na} * g_{Na_t} * \frac{J_{Na_t}}{75} \quad \mu A/cm^2 \tag{A.81}$$

T-tubular Sodium Potassium Exchanger

$$\sigma_t = \frac{1}{7} * \left(e^{\frac{Na_t}{67.3}} - 1\right) \tag{A.82}$$

$$f1_t = \left(1 + 0.12 * e^{-0.1 * vT * \frac{FF}{RR * TT}} + 0.04 * \sigma_t * e^{-vT * \frac{FF}{RR * TT}}\right)^{-1} \tag{A.83}$$

$$\bar{I}_{NaK_t} = FF * \frac{\bar{J}_{NaK}}{\left(1 + \frac{K_{m_K}}{K_t}\right)^2 * \left(1 + \frac{K_{m_{Na}}}{Na_i}\right)^3} \quad \mu A/cm^2 \tag{A.84}$$

$$I_{NaK_t} = eta_{NaK} * \bar{I}_{NaK_t} * f1_t \quad \mu A/cm^2 \tag{A.85}$$

Table A.2: Model Parameters of the Sarcoplasmic Reticulum Calcium Release Model

Parameter	Unit	Value (fast/slow)
k_L	ms^{-1}	0.002
k_{Lm}	ms^{-1}	1000
f	$-$	0.2
α_1	ms^{-1}	0.2
K	mV	4.5
$\bar{V}$	mV	-20
i_2	$\mu m^3 ms^{-1}$	300/60

The Release of Calcium from the Sarcoplasmic Reticulum

$$k_C = 0.5 * \alpha_1 * e^{\frac{(vT-\bar{V})}{8*K}} \tag{A.86}$$

$$k_{Cm} = 0.5 * \alpha_1 * e^{\frac{(\bar{V}-vT)}{8*K}} \tag{A.87}$$

$$\frac{\partial(C_0)}{\partial(time)} = -k_L * C_0 + k_{Lm} * O_0 - 4 * k_C * C_0 + k_{Cm} * C_1 \tag{A.88}$$

$$\frac{\partial(O_0)}{\partial(time)} = k_L * C_0 - k_{Lm} * O_0 + \frac{-4 * K_C * O_0}{f} + f * k_{Cm} * O_1 \tag{A.89}$$

$$\frac{\partial(C_1)}{\partial(time)} = 4 * k_C * C_0 - k_{Cm} * C_1 + \frac{-k_L * C_1}{f} + f * k_{Lm} * O_1 - 3 * k_C * C_1 + 2 * k_{Cm} * C_2 \tag{A.90}$$

$$\frac{\partial(O_1)}{\partial(time)} = \frac{k_L * C_1}{f} - k_{Lm} * f * O_1 + \frac{4 * k_C * O_0}{f} - f * k_{Cm} * O_1 + \frac{-3 * k_C * O_1}{f} + 2 * f * k_{Cm} * O_2 \tag{A.91}$$

$$\frac{\partial(C_2)}{\partial(time)} = 3 * k_C * C_1 - 2 * k_{Cm} * C_2 + \frac{-k_L * C_2}{(f)^2} + (f)^2 * k_{Lm} * O_2 - 2 * k_C * C_2 + 3 * k_{Cm} * C_3 \tag{A.92}$$

$$\frac{\partial(O_2)}{\partial(time)} = \frac{3 * k_C * O_1}{f} - 2 * f * k_{Cm} * O_2 + \frac{k_L * C_2}{(f)^2} \\ -k_{Lm} * (f)^2 * O_2 + \frac{-2 * k_C * O_2}{f} + 3 * f * k_{Cm} * O_3 \tag{A.93}$$

$$\frac{\partial(C_3)}{\partial(time)} = 2 * k_C * C_2 - 3 * k_{Cm} * C_3 + \frac{-k_L * C_3}{(f)^3} \\ +k_{Lm} * (f)^3 * O_3 - k_C * C_3 + 4 * k_{Cm} * C_4 \tag{A.94}$$

$$\frac{\partial(O_3)}{\partial(time)} = \frac{k_L * C_3}{(f)^3} - k_L m * (f)^3 * O_3 + \frac{2 * k_C * O_2}{f} \\ -3 * k_{Cm} * f * O_3 + \frac{-k_C * O_3}{f} + 4 * f * k_{Cm} * O_4 \tag{A.95}$$

$$\frac{\partial(C_4)}{\partial(time)} = k_C * C_3 - 4 * k_{Cm} * C_4 + \frac{-k_L * C_4}{(f)^4} \\ +k_{Lm} * (f)^4 * O_4 \tag{A.96}$$

$$\frac{\partial(O_4)}{\partial(time)} = \frac{k_C * O_3}{f} - 4 * f * k_{Cm} * O_4 + \frac{k_L * C_4}{(f)^4} \\ -k_{Lm} * (f)^4 * O_4 \tag{A.97}$$

Intracellular Species

This section defines the concentrations of a number of intracellular species concerned with the contraction of the cell. The units are those of the dependant variable.

$$V_o = 0.95 * L_x * \pi * (R_R)^2 \pi \quad \mu m^3 \tag{A.98}$$

$$V_1 = 0.01 * V_o \quad \mu m^3 \tag{A.99}$$

$$V_2 = 0.99 * V_o \quad \mu m^3 \tag{A.100}$$

$$V_{SR1} = 0.01 * V_{SR} \quad \mu m^3 \tag{A.101}$$

$$V_{SR2} = 0.99 * V_{SR} \quad \mu m^3 \tag{A.102}$$

$$T_0 = T_{tot} - Ca_{T_2} - Ca_{CaT2} - D_0 - D_1 - D_2 - A_1 - A_2 \quad \mu M \tag{A.103}$$

Table A.3: Model Parameters of Skeletal Muscle Contraction

Parameter	Unit	Value (fast/slow)
ν_{SR}	$\mu M ms^{-1} \mu m^{-3}$	4.875/2.4375
K_{SR}	μM	1
L_e	$\mu m^3 ms^{-1}$	0.00002/0.00004
τ_R, τ_R^{SR}	$\mu m^3 ms^{-1}$	0.75
L_x	μm	1.1
R_R	μm	0.5
V_{SR}	μm^3	$0.05 * (L_x \pi R_R^2)$
k_T^{on}	$\mu M^{-1} ms^{-1}$	0.04425/0.0885
k_T^{off}	ms^{-1}	0.115
T_{tot}	μM	140
k_P^{on}	$\mu M^{-1} ms^{-1}$	0.0417/0
k_P^{off}	ms^{-1}	0.0005/0
P_{tot}	μM	1500
k_{Mg}^{on}	$\mu M^{-1} ms^{-1}$	0.000033/0
k_{Mg}^{off}	ms^{-1}	0.003/0
k_{Cs}^{on}	$\mu M^{-1} ms^{-1}$	0.000004
k_{Cs}^{off}	ms^{-1}	0.005
Cs_{tot}	μM	31000
k_{CATP}^{on}	$\mu M^{-1} ms^{-1}$	0.15
k_{CATP}^{off}	ms^{-1}	30
k_{MATP}^{on}	$\mu M^{-1} ms^{-1}$	0.0015
k_{MATP}^{off}	ms^{-1}	0.15
τ_{ATP}	$\mu m^3 ms^{-1}$	0.375
τ_{Mg}	$\mu m^3 ms^{-1}$	1.5
k_0^{on}	ms^{-1}	0
k_0^{off}	ms^{-1}	0.15
k_{Ca}^{on}	ms^{-1}	0.15
k_{Ca}^{off}	ms^{-1}	0.05
f_o	ms^{-1}	1.5/0.5
f_p	ms^{-1}	15/5
h_o	ms^{-1}	0.24/0.08
h_p	ms^{-1}	0.18/0.06
g_o	ms^{-1}	0.12/0.04
b_p	ms^{-1}	0.00002867/0.00000394
k_p	$\mu m^3 ms^{-1}$	$3.62 * 10^{-6}$
A_p	$mM^2 ms^{-1}$	1
B_p	$mM ms^{-1}$	0.0001
PP	mM^2	6

$$\frac{\partial(Ca_1)}{\partial(time)} = i2 * (O_0 + O_1 + O_2 + O_3 + O_4) * \frac{(Ca_{SR1} - Ca_1)}{V_1}$$
$$- nu_{SR} * \frac{\frac{Ca_1}{(Ca_1+K_{SR})}}{V_1} + L_e * \frac{(Ca_{SR1} - Ca_1)}{V_1} - \tau_R * \frac{(Ca_1 - Ca_2)}{V_1} \quad \text{(A.104)}$$
$$- \left(k_{P_{on}} * Ca_1 * (P_{tot} - Ca_{P1} - Mg_{P1}) - k_{P_{off}} * Ca_{P1}\right)$$
$$- \left(k_{CATP_{on}} * Ca_1 * ATP1 - k_{CATP_{off}} * Ca_{ATP1}\right) \quad \mu M$$

$$\frac{\partial(Ca_{SR1})}{\partial(time)} = -i2 * (O_0 + O_1 + O_2 + O_3 + O_4) * \frac{(Ca_{SR1} - Ca_1)}{V_{SR1}}$$
$$+ nu_{SR} * \frac{\frac{Ca_1}{(Ca_1+K_{SR})}}{V_{SR1}} - L_e * \frac{(Ca_{SR1} - Ca_1)}{V_{SR1}} - \tau_{SR_R} * \frac{(Ca_{SR1} - Ca_{SR2})}{V_{SR1}}$$
$$- \left(k_{Cs_{on}} * Ca_{SR1} * (Cs_{tot} - Ca_{Cs1}) + -k_{Cs_{off}} * Ca_{Cs1}\right) \quad \mu M$$
(A.105)

$$\frac{\partial(Ca_2)}{\partial(time)} = -nu_{SR} * \frac{\frac{Ca_2}{(Ca_2+K_{SR})}}{V_2} + L_e * \frac{(Ca_{SR2} - Ca_2)}{V_2} + \tau_R * \frac{(Ca_1 - Ca_2)}{V_2}$$
$$- \left(k_{T_{on}} * Ca_2 * T_0 - k_{T_{off}} * Ca_{T_2} + k_{T_{on}} * Ca_2 * Ca_{T_2} - k_{T_{off}} * Ca_{CaT2}\right)$$
$$- \left(k_{T_{on}} * Ca_2 * D_0 - k_{T_{off}} * D_1 + k_{T_{on}} * Ca_2 * D_1 - k_{T_{off}} * D_2\right)$$
$$- \left(k_{P_{on}} * Ca_2 * (P_{tot} - Ca_{P2} - Mg_{P2}) - k_{P_{off}} * Ca_{P2}\right)$$
$$- \left(k_{CATP_{on}} * Ca_2 * ATP2 - k_{CATP_{off}} * Ca_{ATP2}\right) \quad \mu M$$
(A.106)

$$\frac{\partial(Ca_{SR2})}{\partial(time)} = nu_{SR} * \frac{\frac{Ca_2}{(Ca_2+K_{SR})}}{V_{SR2}} - L_e * \frac{(Ca_{SR2} - Ca_2)}{V_{SR2}}$$
$$+ \tau_{SR_R} * \frac{(Ca_{SR1} - Ca_{SR2})}{V_{SR2}} - \left(k_{Cs_{on}} * Ca_{SR2} * (Cs_{tot} - Ca_{Cs2}) - k_{Cs_{off}} * Ca_{Cs2}\right)$$
$$- \frac{1000}{1} * \left(A_p * \left(P_{SR} * \frac{0.001}{1} * Ca_{SR2} - PP \right) * \begin{cases} 1; & \text{if } \left(P_{SR} * \frac{0.001}{1} * Ca_{SR2} - PP\right) > 0, \\ 0 & \text{otherwise.} \end{cases} \right)$$
$$* P_{SR} * Ca_{SR2} - \frac{1000}{1} B_p * P_{C_SR} * \left(PP - P_{SR} * \frac{0.001}{1} * Ca_{SR2} \right)$$
$$* \begin{cases} 1; & \text{if } \left(PP - P_{SR} * \frac{0.001}{1} * Ca_{SR2}\right) > 0, \\ 0 & \text{otherwise.} \end{cases} \quad \mu M$$
(A.107)

$$\frac{\partial(Ca_{T_2})}{\partial(time)} = k_{T_{on}} * Ca_2 * T_0 - k_{T_{off}} * Ca_{T_2} - k_{T_{on}} * Ca_2 * Ca_{T_2} + k_{T_{off}} * Ca_{CaT2} - k_{0_{on}} * Ca_{T_2} + k_{0_{off}} * D_1 \quad \mu M \tag{A.108}$$

$$\frac{\partial(Ca_{P1})}{\partial(time)} = k_{P_{on}} * Ca_1 * (P_{tot} - Ca_{P1} - Mg_{P1}) - k_{P_{off}} * Ca_{P1} \quad \mu M \tag{A.109}$$

$$\frac{\partial(Ca_{P2})}{\partial(time)} = k_{P_{on}} * Ca_2 * (P_{tot} - Ca_{P2} - Mg_{P2}) - k_{P_{off}} * Ca_{P2} \quad \mu M \tag{A.110}$$

$$\frac{\partial(Mg_{P1})}{\partial(time)} = k_{Mg_{on}} * (P_{tot} - Ca_{P1} - Mg_{P1}) * Mg1 - k_{Mg_{off}} * Mg_{P1} \quad \mu M \tag{A.111}$$

$$\frac{\partial(Mg_{P2})}{\partial(time)} = k_{Mg_{on}} * (P_{tot} - Ca_{P2} - Mg_{P2}) * Mg2 - k_{Mg_{off}} * Mg_{P2} \quad \mu M \tag{A.112}$$

$$\frac{\partial(Ca_{Cs1})}{\partial(time)} = k_{Cs_{on}} * Ca_{SR1} * (Cs_{tot} - Ca_{Cs1}) - k_{Cs_{off}} * Ca_{Cs1} \quad \mu M \tag{A.113}$$

$$\frac{\partial(Ca_{Cs2})}{\partial(time)} = k_{Cs_{on}} * Ca_{SR2} * (Cs_{tot} - Ca_{Cs2}) - k_{Cs_{off}} * Ca_{Cs2} \quad \mu M \tag{A.114}$$

$$\frac{\partial(Ca_{ATP1})}{\partial(time)} = k_{CATP_{on}} * Ca_1 * ATP1 - k_{CATP_{off}} * Ca_{ATP1} - \tau_{ATP} * \frac{(Ca_{ATP1} - Ca_{ATP2})}{V_1} \quad \mu M \tag{A.115}$$

$$\frac{\partial(Ca_{ATP2})}{\partial(time)} = k_{CATP_{on}} * Ca_2 * ATP2 - k_{CATP_{off}} * Ca_{ATP2} + \tau_{ATP} * \frac{(Ca_{ATP1} - Ca_{ATP2})}{V_2} \quad \mu M \tag{A.116}$$

$$\frac{\partial(Mg_{ATP1})}{\partial(time)} = k_{MATP_{on}} * Mg1 * ATP1 - k_{MATP_{off}} * Mg_{ATP1} - \tau_{ATP} * \frac{(Mg_{ATP1} - Mg_{ATP2})}{V_1} \quad \mu M \tag{A.117}$$

$$\frac{\partial(Mg_{ATP2})}{\partial(time)} = k_{MATP_{on}} * Mg2 * ATP2 - k_{MATP_{off}} * Mg_{ATP2} + \tau_{ATP} * \frac{(Mg_{ATP1} - Mg_{ATP2})}{V_2} \quad \mu M \tag{A.118}$$

$$\frac{\partial(ATP1)}{\partial(time)} = -\left(k_{CATP_{on}} * Ca_1 * ATP1 - k_{CATP_{off}} * Ca_{ATP1}\right) - \left(k_{MATP_{on}} * Mg1 * ATP1 - k_{MATP_{off}} * Mg_{ATP1}\right) - \tau_{ATP} * \frac{(ATP1 - ATP2)}{V_1} \quad \mu M \tag{A.119}$$

$$\frac{\partial(ATP2)}{\partial(time)} = -\left(k_{CATP_{on}} * Ca_2 * ATP2 - k_{CATP_{off}} * Ca_{ATP2}\right) - \left(k_{MATP_{on}} * Mg2 * ATP2 - k_{MATP_{off}} * Mg_{ATP2}\right) + \tau_{ATP} * \frac{(ATP1 - ATP2)}{V_2} \quad \mu M \tag{A.120}$$

$$\frac{\partial(Mg1)}{\partial(time)} = -\left(k_{Mg_{on}} * (P_{tot} - Ca_{P1} - Mg_{P1}) * Mg1 - k_{Mg_{off}} * Mg_{P1}\right) - \left(k_{MATP_{on}} * Mg1 * ATP1 - k_{MATP_{off}} * Mg_{ATP1}\right) - \tau_{Mg} * \frac{(Mg1 - Mg2)}{V_1} \quad \mu M \tag{A.121}$$

$$\frac{\partial(Mg2)}{\partial(time)} = -\left(k_{Mg_{on}} * (P_{tot} - Ca_{P2} - Mg_{P2}) * Mg2 - k_{Mg_{off}} * Mg_{P2}\right) - \left(k_{MATP_{on}} * Mg2 * ATP2 - k_{MATP_{off}} * Mg_{ATP2}\right) + \tau_{Mg} * \frac{(Mg1 - Mg2)}{V_2} \quad \mu M \tag{A.122}$$

$$\frac{\partial(Ca_{CaT2})}{\partial(time)} = k_{T_{on}} * Ca_2 * Ca_{T_2} - k_{T_{off}} * Ca_{CaT2} - k_{Ca_{on}} * Ca_{CaT2} + k_{Ca_{off}} * D_2 \quad \mu M \tag{A.123}$$

$$\frac{\partial(D_0)}{\partial(time)} = -k_{T_{on}} * Ca_2 * D_0 + k_{T_{off}} * D_1 + k_{0_{on}} * T_0 - k_{0_{off}} * D_0 \quad \mu M \tag{A.124}$$

$$\frac{\partial(D_1)}{\partial(time)} = k_{T_{on}} * Ca_2 * D_0 - k_{T_{off}} * D_1 + k_{0_{on}} * Ca_{T_2} - k_{0_{off}} * D_1 - k_{T_{on}} * Ca_2 * D_1 + k_{T_{off}} * D_2 \quad \mu M \tag{A.125}$$

$$\frac{\partial(D_2)}{\partial(time)} = k_{T_{on}} * Ca_2 * D_1 - k_{T_{off}} * D_2 + k_{Ca_{on}} * Ca_{CaT2} - k_{Ca_{off}} * D_2 - f_o * D_2 + f_p * A_1 + g_o * A_2 \quad \mu M \tag{A.126}$$

$$\frac{\partial(A_1)}{\partial(time)} = f_o * D_2 - f_p * A_1 + h_p * A_2 - h_o * A_1 \quad \mu M \tag{A.127}$$

$$\frac{\partial(A_2)}{\partial(time)} = -h_p * A_2 + h_o * A_1 - g_o * A_2 \quad \mu M \tag{A.128}$$

$$\frac{\partial(P)}{\partial(time)} = \frac{0.001}{1} * (h_o * A_1 - h_p * A_2) - 1 * b_p * P - 1 * k_p * \frac{(P - P_{SR})}{V_2} \quad \mu M \tag{A.129}$$

$$\begin{aligned}\frac{\partial(P_{SR})}{\partial(time)} = {} & k_p * \frac{(P - P_{SR})}{V_{SR2}} - A_p * \left(P_S R * \frac{0.001}{1} * Ca_{SR2} - PP\right) * \\ & \begin{cases} 1; & \text{if } \left(P_{SR} * \frac{0.001}{1} * Ca_{SR2} - PP\right) > 0, \\ 0 & \text{otherwise.} \end{cases} * \frac{0.001}{1} * P_{SR} * Ca_{SR2} \\ & + B_p * P_{C_{SR}} * \left(PP - P_{SR} * \frac{0.001}{1} * Ca_{SR2}\right) * \\ & \begin{cases} 1; & \text{if } \left(PP - P_{SR} * \frac{0.001}{1} * Ca_{SR2}\right) > 0, \\ 0 & \text{otherwise.} \end{cases} \quad \mu M\end{aligned} \tag{A.130}$$

$$\begin{aligned}\frac{\partial(P_{C_{SR}})}{\partial(time)} = {} & A_p * \left(P_{SR} * \frac{0.001}{1} * Ca_{SR2} - PP\right) * \\ & \begin{cases} 1; & \text{if } \left(P_{SR} * \frac{0.001}{1} * Ca_{SR2} - PP\right) > 0, \\ 0 & \text{otherwise.} \end{cases} * \frac{0.001}{1} * P_{SR} * Ca_{SR2} \\ & - B_p * P_{C_{SR}} * \left(PP - P_{SR} * \frac{0.001}{1} * Ca_{SR2}\right) * \\ & \begin{cases} 1; & \text{if } \left(PP - P_{SR} * \frac{0.001}{1} * Ca_{SR2}\right) > 0, \\ 0 & \text{otherwise.} \end{cases} \quad \mu M\end{aligned} \tag{A.131}$$